COIL-DOMINATED LARGE BORE SUPERCONDUCTING QUADRUPOLES FOR HIGH RIGIDITY ISOTOPE BEAMS

By

David Buell Greene

A DISSERTATION

Submitted to
Michigan State University
in partial fulfillment of the requirements
for the degree of

Physics—Doctor of Philosophy

2024

ABSTRACT

Future nuclear physic research requires the transport of high rigidity heavy ion beams. The Facility for Rare Isotope Beams (FRIB) requires such beams with high momentum acceptance for future nuclear physics research. This will require larger aperture magnets that can still provide efficient and accurate steering and focusing. This dissertation will discuss the electro-magnetic (EM) design, beam impact, and mechanical design along with prototyping and testing of a 18 T/m gradient and 0.2 meter diameter aperture coil-dominated quadrupole, which will serve as a future upgrade for FRIB's fragment separator.

ACKNOWLEDGMENTS

I would like to thank Ting Xu for advising me through my PhD study and the knowledge, support, and honesty with which he guided me through my study, may the helium gods always smile on you. I would like to thank Peter Ostroumov for the opportunities, resources, and knowledge which made my PhD study possible.

In addition, I would like to thank the members of my thesis committee Professors: Remco Zegers, Yue Hao, Kirsten Tollefson, and Sergey Baryshev for the guidance they have given me in both research and career development.

A very large thanks is deserved for every member of the SC magnet group and the SC mechanical design team: Yoonhyuck Choi, Xiaoji Du, Danlu Zhang, Junseong Kim, Hengkang Zheng, Hai Nguyen, John Wenstrom, Yamen al-Mahmoud, Ryan Koschay, and Courtney Smith. Who have all helped me to reach where I am today and made my research goals possible.

A very special thanks to every group member, technician, and machinist working under the SRF & SC Magnet group umbrella, whom I have all sufficiently annoyed with request for help on builds and searching for tools. Thanks to: Chris Compton, Ken Witgen, Tanner Brenton, Erik Mikko-Eicher, Elaine Pfeiffelman, Tyler Weber, Joe Asciutto, and Chris Magsig. Without any of which I would not have had the testing quality I needed, or known what cabinets Kapton tape and hot glue were in.

Last but not least, I'd like to thank all my family and friends who have all supported me through every trial and tribulation in my life. My mother, father, sister, Victor, Cassie, grandmother, and to my grandfather who will never see this. I'd like to thank the friends who helped me survive my graduate experience, to name a few: Hannah, Kelly, Lexi, Cristhian, Julia, Josh, Bob, Karina, Jordan O.F., Jordan P., Ian, Carissa, Cami, Senora, Nick, Giovanni. My friends who have supported me from afar during my time in Michigan: Scout, Connor, Vince, Sarah, Thomas, David, Alvaro, Ben, Hunter, Russell. My thanks are truly beyond the capability of my expression in writing, but none the less, thank you.

TABLE OF CONTENTS

LIST OF TABLES

LIST OF FIGURES

CHAPTER 1

INTRODUCTION

1.1 General Principles of Particle Accelerators

Particle accelerators are a fundamental tool for nuclear and particle physics research. The most fundamental elements of a particle accelerator are components that allow for the acceleration of charged ions, and components which allow for the control of the motion of these charge ions. The components which makes those things possible are accelerating cavities and optical magnets respectively. This chapter will discuss the principles of particle accelerators with an emphasis on optical magnets as they are the primary topic of discussion of this dissertation.

1.1.1 Basic Components of Beam Transportation

The most basics principles for beam transportation are ion acceleration, beam steering, and beam focusing/defocusing. The primary mechanism for acceleration of charged particles/ions in most modern accelerator systems is Radio-Frequency (RF) cavities. The concept of RF cavities for acceleration is that a radio frequency AC signal can be applied to a conducting cavity. Conceptually similar to a wave guide, this generates an oscillating electric field which can be used for acceleration of charged ions by synchronizing the ion motion from the source with the oscillation of the electric field, such that net acceleration is achieved. In the case of a linear accelerator (linac), multiple cavities can be used in series to achieve the desired amount of acceleration. In the case of circular accelerators, such as cyclotrons and synchrotrons, desired acceleration is achieved by having the ions pass through the same cavities or accelerating gaps multiples times by cycling them through a circular path. Lastly, the ideal geometry of cavities, and material selection for cavities are very robust topics, which cannot be covered in great detail within the scope of this dissertation.

Magnets are used for the control of particle motion separate from acceleration. Besides begin accelerated to a target kinetic energy, ions need to be transported to their target destination. In order to control the transport of charged ion beams to their target, this requires the control of motion not only in the accelerating direction, but also in the transverse plane of motion. When discussing beam particle coordinates, we will always refer to x and y as being the transverse plane of motion.

Controlling the motion in the x, y plane is important, as it is necessary to be able to steer, focus, and defocus the beam, in order to accurately delivery beam to its intended location. In summation, this means that magnets are used to steer the beam, and to focus or defocus the beam. Beam steering is achieved through the use of vertical and horizontal dipoles, while beam focusing and defocusing is achieved through magnetic quadrupoles. Higher order multipole magnets are also used for a variety of applications in accelerator systems, but this will be discussed further and in detail in later sections.

1.1.2 Formalism's of Beam Dynamics

The motion in a particle accelerator is dictated by the interaction of charged particles with an electromagnetic field. Fundamentally, the force dictating the movement of these particles is the Lorenz force, $\vec{F_L}$, seen in Eq. 1.1. Where q is the charge of the particle, $\vec{E}$ is the electric field, $\vec{B}$ is the magnetic field, and $\vec{v}$ is the velocity of the particle. It can be seen from this why electrical fields are used to accelerate particles in the transport direction and magnetic fields affect only the transverse motion of the particles.

$$\vec{F_L} = q(\vec{E} + \vec{v} \times \vec{B}) \tag{1.1}$$

From this, the equations of motion can be found by solving for the Hamiltonian of the system, knowing that $\frac{d\vec{p}}{dt} = F_L$. Applying this to the Euler-Lagrange equation yields the Hamiltonian of Eq. 1.2, and the equations of motion can then be expressed in terms of the conjugate pair of the position and canonical momentum seen in Eq. 1.3.

$$H = c[m^2c^2 + (\vec{P} - e\vec{A})^2]^{1/2} + e\Phi \tag{1.2}$$

$$\frac{\partial x}{\partial t} = \frac{\partial H}{\partial P_x}, \quad \frac{\partial P_x}{\partial t} = -\frac{\partial H}{\partial x} \tag{1.3}$$

Where m is the mass, c is the speed of light, $\vec{P}$ is the momentum, e is the charge of an electron, $\vec{A}$ is the magnetic vector potential, and Φ is the electric scalar potential. For the transverse motion

through a static magnetic field where $\vec{E} = 0$. We can express the magnetic field in terms of it's transverse components in Eq. 1.4, when solving for the component of $B_x$and B_y, they can be expressed in terms of a Power series to arrive at Eq. 1.5, which is known as Beth representation [1].

$$\vec{B} = B_x(x, y)\hat{x} + B_y(x, y)\hat{y} \tag{1.4}$$

$$B_y + jB_x = B_0 \sum_{n=1}^{\infty} (b_n + ja_n)(x + jy)^{n-1} \tag{1.5}$$

$$b_n = \frac{1}{B_0(n-1)!} \frac{\partial^{n-1} B_y}{\partial x^{n-1}}\bigg|_{x=y=0}, \quad a_n = \frac{1}{B_0(n-1)!} \frac{\partial^{n-1} B_x}{\partial x^{n-1}}\bigg|_{x=y=0} \tag{1.6}$$

where j is the imaginary number, B_0 is the dipole strength corresponding to the constant first term of the expansion, b_n and a_n are multipole coefficients, x and y are the transverses positions, and n is the multipole index, where $n = 1$ is the dipole, $n = 2$ is the quadrupole, and so forth.

When expressing and using the multipole coefficient in Eq. 1.6, b_n is referred to as the normal multipole coefficients and a_n is referred to as the skew multipole coefficient. For magnetic multipoles, the normal orientation refers to the rotational orientation of the multipoles, such that the skew terms are zero. From normal position, a skew multipole can then be expressed as a $\pi/2n$ rotation from the normal position for any "nth" order multipole.

For particle motion through dipoles and quadrupoles, the equations of motion can then be expressed as Hill's equations [1].

$$x'' + K_x(s)x = 0, \quad y'' + K_y(s)y = 0 \tag{1.7}$$

$$K_x = \frac{1}{\rho^2} + K_1(s), \quad K_y = -K_1(s) \tag{1.8}$$

$$K_1(s) = \pm \frac{\partial B_y}{\partial x} \tag{1.9}$$

Where s is the beam transport direction expressed in a Frenet-Serret (curvilinear) coordinate system. This is useful as many accelerators are circular in nature. K_x and K_y are expressed in Eq. 1.9, where $1/\rho = B_0/B\rho$ and B_0 is the dipole component and $B\rho$ is the magnetic beam rigidity [1].

From Hill's equation, it can then be seen that the motion through a dipole or quadrupole is directly dependent on the dipole field constant, and the quadrupole field gradient. This is very important as to why the multipole gradients are given as design requirements for magnet design and fabrication.

1.2 Magnets for Accelerator Systems

Magnets serve multiple functions in particle accelerators for controlling the motion and delivering beam, and it takes a variety of magnet types to do this. Dipoles are used for beam steering in both the x and y direction in order to move the entire centroid of the beam along bends. Quadrupoles are used to both focus and defocus the beam in different directions. Depending on the quadrupole polarity, it can either focus or defocus beam. In particular a quadrupole, which focuses in the x will defocus in the y and vice versa. As the focusing force from the quadrupole is proportional to the distance from center of the particle a combination of focusing and defocusing elements can be made to achieve a net focus of the beam in x and y, this is normally refereed to as a **FODO** lattice. Where **F** is a focusing element in one direction, **O** is drift space, and D is a defocusing element in the same direction as **F**. Typically **FODO** lattices are made by combining three quadrupoles together in one mechanical assembly, separated by some fixed space in the beam transport direction. This magnet assembly is typically refereed to as a magnetic triplet.

Sextupole magnets are used as correctors of chromatic aberrations. As an ion beam realistically has some distribution of energy, and the entire beam is not at the target energy, this impacts the beam focusing. Sextupoles help to correct these affect and allow the low and high energy parts of the beam the same as the target energy particles. Octupoles similarly help to correct away higher order chromatic aberrations and other high order nonlinearities. Beyond DC optical magnets, accelerators can also implement AC magnets for a variety of purposes, for example magnetic undulators use an alternating magnetic field to "wiggle" the beam at a specific frequency to produce a desired frequency of X-rays. As optical magnets are the primary discussion of this thesis, the two broad forms of magnet design types will be discussed in the following subsections, iron-dominated and coil-dominated.

1.2.1 Iron-Dominated Magnets

Iron-dominated magnets are magnets in which an electrical coil is wrapped around an iron core, commonly called an iron pole, in order to provide a desired amount of magnetic flux through that iron core. For an iron-dominated magnet, the response of this iron core is what generates a majority of the desired field strength, additionally the geometry of this core also contributes the major portion of the field shape, thus the strength and shape of the field is "dominated" by the iron.

The ideal pole-tip geometry differs by magnet type. The ideal geometry for a dipole, quadrupole, sextupole and so on are different. The ideal geometry for a steering dipole iron-pole is a plane of iron, while the ideal pole-tip geometry for a quadrupole is a hyperbola for example. Field shape and quality can also be affected by the surface treatment of the poles. Additionally, for quadrupoles and dipoles, the field close to the pole tip will exhibit nonlinear behavior and the field strength will shift from linear to geometric series like [2], [3] as you approach the pole tip. The distance at which nonlinearities are seen is dependent on the iron saturation and the design. The saturation of the iron also has an impact on nonlinearities being introduced into the field, which negatively impacts beam optics. The iron saturation becomes a limiting factor in the field strength achievable for iron dominated designs [4]. The formulation of geometry, design of electrical coils, and fabrication process for iron-dominated magnets is a robust, but well studied topic with much history in the field.

1.2.2 Coil-Dominated Magnets

Coil-dominated magnets refer to magnets where the magnetic field strength and shape are dominated by the coil geometry, and iron may be used for symmetric magnetic shielding on the outside of the coils. As coil geometry dominates the field shape, it is important to have methods and techniques for optimizing coil geometry. The optimizing of the coil shape can be started from the field solution of line currents in the z-direction. It is commonly known in the study of multipole magnets for accelerator systems that a current density of $j_z = j_0 \cos(n\phi)$ generates pure "nth" order multipole harmonics in 2D. Therefore, creating practical coil/winding designs which can closely approximate a cosine distribution of current around the bore tube is not only important, but also

the backbone of coil-dominated magnet design.

The 2D analytical solution for current distributions which generate pure magnetic multipoles is a cosine distribution in the form of Eq. 1.10 [1], [5].

$$J(\phi) = J_0 \cos n\phi \tag{1.10}$$

Where J is current density, ϕ is azimuth angle, and n is multipole order. In the 2D, this can be demonstrated by generating a circle and defining a continuous current distribution of this form to generate pure multipoles. As an example, this can be seen in Fig. 1.1.

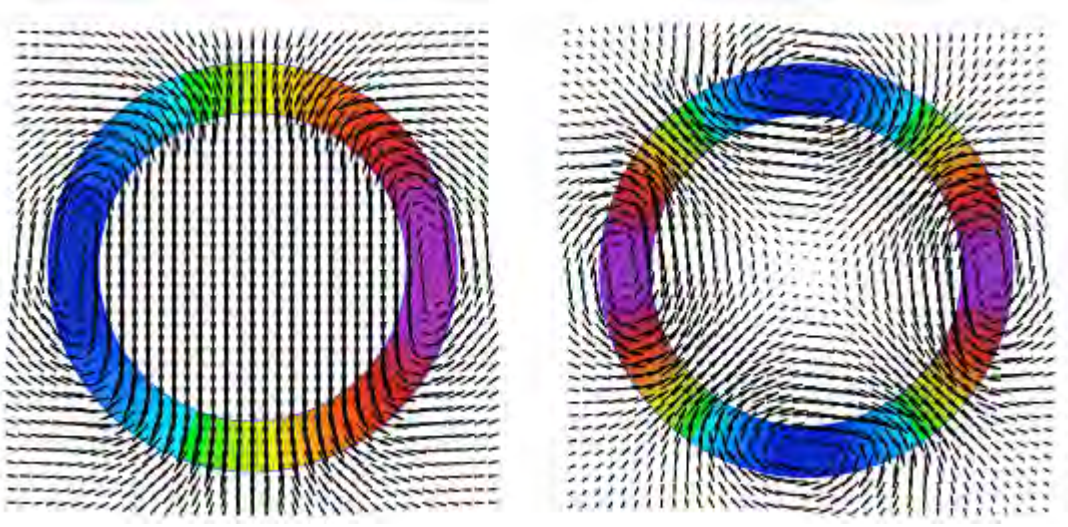

Figure 1.1 Picture of example multipoles generated using $\cos\phi$ (left) and $\cos 2\phi$ (right) current density distributions to create a dipole (left) and quadrupole (right) magnetic field [5].

To create uniform multipoles where non-principal multipole content does not contribute to the total field significantly, designs aim to create winding packs which closely satisfy a cosine distribution. The impact of higher order terms and what is considered "significant" impact is very application dependent and is typically part of a uniformity requirement for a given design. As creating a continuous cylindrical sheet where an exact cosine distribution of current density can be applied is impossible, a variety of design techniques exist to create windings which can create cosine current distributions in realistic situations of using real cable geometry, where windings are operating at the same current magnitude and are connect in series. A typical style of coil winding

used to generate cosine current distributions are called sector coils. A 2D example of sector coils can be seen in Fig. 1.2.

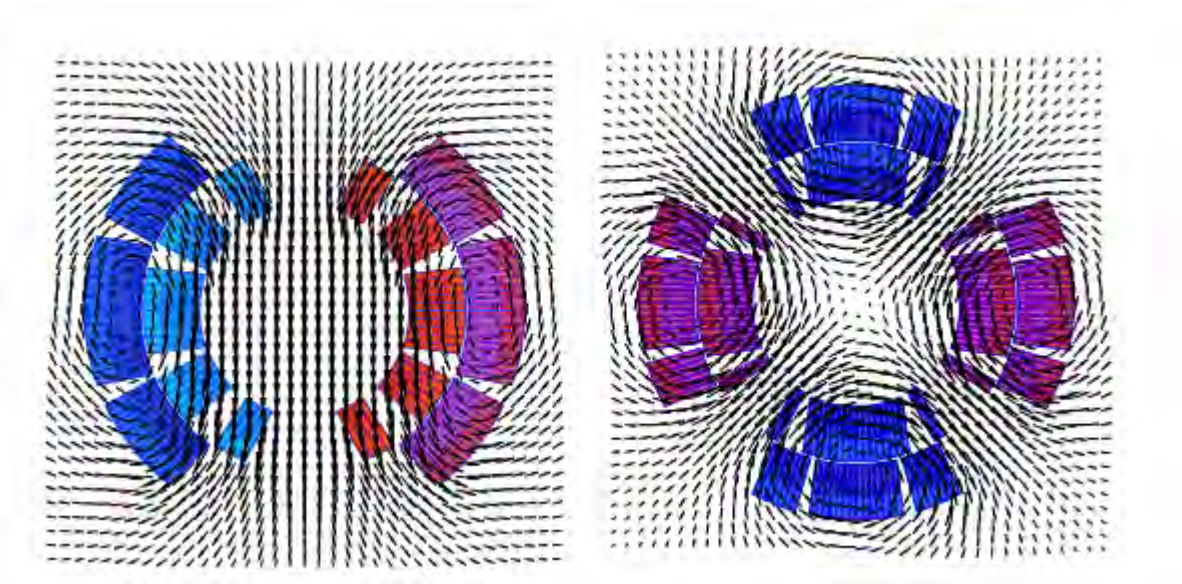

Figure 1.2 Picture of example multipoles generated using $\cos\phi$ (left) and $\cos 2\phi$ (right) current density distributions to create a dipole (left) and quadrupole (right) magnetic field [5].

There are multiple approaches to approximating a cosine current distribution using coil geometry. There are segment coils [6], canted cosine theta coils (CCT) [7], and discrete cosine theta coils (DCT) also referred to as Walstrom style coils [8], where theta still refers to the cylindrical azimuth angle. The bulk of this text will focus on the formulation, design, fabrication, and testing of a DCT/Walstrom style quadrupole, designed to be employed as a focusing magnet in FRIB's fragment separator section.

1.3 FRIB's CDQ Project

FRIB requires the transport of secondary rare isotope beams with high emittance and high magnetic rigidity. The magnetic rigidity of the beam can reach as high as 8 Tm. Sections of FRIB require apertures on the scale of 0.2 m and large iron yokes for the quadrupole magnets are required in order to have sufficient strength, uniformity, and efficiency [9]–[11]. A number of issues are introduced when using large iron yokes at this scale. These include cool down times that span weeks and difficulties with alignment of the magnet due to transportation or thermal cycles. The primary issue with using iron yokes in this application, is their undesirable interaction with

magnetic sextupole correctors. An iron yoke with four pole tips, interacts with a sextupole inside of the yoke due to the difference in their symmetry. This interaction generates a non-zero dipole component, causing unwanted deflection of the beam. One of the primary quadrupole triplets used in FRIB's fragment separator is the A1900's triplet [12]. The quadrupoles used in this triplet are FRIB's Fragment Separator Quadrupole Type C (FSQC) and Type B (FSQB), both of which have higher order multipole packages. A proposal has been made to replace the A1900 triplet with a new design, utilizing superconducting coil-dominated quadrupoles to eliminate this dipole effect and for additional benefits the design will provide. Introducing a coil-dominated design will allow for shorter cooldown times due to smaller cold-mass, theoretically less coil training, absence of nonlinearities introduced by iron saturation, lower inductance allowing faster beam tuning time, and the design yields comparable field uniformity as the existing FSQ magnet designs. The quadrupoles are designed to serve the same optical function as FRIB's B-C-B triplets which consist of a triplet made form FSQB and FSQC magnets. We call our design Coil-Dominated Quadrupole (CDQ), and this thesis will consist of the design of the C type CDQ, along with the fabrication of a sub-scaled prototype, and the prototype cold test and magnetic field mapping results.

CHAPTER 2

MAGNET EM DESIGN & ANALYSIS

2.1 Discrete Cosine Theta Geometry

In this chapter we will outline the process for the designed geometry of the CDQ coil and summarize the magnetostatic analysis of the design model, the conductor selection, and the quench analysis of the designed coil.

2.1.1 Geometry Formulation

The aim of this formulation for coil-dominated winding geometry is to create a winding that has a $\cos n\phi$ distribution at every point in z within the boundary of the coil geometry. Coil geometry created in this way is often called Discrete Cosine Theta (DCT). The reason being the cosine distribution of the current can be divided into discrete current paths, where the number of discretized turns is determined by the designer, similar to that of a CCT coil, but lacking the canted angle. To summarize how the generating function for the primary geometry of a DCT / Walstrom coil is arrived at, one can start from a generalized 3 dimensional continuous current density distribution. The current density distribution can be expressed as the curl of a magnetic dipole density distribution, seen in Eq. 2.1.

$$\boldsymbol{J}(r, \phi, z) = \nabla \times \boldsymbol{M}(r, \phi, z) \tag{2.1}$$

Where $\boldsymbol{J}$ is the current density distribution in cylindrical coordinates, and $\boldsymbol{M}$ is the magnetic dipole density distribution. It is important to state that $\boldsymbol{M}$ is a fictitious quantity used only as a mathematical tool. By defining $\boldsymbol{J}$ in this way, it assures that $\boldsymbol{J}$ corresponds to magnetic field solutions with zero divergence, which must be true for physical solutions for magnetic field. It follows that $\boldsymbol{M}$ can be expressed in a form which assures that J_z, the z component of $\boldsymbol{J}$, has a cosine distribution.

$$\boldsymbol{M} = F(r, z) \sin n\phi \hat{\mathrm{r}} \tag{2.2}$$

Where $F_n(r, z)$ is a generalized function relating to the dipole distribution. By taking the curl of Eq. 2.2, it follows that the cylindrical components of $\boldsymbol{J}$ take the form of Eqs. 2.3, 2.4, and 2.5.

$$J_z = -n\frac{F(r,z)}{r}\cos n\phi \tag{2.3}$$

$$J_\phi = n\frac{\partial F(r,z)}{\partial z}\sin n\phi \tag{2.4}$$

$$J_r = 0 \tag{2.5}$$

We now have an expression for J_z which has a cosine distribution as a function of the azimuth angle. Boundary conditions on $F(r, z)$ can be used to create a realistic winding geometry within the desired space of the magnet winding. As $\boldsymbol{J}$ is still continuous, we express $F(r, z)$ in a form which discretizes it into finite current paths, as this must be done to reflect a real winding. The condition for zero diameter discrete current paths existing on a thin cylindrical sheet at a constant radius can be described as Eq. 2.6

$$\boldsymbol{M}(\phi, z) = F(z)\sin n\phi = C_N \tag{2.6}$$

Where C_N is a constant defined by the number of turns per coil pole. The constant C_N takes the form of Eq. 2.7, in order to discretize the cylindrical sheet currents into N number of closed current loops with current I, which is a simplified case of a coil winding, as this creates N number of completely separate closed loops within the coil boundary on the cylindrical sheet.

$$C_N = \frac{i - 1/2}{N}I \tag{2.7}$$

The choice of F_n, which will be refereed to as the shape function, is discussed further in the next subsection. An example of a shape function used to generate the coil turns of a quadrupole using Eq. 2.1 - 2.7 can be seen in Fig. 2.1. Greater detail on the formulation of this style of coil geometry and on it's motivation can be found in Refs. [14]–[18].

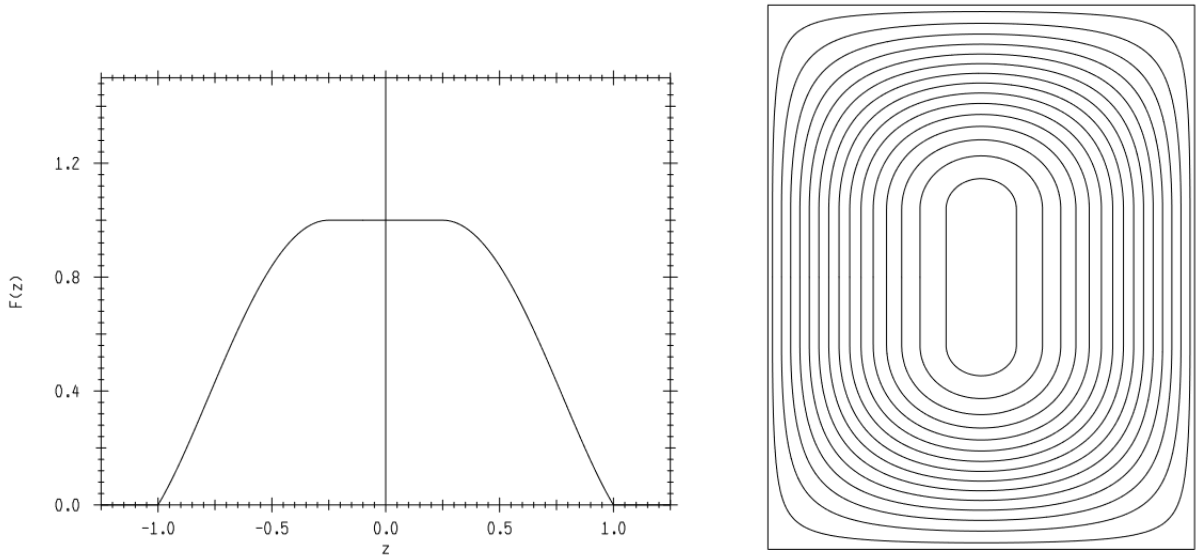

(a) (b)

Figure 2.1 a) Example shape function for a quadrupole of length 2 in arbitrary units. b) A quadrant of a quadrupole coil of length 2 in arbitrary units with 15 turns [13].

2.1.2 FRIB's CDQ

As discussed above the geometry of a DCT / Walstrom style coil, allows one to dictate the winding path through the choice of a shape function, $F(z)$. Through the use of Eq. (2.8), where z is the axial coordinate, ϕ is the azimuthal angle, n is the multipole order, and N is the total turn number a series of discrete parametric contours can be created which form the fundamental geometry of the winding. This shape function is used in Eq. (2.8) to create a set of parametric curves that will represent our current paths ie. our conductor paths for winding.

$$F(z)\sin(2\phi) = \frac{i-\frac{1}{2}}{N}, i = 1, 2, ..., N \tag{2.8}$$

The shape function is characterized such that $F(z) = 1$ in the straight sections of the wire. $F'(z) = 0$ at the very end of the straight section, and $F(z) = 0$ at the end of the winding. It is also necessary that $F(z)$ is continuous for physical windings to be properly represented. This can be achieved by using a piecewise function which satisfies these conditions, such as a common one outlined in Ref. [19]. The shape function used to generate the base geometry of the CDQ coil seen in Fig. 2.2. This generates a coil of the specified length and also generates coil's of radius 1 in

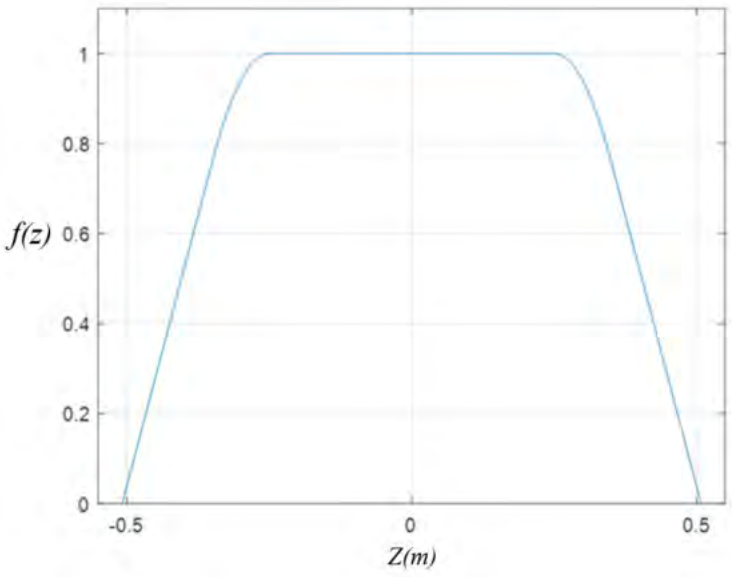

Figure 2.2 Shape function used to generate the base geometry for the CDQ coil winding.

arbitrary units. It can be useful to have the radius as 1, and then geometry can be scaled later to the desired radius. The choice of end winding geometry is based on the ends of our shape function, where we can choose our shape function, such that higher order harmonic terms are optimized when considering the end winding geometry. The introduction of realistic winding elements and real width conductors will always generate some higher order terms septate from the natural higher orders term which depend on the principal harmonic order of the coil. Once the base geometry of the independent terms are created, then the field solution can be analyzed before adding any more realistic elements, in order to verify aspects of the magnetic field generated by the coil.

2.2 Model Generation and Field Analysis

2.2.1 Analysis Technique

Once the base geometry is generated, we create a coordinate point file for the winding path. This file is then used for importing the geometry into a Finite Element Analysis (FEA) tool. Both CST Studio ® and COMSOL are used for magnetostatic simulations to analyze the steady state field. We design with a rough estimate of the necessary current needed for the field strength required at max, but parameter sweep over a range of the operating current to find the exact solution for field at warm bore radius. The results from the 2D model can be seen in Fig. 2.3, which shows a heat

map of the radial field intensity of the quadrupole package at the coil center.

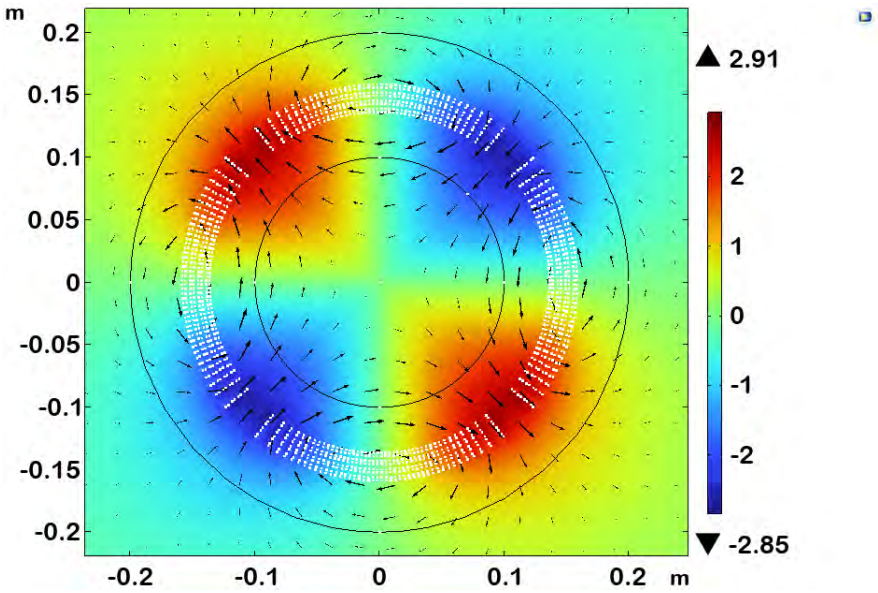

Figure 2.3 Distribution of the radial component of the magnetic field in the cross section of the magnet from magnetostatic model of CDQ magnet operating at 450 A [20].

The white dots in Fig. [20] are representative of the conductor, and it can be seen that the coil pack is composed of 4 groups of 2 conductors side by side. In order to keep the operating current under 500 A, we found that a design consisting of 8 concentric layers of 22 turns on a cylindrical sheet results in the desired field parameters. The variable radial spacing seen and the reason for 4 groups of 2 is due to the realistic spacing required for fabrication of cylindrical winding bobbins and will be discussed in more detail in chapter 4.

Once the field is simulated, we analyze it using a harmonic decomposition analysis. When expressed in cylindrical coordinates, the 2D field components, which are at a fixed radius along a circle, can be expressed in terms of a Fourier series of field harmonics. Expressing the B_r and B_ϕ in terms of field harmonics is shown in Eqs. 2.9, 2.10.

$$B_r(r_0, \phi) = \sum_{n=1}^{\infty} B_n(r_0) \sin(n\phi) + A_n(r_0) \cos(n\phi) \tag{2.9}$$

$$B_\phi(r_0, \phi) = \sum_{n=1}^{\infty} B_n(r_0) \cos(n\phi) - A_n(r_0) \sin(n\phi) \tag{2.10}$$

Where ϕ is the azimuth angle in cylindrical coordinates, B_n represents nth order normal harmonics, A_n represents nth order skew harmonics, r_0 represents the reference radius that the field is analyzed at, and n represents the harmonic index where $n = 1$ is the dipole harmonics, $n = 2$ is the quadrupole harmonics and so forth. The field harmonics can be expressed as a Fourier transform of the radial field component as a function of angle at a fixed radius, seen in Eqs. 2.11, 2.12.

$$B_n(r_0) = \frac{1}{\pi}\int_0^{2\pi} B_r(r_0,\phi)\cos(n\phi)d\phi, \quad n = 1, 2, 3, ... \tag{2.11}$$

$$A_n(r_0) = \frac{1}{\pi}\int_0^{2\pi} B_r(r_0,\phi)\sin(n\phi)d\phi, \quad n = 1, 2, 3, ... \tag{2.12}$$

A harmonic decomposition analysis is done on the field results to calculate the field harmonics. The field harmonics can then be used to calculate the quadrupole field gradient, effective length, integrated strength, and uniformity. The field harmonics are calculated from Eqs. 2.13 & 2.14.

$$B_n(r_0) \approx \frac{2}{N}\sum_{k=1}^{N-1}(B_r(r_0,\phi_k)\sin n\phi_k) \tag{2.13}$$

$$A_n(r_0) \approx \frac{2}{N}\sum_{k=1}^{N-1}(B_r(r_0,\phi_k)\cos n\phi_k) \tag{2.14}$$

$$\phi_k = \frac{2\pi k}{N}, k = 0, 1, 2, ..., N-1 \ [0, 2\pi] \tag{2.15}$$

The quadrupole field gradient can be calculated from the field harmonics and the reference radius. This relation can be seen in Eq. 2.16.

$$\frac{B_n}{r_0^{n-1}} = \frac{1}{(n-1)!}\frac{d^{n-1}B_y}{dx^{n-1}} \tag{2.16}$$

While $\frac{d^{n-1}B_y}{dx^{n-1}}$ is the mathematical gradient, we will refer to the entire expression of $\frac{B_n}{r_0^{n-1}}$ as the multipole gradient going forward for convenience sake. As this harmonic decomposition is a 2D analysis done at a reference radius, this analysis can be done at fixed steps along the beam line direction in a 3D model to obtain the harmonics as a function of the z-direction. We can

then integrate the harmonics with respect to z along the beam line direction. The bounds of the integration are such that your integration length must be sufficiently long for the field to approach zero outside of the magnet. Commonly, the z direction is integrated along the magnets total length plus 5 times the warm bore radius on each side. Once the field harmonics are obtained they can be used to calculate the field gradient at the center of the magnet and the integrated field harmonics, it then follows that the magnetic effective length, quadrupole integrated strength, and uniformity can be calculated from these values, shown in Eqs.2.17 - 2.20 [5].

$$L_{eff} = \frac{\int_{-z}^{z} B_2(r_0, z)dz}{B_2(r_0, 0)} \tag{2.17}$$

$$\frac{B_2}{r_0} = g \tag{2.18}$$

$$\frac{1}{2}\int_{-L_{eff}/2}^{L_{eff}/2} \nabla B(z)dz = gL_{eff} \tag{2.19}$$

$$\frac{\Delta B}{B} = \frac{\sum_n B_n - B_2}{\sum B_n} \tag{2.20}$$

The magnetic effective length refers to the region in the magnet that contributes to the motion of the beam particles. This is expressed as the integrated quadrupole harmonics divided by the quadrupole harmonic at coil center. It can be thought of as the effective length at which the bunch sees the center gradient. From this, one can then express the integrated strength as the center gradient multiplied by the effective length. The integrated strength gives a relation of the total focusing power of the magnet. The uniformity is simply a calculation of the percentage of the principle harmonic to the sum of all the harmonics calculated.

2.2.2 Model and Results

As discussed above, a point file is used to generate the winding geometry of the coil. Initially a simplified model can be made, where each turn is an isolated closed loop unconnected to each other, but realistic elements need to be implemented to see their effect on the field quality before a

finalized geometry for fabrication can be established. One of the desired elements for this design was to have all quadrants connected in series, which is a usual case for multipole operation. We found that a two-layer winding such that all quadrants were connected in series, and with the correct polarity, as one continuous conductor path could be used on a singular windings bobbin. Then, 4 bobbins could be assembled concentrically and spliced together in series. A 2D representation of this design can be seen in Fig. 2.4, and a 3D model used for defining the current paths can be seen in Fig. 2.5.

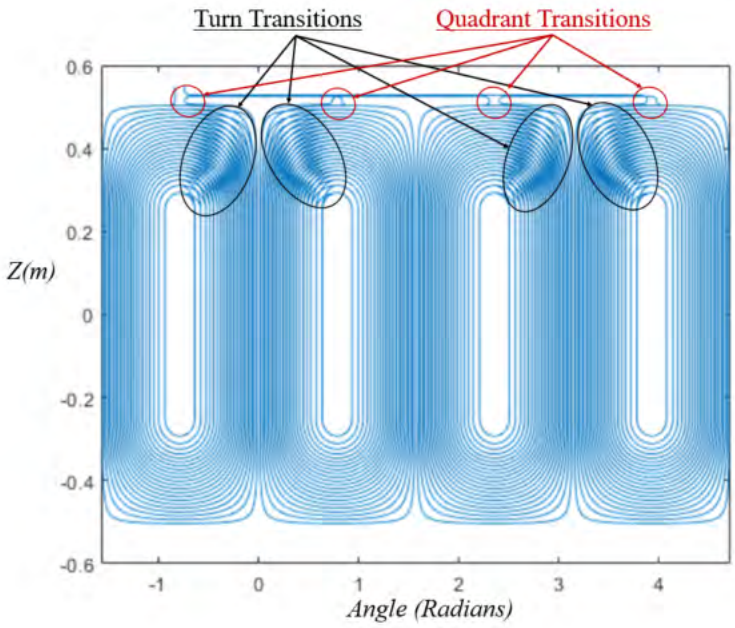

Figure 2.4 Plot of coil geometry represented in 2D plot of axial length versus angle, including turn to turn transitions marked in black and quadrant to quadrant transitions marked in red, [20].

A plot of the integrated harmonics normalized to the field sum can be seen in Fig. 2.6 from the magnetostatic simulation results. Beyond the uniformity calculation, it is important to observe what higher order harmonics contribute the most. Additionally, the results of interest for the steady state analysis can be seen collected in Table 2.1. Lastly, it is important information to see the quadrupole gradient plotted along the beam axis through the coil, to observe if there are any discontinuous or undesired effects from the simulation, this plot can be seen in Fig. 2.7.

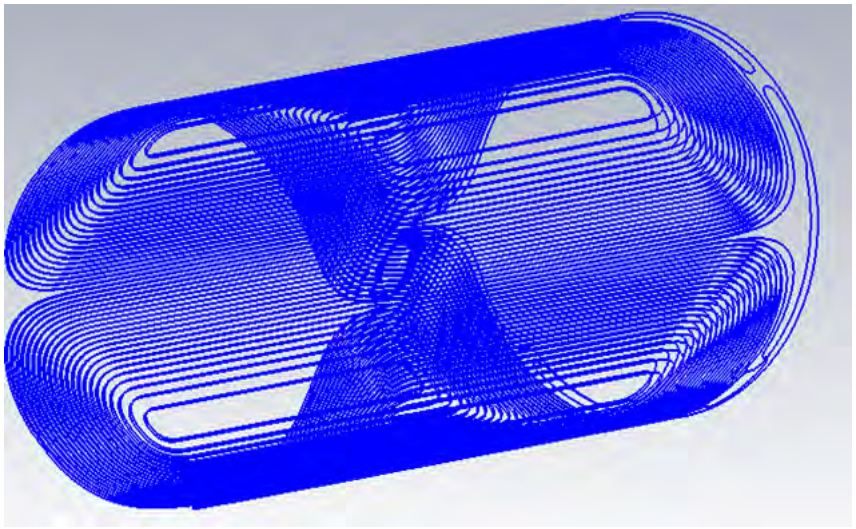

Figure 2.5 Image of 3D magnetostatic model in Both CST Studio ® of CDQ winding intended for a single bobbin.

Figure 2.6 Normalized integrated normal harmonics of the coil-dominated quadrupole design.

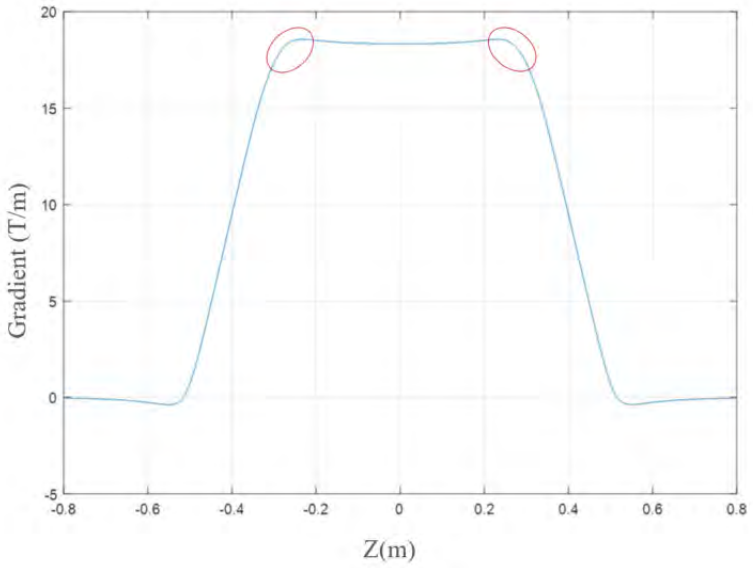

Figure 2.7 Plot of the quadrupole gradient along the beam axis. Red circles denote peak which we attribute to higher order harmonic effects to the end winding geometry [20].

Table 2.1 Design Parameters and Field Results[20]

Parameter	Unit	CD Type C
Operating Current	A	450
Amp-Turn	kA	316.8
Warm Bore Radius	m	0.1
Quad Gradient	T/m	18.3
Integrated Strength	T	14.7
Effective Length	m	0.8
Non-Uniformity	%	0.1
Max Field in Winding	T	2.9
Inductance	H	1.32
Stored Energy	kJ	134.3

2.3 Wire Selection and Stability Analysis

Before fabrication, a selection of the conductor must be made. As the intended conductor material for this winding was always planned to be Niobium Titanium (NbTi), a selection of the available conductors was done. We had a preference of a using a twisted cable for the winding the coil, out of a selection of different 4 wire twisted cables. A stability analysis was done for our options. A choice of cable type was made based on operating margin maximum, which are based on operating load lines, and geometric stability factors, such adiabatic stability and flux jumping. Based on these parameters, and the max field in the coil winding, an operating max of 800 A at 4. 2K was determined, giving a 54% operating margin at 4.2 K based on the 450 A required max and a temperature limit at 450 A of 6.6 K [21], [22]. These results can be seen from the operating load line in Fig. 2.8, and the conductor parameters can be seen in Table 2.2.

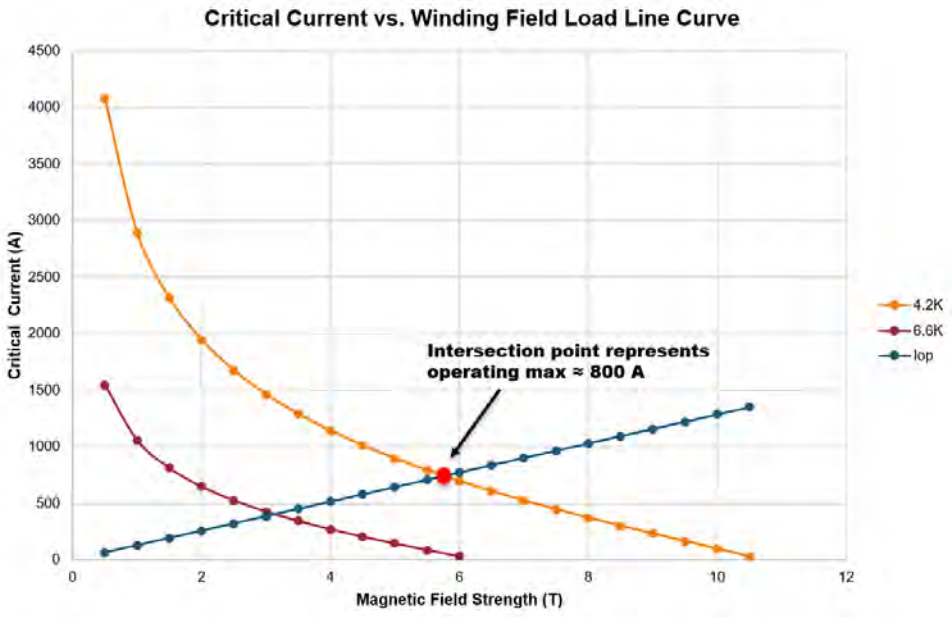

Figure 2.8 Operating load line for the chosen NbTi wire conductor that will be used for the CDQ winding. Orange line represents the critical current curve at 4.2 K, and red line is the 6.6 K.

Table 2.2 NbTi Conductor Parameters

Parameters	Unit	Chosen
Conductor Type	NA	NbTi
Bare Wire Diameter	mm	0.95
Insulated Diameter	mm	1.00
Filament Number	NA	54
Filament Diameter	μm	85
Cu:SC Ratio	NA	1.3
Critical Current @ 1.5 T	A	1330

2.4 Quench Analysis

A quench refers to the transition of a superconductor from the superconducting state back to a normal state. As operational stability is a large factor in magnet design and operation, it is insufficient to design for the stable scenario alone, the quench behavior must be understood well. Even a coil designed for good stability can still quench due to a number of operational issues than can occur, such as helium leaks or coil training. A simple quench circuit typically consists of quench detection based on the voltage across the superconducting coil, then a switch connecting the coil to the power supply is opened and the current in the coil is then forced through dump resistor until all of the coil energy has been dumped. A simple diagram of the quench circuit used for CDQ magnet for analysis is shown in Fig. 2.9. It is important to know what the max temperature of the

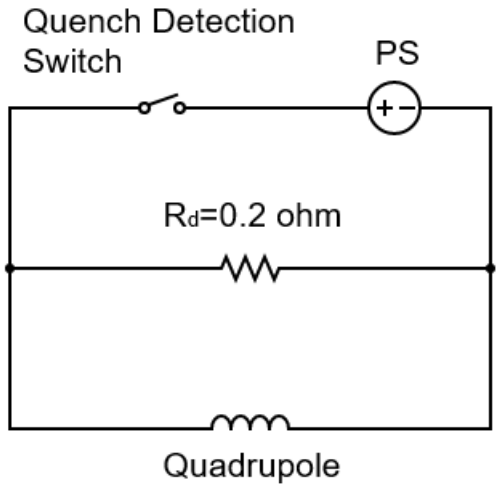

Figure 2.9 Quench circuit diagram for CDQ coil.

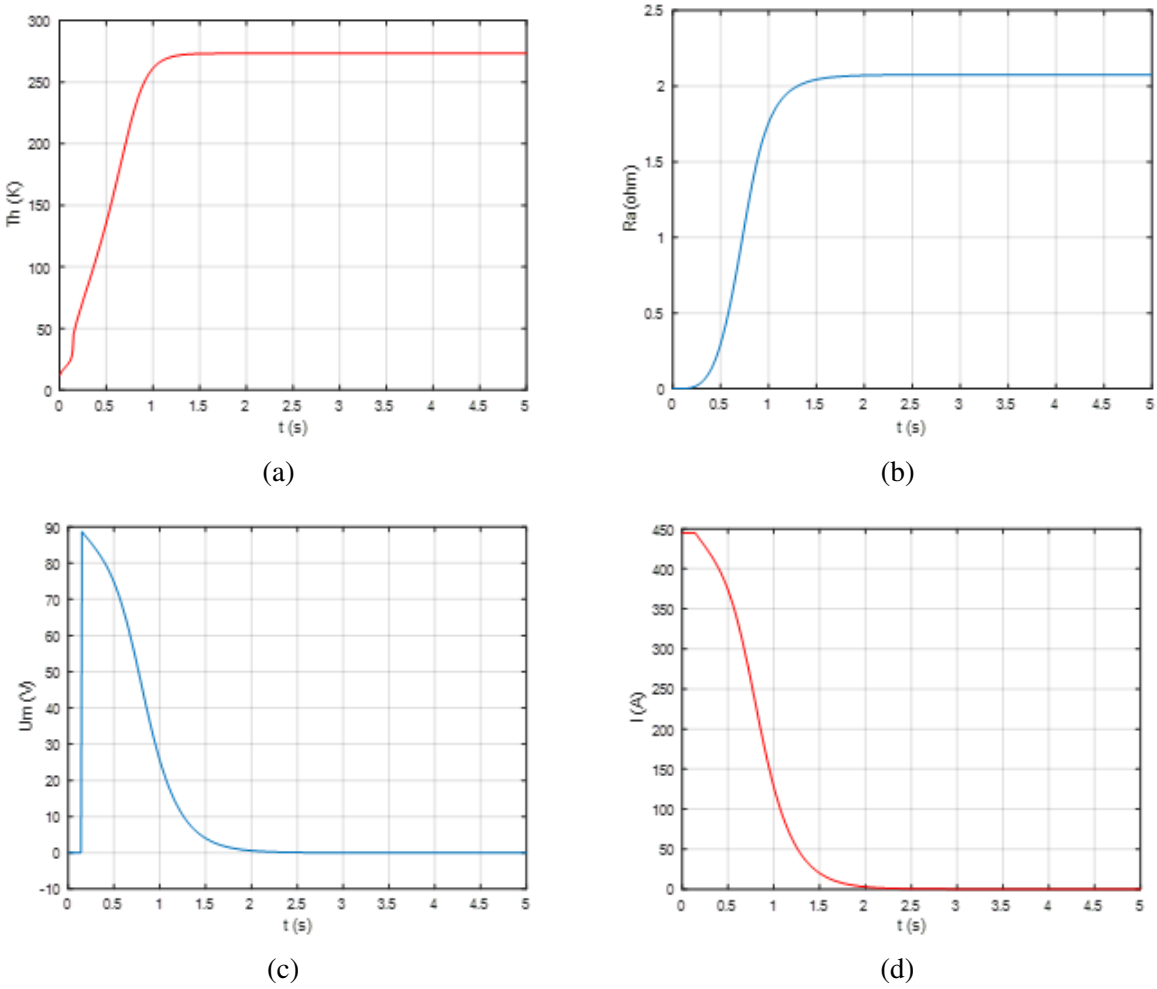

Figure 2.10 a) Plot of the temperature of the coil during a quench. b) Plot of the resistance growth from normal zone propagation during quench. c) Plot of the coil voltage during quench. d) Plot of the current decay of the coil during quench [23].

coil will be, the power delivered from the normal zone, and the voltage of the coil as a function of the current decay. A quench analysis was done on the CDQ coil for a dump resistor of 0.2Ω. The results of this can be seen in Fig. 2.10.

The following chapters will discuss the optical impact of this coil design on a section of the fragment separator of FRIB, the fabrication of a single layer testing prototype, and the testing and field mapping results of the prototype coil at 450 A.

CHAPTER 3

BEAM STUDY CHAPTER

3.1 Facility for Rare Isotope Beams

The Facility for Rare Isotope Beams (FRIB) is a facility whose aim is to use heavy ion beams which reach up to 200 MeV/u energy for uranium and up to 320 MeV/u for lighter ions such as oxygen-16, neon-20, argon-26, to create many of the rare isotope predicted to exist. FRIB consists of an ion production front end, a superconducting linear accelerator (linac), and a fragment separator. Additionally a Re-accelerator (ReA6) will be utilized for further nuclear physics experiments and a series of upgrades such as a high rigidity spectrometer (HRS) and an energy upgrade up to 400 MeV/u for uranium and 463 MeV/u for lighter ions are planned to expand FRIB's research capabilities. FRIB's primary accelerator is a superconducting linac. The linac consists primarily of Quarter Wave Resonators (QWR) and Half Wave Resonators (HWR), which are superconducting radio frequency (SRF) cavities, but in the front end a radio frequency quadrupole (RFQ) is utilized for acceleration of the beam up to 0.5 MeV/u. The energy upgrade to 400 MeV/u for uranium (FRIB400) will implement a series of 5-cell elliptical SRF cavities as well. The linac consist of 3 separate linac sections which are then connected through folding segments to form a "paper clip" shape. This shape can be seen in Fig. 3.1 [9].

3.1.1 Linac

The linac is divided into 3 linear segments and 2 folding segments: these are Linear Segment 1 (LS1), Linear Segment 2 (LS2), Linear Segment 3 (LS3), Folding Segment 1 (FS1), and Folding Segment 2 (FS2) respectively. LS1 accelerates the beam up to energies of 20 MeV/u and consists of 14 total cryomodules, 3 of which each contain four QWR and 11 of which contain 8 QWRs all operating nominally at 80.5 MHz. Each cavity voltage and phase can be individually adjusted as well for beam tuning. LS2 similarly consists of two cavity types, and consists overall of 24 cryomodules. FS1 begins with a series of quadrupoles which bring beam to desired size for the charge stripping station, and a rebunching cryomodule for charge stripping station requirements. A series of quadrupoles downstream then readjusts the beam size again. The charge stripping

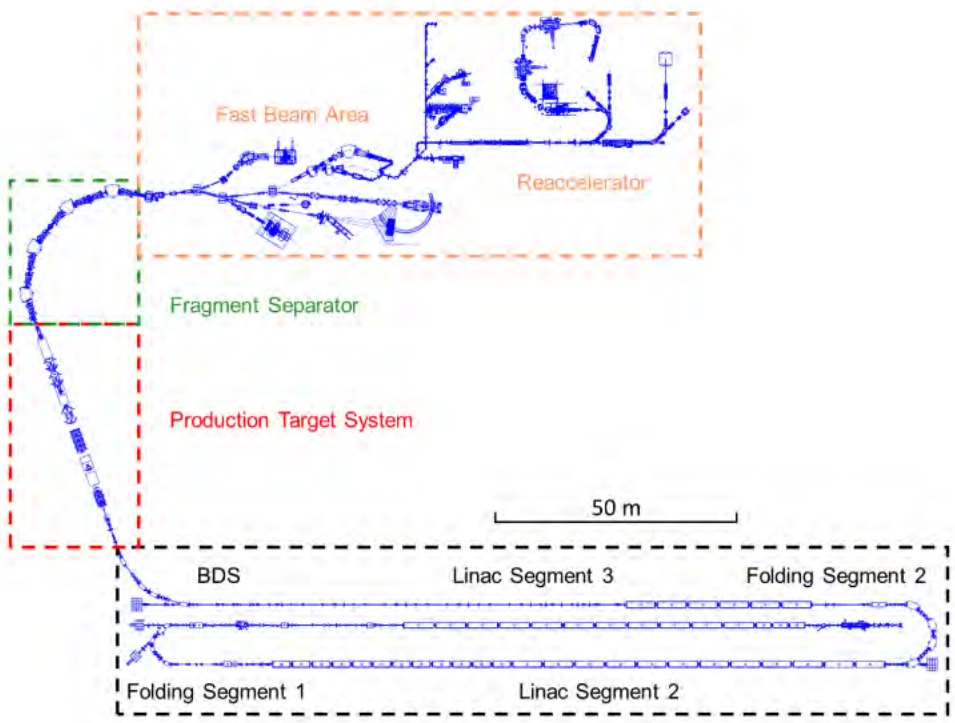

Figure 3.1 Diagram of FRIB layout including linac portion, production target system, fragment separator, fast beam area, and re-accelerator [9].

station is a liquid lithium film where 85% of the uranium produced through the station have charge states of +76 to +80. The LS2 bending dipoles are superconducting coils that can be energized up to 2 T. The bending segment also contains combined magnets of quadrupoles and sextupole, which go between bending dipoles to compensate for the chromatic effects. LS2 consist first of 12 cryomodules, each containing 6 HWRs all operating at 322 MHz, these are then followed by an additional 12 cryomodules containing 8 HWRs each also operating at 322 MHz. Each cryomodule also contains an emittance compensation solenoid, which can be energized up to 9 T. FS2 has a very similar layout of magnets to achieve another 180° bending segment after LS2. LS3 contains 6 cryomodules that complete the acceleration up to 200 MeV/u. A diagram of these aspects of the superconducting linac can be seen in in Fig. 3.2. LS3 is then followed by a transport section which will be utilized with more cryomodules for the FRIB400 upgrade. There is a 70° segment with 4 dipoles to steer the beam towards the target [9], [24], [25].

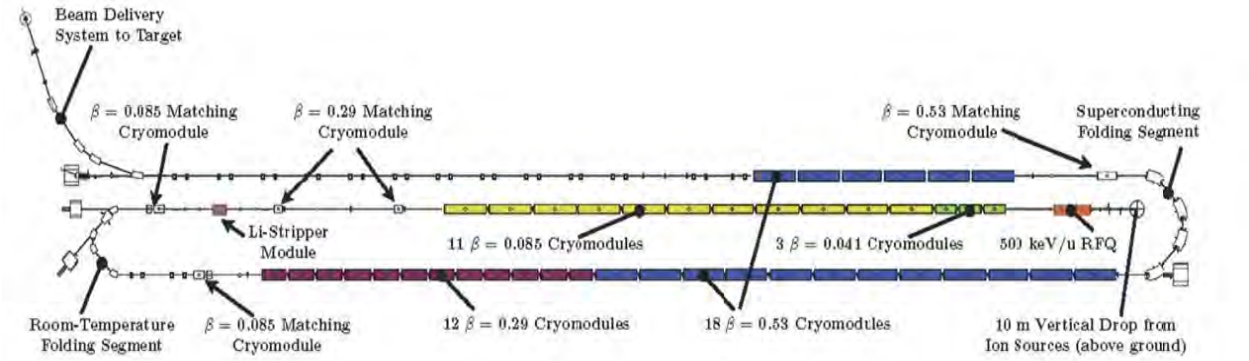

Figure 3.2 Diagram of FRIB's Superconducting Linac [24].

3.1.2 Advanced Rare Isotope Separator

The fragment separator of FRIB, known as the Advanced Rare Isotope Separator (ARIS), is used to separate out the isotope species of interest from all of the species created from interaction of the primary beam with the target. The angular acceptance of ARIS is ±40 mrad and momentum acceptance of ±5%. ARIS is designed for a 3.5-8 Tm beam rigidity. ARIS consists of 3 stages, a pre-separator for the initial separation of the different isotope species. Stage 2 and 3 then provide further separation to ensure a very pure secondary beam of the rare isotope(s) of interest. The pre-separator brings up the beam from the underground level to the ground level of the facility, in addition, the use of dipoles in these vertical bends also help spatially disperse the different species in the beam. The pre-separator consists of 4 dipoles, 4 quadrupole triplet packages, and 6 stand alone quadrupoles. The pre-separator layout can be seen in more detail in Fig. 3.4. The portion of the pre-separator from the target to the first energy degrader is the front end of the separator. The front end exists in a hot cell, and all magnets are designed to operate in high radiations environments. The energy degrader is used to separate out the beam mass and compress the momentum spread of rare isotopes of interest to the required phase space. After the first dipoles in the pre-separator, there is also a beam dump for the primary beam, after produced isotopes are separated by dipoles. The magnets used are all superconducting, with the dipoles and quadrupoles used are iron-dominated, while the sextupoles and octupole are saddle coils nested inside of certain quadrupoles. The sextupoles and octupoles are to provide correction to chromatic effects, which will be discussed in more detail in the following section [9]–[11].

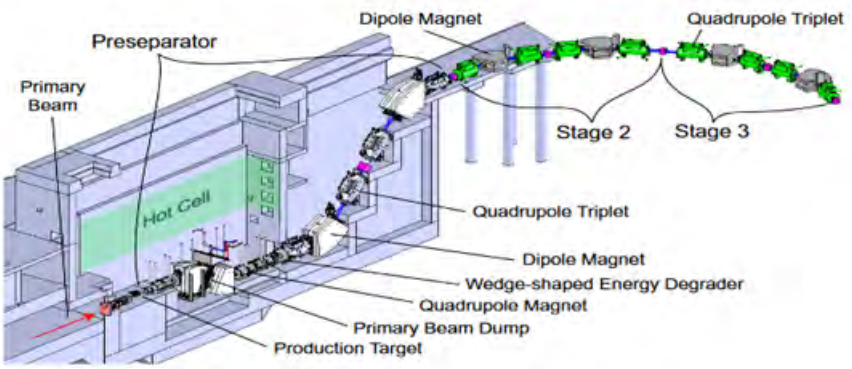

Figure 3.3 Labeled model of Advanced Rare Isotope Separator (ARIS) [9].

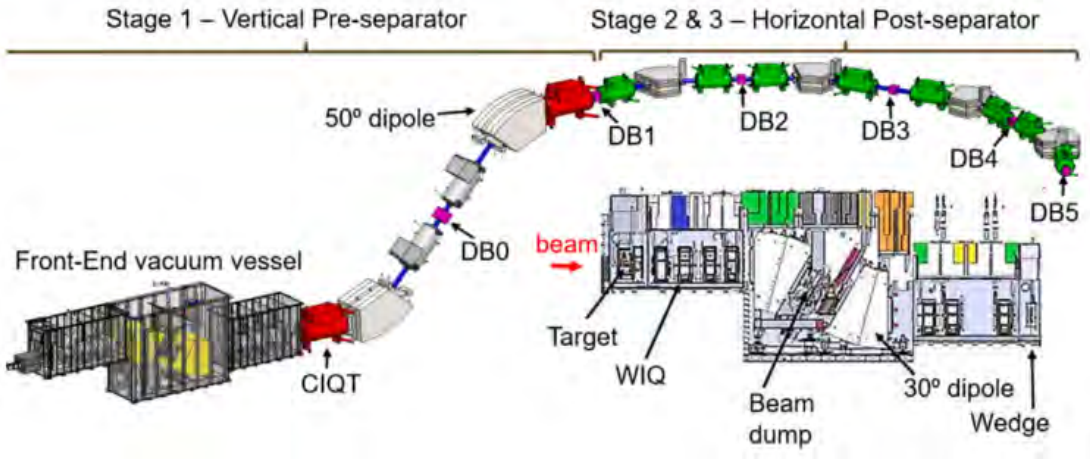

Figure 3.4 Diagram of ARIS including diagram of hot cell pre-separator area (lower right) [11].

3.2 Sextupole Kick Optics

Sextupoles are an important component for optical corrections in accelerators systems. Sextupoles help to correct chromatic aberrations [1]. In the process of acceleration, while the average energy of the particles may be the target acceleration energy, there exists an energy distribution in the bunch, which results in a change in focal length which is dependent on energy. This results in lower energy particles being over-focused and higher energy particles are under-focused. Sextupole magnets are used as chromatic correctors to give all particles the same focal length.

Available space along the beam line can be very precious for many facilities. Sextupoles can have their own dedicated positions in the beamline, but it is not uncommon to pair them concentrically with other magnets in a module in order to save space along the beamline, especially if it is known in advance that a chromatic corrector will be necessary. In certain circumstances this

Table 3.1 Separator Stage 2 & 3 Magnets.

Parameters					
Type	FSQA	FSQB	FSQC	FSQD	FSQE
L_{eff} (m)	0.723	0.4	0.79	0.486	0.7
Full Aperture (m)	0.2	0.2	0.2	0.34	0.23
Quad Max Grad (T/m)	13.2	17	14	11.9	16.6
Sext. Max Grad (T/m^2)	NA	9.6	6.8	NA	NA
Oct Max Grad (T/m^3)	NA	48.9	48.5	NA	NA

pairing can cause issues. One of these circumstances being when, a sextupole is paired with an iron-dominated quad. In order to have multiple magnets operate in the same portion of beamline, they need to be mated concentrically. For an iron-dominated quadrupole the size of the iron yoke can restrict the placement of the sextupole. Requiring it to be the inner magnet for design, efficiency, and practicality. A sextupole's poles will not align with a quadrupole's poles due to differences in symmetry order. Due to this when the sextupole draws flux from the iron yoke due to it's proximity, this will generate a dipole harmonic in addition to the quadrupole and sextupole. This term can be either acceptably low or unacceptably high, depending on the design of both the quadrupole, sextupole, and the operational requirements of the facility. Some magnets of the fragment separator of FRIB suffer from this issue.

A portion of FRIB's fragment separator consists of 4 dipoles, 24 quadrupoles, 16 sextupoles, and 16 octupoles [9]. In this portion all 16 sextupoles are paired with a quadrupole. This portion corresponds to Stage 2 and Stage 3 of Fig. 3.3. This portion of the beamline works as a good example for showing the impact of this sextupole induced dipole component on the optics of the separator.

This portion corresponds to Stage 2 and Stage 3 of Fig. 3.3. This portion of the beamline works as a good example for showing the impact of this sextupole induced dipole component on the optics of the separator. The optical lattice of this portion of the separator can be seen in Fig. 3.5. Each letter in the lattice diagram corresponds to it's Fragment Separator Quad (FSQ) model, and the parameters of each quad package can be seen in Table 3.1. The strength of the dipole component induced by the sextupole can be seen in the harmonic analysis of the field. This dipole component

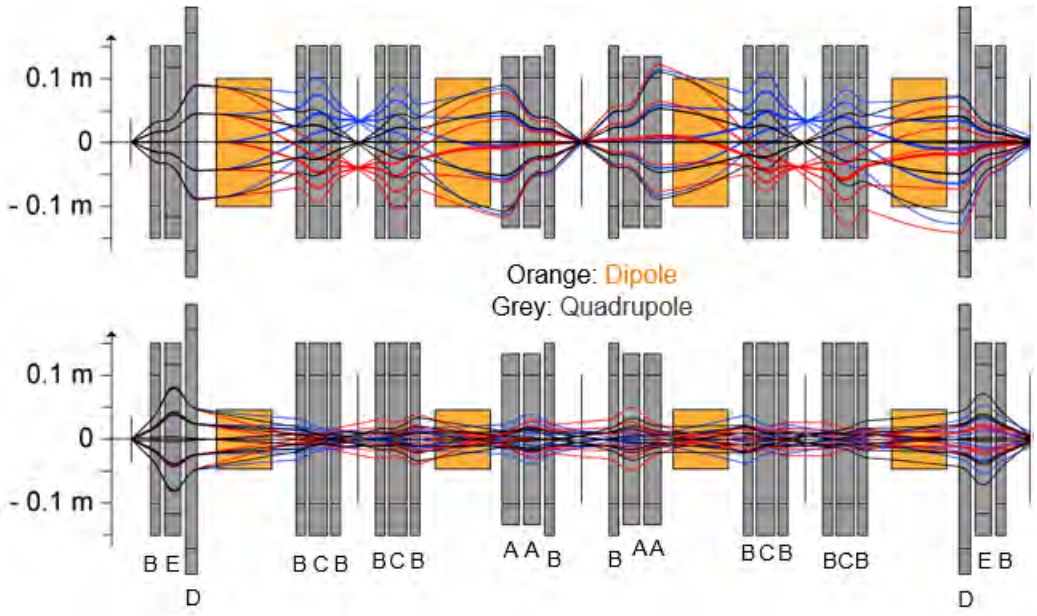

Figure 3.5 Dispersive (top) and non-dispersive (bottom) plane primary beam through the second and third stages of ARIS, in 5th order approximation. The angle spread is ± 31 mrad in x and ± 35 mrad in y. The blue and red corresponds to the off-momentum beams, which are ± 2.3% of ideal magnetic rigidity [9].

has been observed in both simulated results and experimental mappings of sextupoles at FRIB. In Fig. 3.6, one can see that the dipole harmonic is about 20% of the principle sextupole harmonic at the center of the magnet. This has a non-negligible impact on the optics of the beam portions of magnet with this induced dipole.

To further clarify the optical impact of this effect, it can be incorporated into the beam simulation of the fragment separator portion. The fragment separator lattice has been simulated using COSY INFINITY [26]. This effect was incorporated into the COSY code, by taking the integrated strength of the dipole component and evaluating the dipole kick strength based on the operating beam rigidity. The kick is then split into two parts, half of the kick when the beam enters the magnet and half when the beam exits the magnet. Additionally, the magnetic effective length, L_{eff}, of the magnets changes based on operating current due to saturation effects of the iron. The effective length as a function of sextupole coil operating current was estimated using FEM Magnetostatic solver of CST Studio, and the results of this can be seen in Fig. 3.9. The beam envelope with and without this effect considered can be seen in Fig. 3.7, and the deviation from reference orbit from

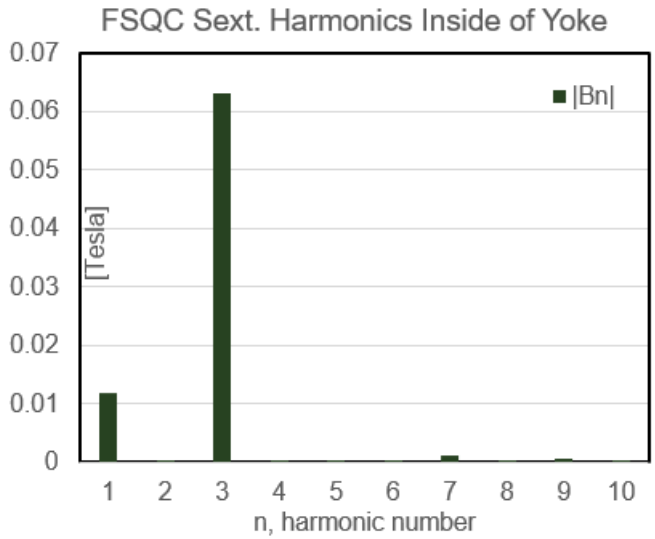

Figure 3.6 Example harmonics of a sextupole of FRIB's FSQC magnet package.

this effect can be seen in Fig. 3.8

An analysis of the impact on the phase space of the beam was also studied. It was calculated that over the entire lattice the mean dispersive momentum had changed by about 7 mrad from first order calculations and about 4 mrad from a 5th order calculation. These are large enough shifts that correction would be required during operation. This simulation shows the impact this effect has on Stage 2 and 3 of the separator, but it can be seen from Fig. 3.10 that this dipole harmonic is even stronger in the CIQT magnets of the pre-separator due to required sextupole strength, meaning that the kick from these magnets is even stronger. Eliminating this effect is advantageous to operation, and eliminating the large iron yoke greatly reduces the tuning times that can be achieved from the magnet, even when including the iron collars which act as fringe field shields for the magnet.

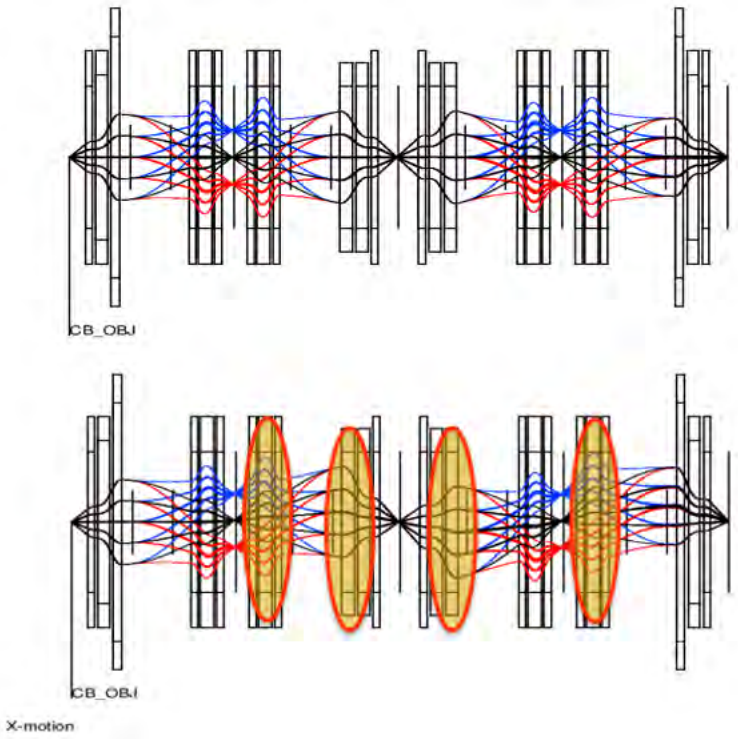

Figure 3.7 Top is a plot of the simulated beam envelope along intended trajectory of the fragment separator. Bottom is the beam envelope when the sextupole induced dipole kick is considered, with the highlighted areas are locations of the most significant deviation from reference orbit. The blue and red corresponds to the off-momentum beams, which are ± 2.3% of ideal magnetic rigidity and both plots are of the dispersive plane.

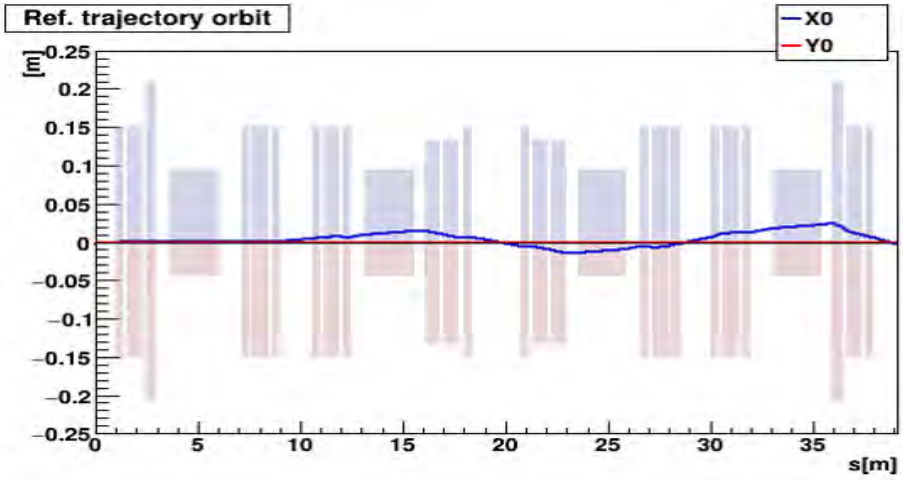

Figure 3.8 Plot of the deviation from reference orbit based on the effect of dipole component induced by sextupoles.

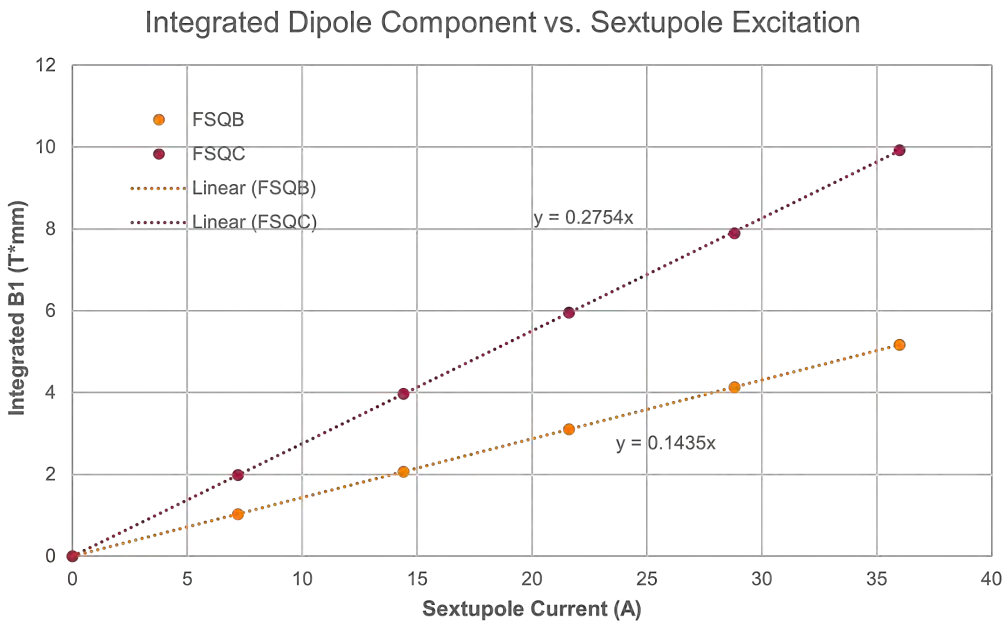

Figure 3.9 Plot of sextupole magnetic effective length of FSQB and FSQC as a function of operating current.

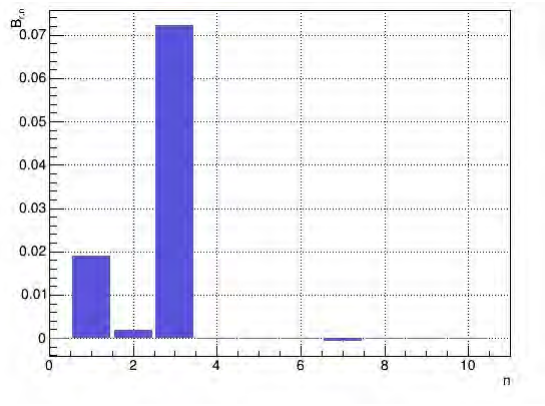

Figure 3.10 Measured harmonics of FSQ7 sextupole at maximum excitation [27].

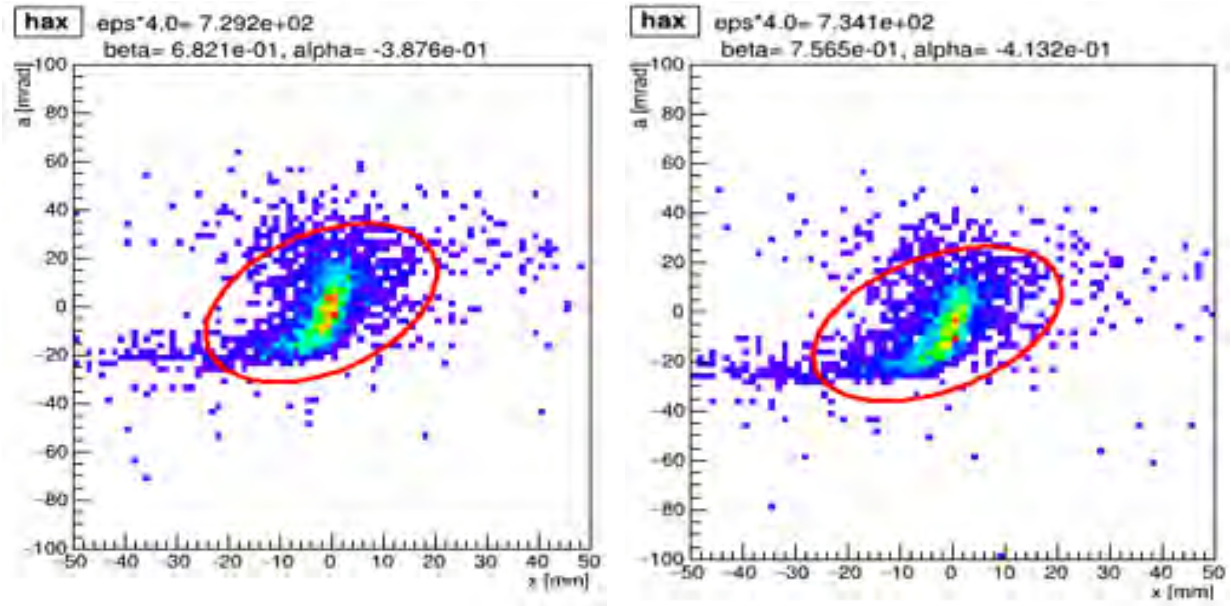

Figure 3.11 Plot of 5th order phase space in the kick plane. Dipole effect unconsidered (left) and dipole effect considered (right). Where a shift in the mean x-momentum of about 6.8 mrad occurs, and a shift of about 1 mm in the x position occurs.

CHAPTER 4

COIL FABRICATION AND DEVELOPMENT

4.1 Winding

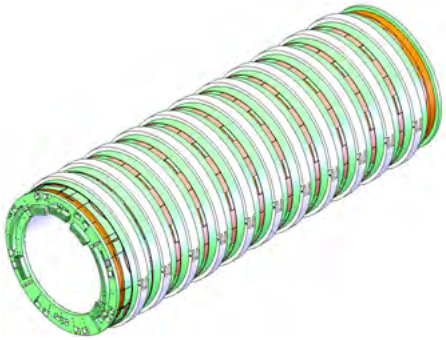

(a)

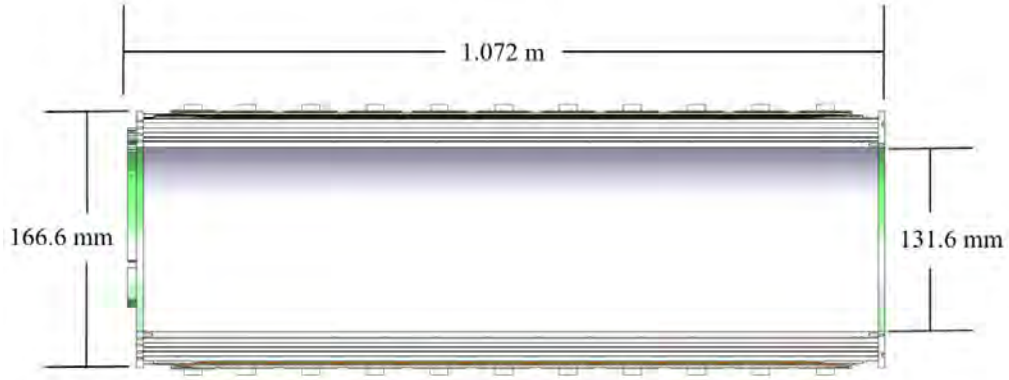

(b)

Figure 4.1 a) Isometric view of conceptual quad package assembled. b) Cross sectional schematic view of conceptual quad package assembled [20].

The quadrupole winding was achieved via a direct winding method. The direct winding for the DCT was achieved by machining a pathway for the cable strand to follow on a cylindrical winding bobbin. The winding bobbin is made of 6061-T6 aluminum [28]. This aluminum was chosen as opposed to a strong insulating material like G10 in order to implement an optional conduction cooling scheme to the magnet that could be explored in the future to reduce the use of liquid helium. Aluminum also helps to spread heat during the quench to improve the time it takes to reach equilibrium temperature. The entire quadrupole package would consist of 4 bobbins nested

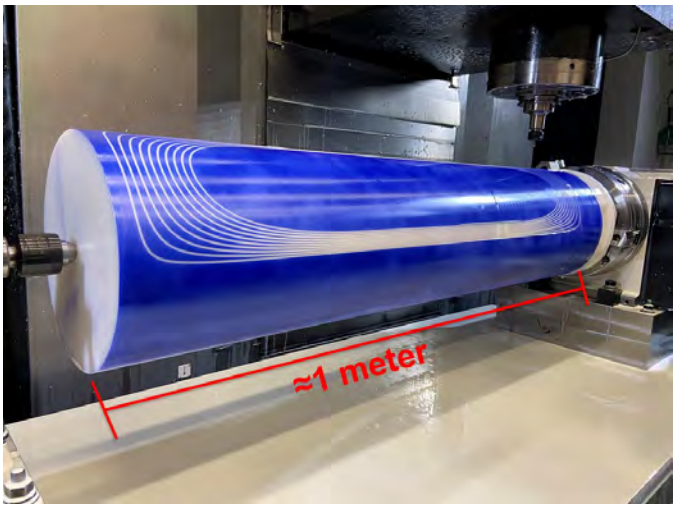

Figure 4.2 Practice machining of winding path on full scale plastic cylinder. Only the 10 outer turns are machined for practice winding.

concentrically, seen in Fig. 4.1. Each bobbin we call a super-layer, as it is a partial layer of the full package. Each bobbin consists of 2 layers of NbTi twisted cable, the wire parameters, stability and operating margin of our chosen wire was discussed previously in Chapter 2.

Initially, the intended winding pattern for the coil is machined onto a sub-scaled flat plate. Multiple flat sample pieces are machined all with varying path widths in order to make sure that the winding path has both enough depth and width to properly accommodate the twisted cable. If the width is too small the conductor cannot be placed properly into the groove and either will not fit or may be damaged when trying to submerge it into the groove. If the width is too large then the winding can become difficult to execute due to wire stiffness, and excess space leads to poor restriction of conductor motion. Once sizing is determined, a large scale test piece can be machined for practice. A plastic cylinder the same radius as the intended winding bobbin was used to test machine the winding path on a cylindrical surface to ensure that winding path could be machined as intended with desired accuracy. This form was then used for some practice winding to quality check the machining work.

Practice winding is done in order to identify any issues that may appear during the actual winding, and to ensure that the winding path can properly accommodate the conductor. Based on feedback from the practice winding during this part of the bobbin development, geometry changes

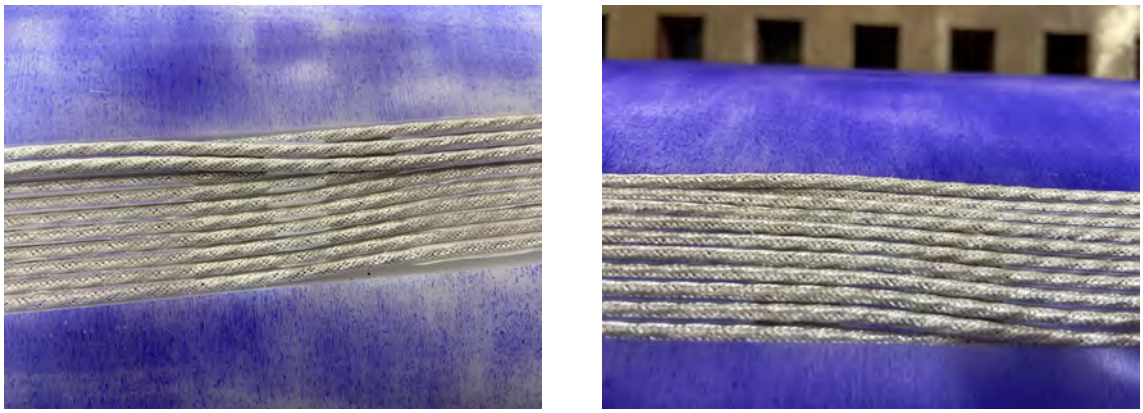

(a) (b)

Figure 4.3 a) Turn to turn transition area can be seen in first and second layer. (b) At the top of the transition area the additional overlap of conductor can be seen due to the winding path design.

Figure 4.4 New location of the turn to turn transition area demonstrated on a sub-scaled flat prototype winding [20].

were made to the turn to turn transitions of the winding geometry due to an unwanted overlap of conductor in a portion of the winding. In Fig. 4.3a, the transitions from turn to turn can be seen. In Fig. 4.3b, this unwanted overlap of conductor can be seen and results in conductors going above the surface of the winding fixture. It was considered more favorable to adjust the position of the turn to turn transitions, rather than leaving the overlap. The adjustments impact on field quality was still within the design requirements.

It was found that moving the turn to turn transitions from the mid section to the end sections was more favorable, and still allowed for ease of winding. This path was then tested with the sub-scaled 2D piece seen in Fig. 4.4 to observe any issue with the winding form. Once found acceptable, the full quadrupole winding path was then provided to a Computer Numerical Control (CNC) machine technician to convert the winding path into the machining tool path as was done previously for the plastic winding cylinder.

The final winding form is a 6061 aluminum cylinder which has the winding path machined into it

(a)

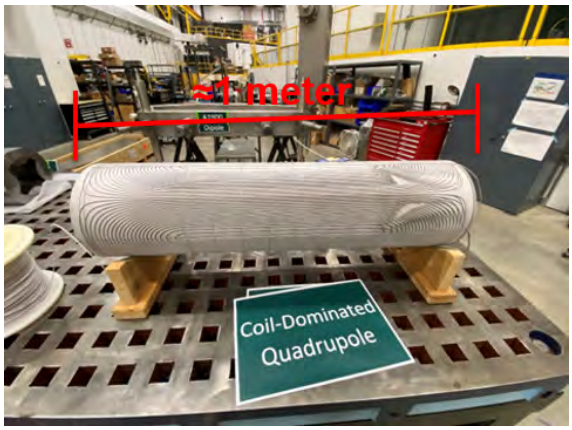

(b)

Figure 4.5 a) Completed machining of winding bobbin for first super-layer of CDQ package. (b) Sand blasted bobbin to treat sharp features before surface treatment [29].

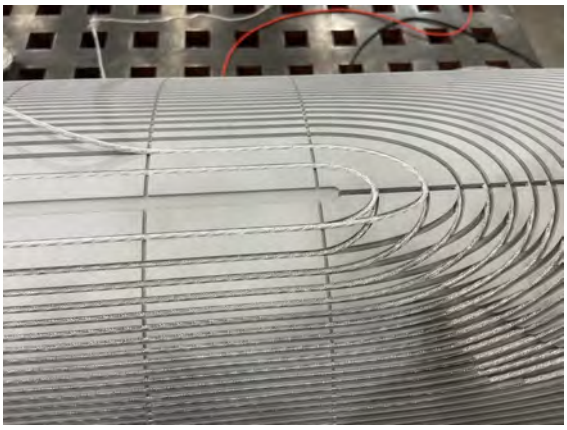

(a)

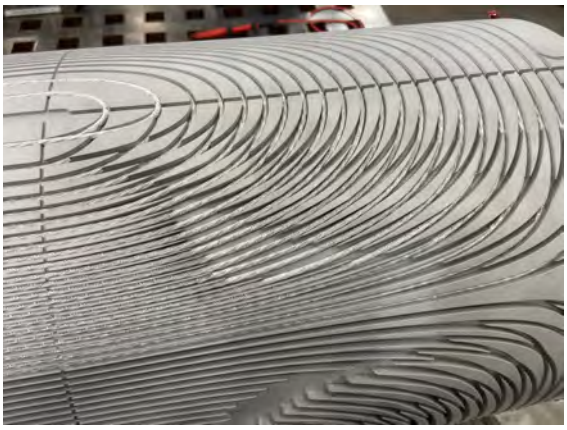

(b)

Figure 4.6 a) Practice winding of full scale winding bobbin. (b) turn-to-turn transition area of full scale winding bobbin.

via a CNC machine. The bobbin is then inspected through a Coordinate Measuring Machine (CMM) to measure the eccentricity, axial straightness, and winding path depth and width consistency. The first completed full scale bobbin can be seen in Fig. 4.5. Once the machining is considered acceptable, a practice wind is then done on the bobbin as part of the inspection and also to gain technical practice with winding on this piece. After practice winding is completed with satisfaction, the bobbin then needs to be surface treated before attempting the real winding.

To assure good electrical insulation between the winding bobbin and the conductor the 6061 Al bobbin is surface treated with an insulating material. Initially, an electrodeposition or "E-coating"

Figure 4.7 Winding bobbin after electro deposition of zinc phosphate "e-coating" completion, the bobbin is then placed on the winding table for real winding of quadrupole.

of zinc phosphate was applied to the winding bobbin to electrically insulate it. The E-coated bobbin can be seen by the now black surface of the bobbin in Fig. 4.7 [30]. Once surface treatment is completed the winding process begins. The winding process was done by two persons, and the bobbin allows for the winding of a quadrupole super-layer via one continuous winding to reduce the number of electrical splices necessary. It was found that the zinc phosphate layer would electrically insulate the bobbin up to 1000 V, but could be scratched off during the winding process due to abrasion and added challenge to complete the winding without creating electrical short between the wire and the bobbin. This resulted in several failures during the winding process, due to an electrical short between the conductor and bobbin. Any exposed areas from abrasion were treated with either a thin layer of Stycast manually or treated with thin layer of kapton. Due to this challenge, the surface treatment for successive bobbins was changed to a hard coat anodization of aluminum oxide [31]. Hard coat anodization is an electrochemical process which involves passing current through the metal fixture and caused a deposition of oxygen on the surface, which forms a hard coat of aluminum oxide on the outer surface. This material offered a good compromise of abrasion resistance and electrical insulation. It was found that aluminum oxide anodization offered electrical resistance up to 700 V, less than that of zinc phosphate, but was much more abrasion resistant and

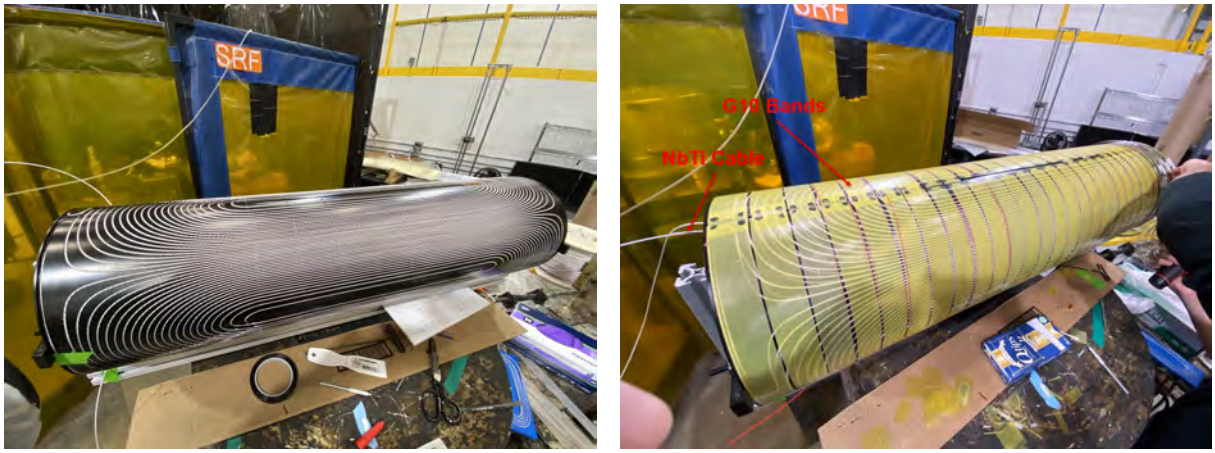

(a) (b)

Figure 4.8 a) Completed winding of E-coated bobbin, now ready for preparations for electrical splicing and impregnation. (b) Completed winding with G10 overbanding strips fastened to the bobbin to keep wires contained during preparations for splicing and impregnation.

offered an easier winding. As a successful winding was completed with zinc phosphate e-coated bobbin this winding was used for sub-scale testing process. The completed winding can be seen in Fig. 4.8.

Once winding was completed the bobbin was then banded with G10 strips, seen in Fig. 4.8b, to ensure good containment of the wires while the form was prepared for the electrical splicing of the lead wires and the vacuum impregnation process.

4.2 Electrical Splicing

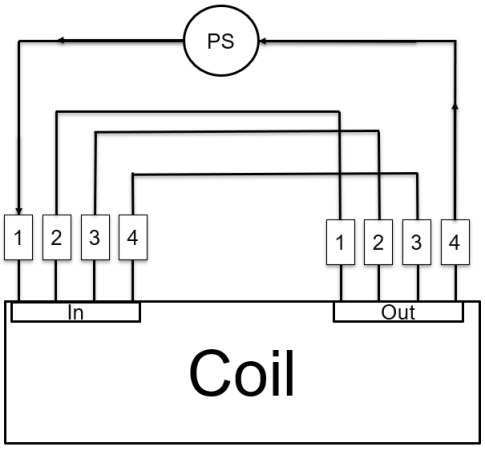

Figure 4.9 Diagram of the coil splicing to achieve a series connection between the four wires of the NbTi cable used for winding.

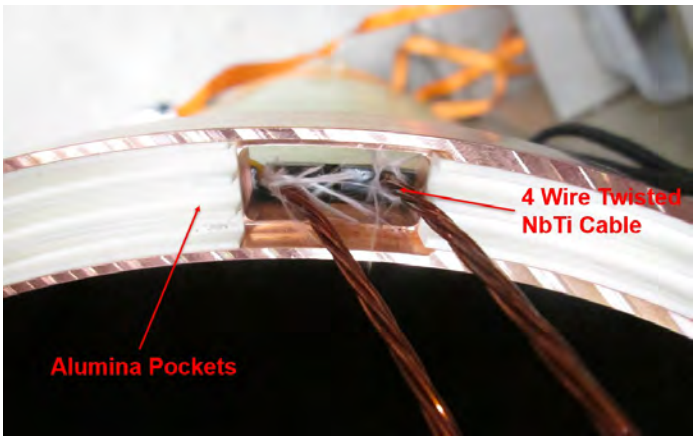

Figure 4.10 Lead in and out of the coil before being spliced and placed into alumina pockets.

The goal of the electrical splicing is to take each of the four wires of the NbTi twisted cable and connect them electrically in series such that there exists one wire which is the current in and one wire which is the current out. These two leads drive excitation of the entire quadrupole package, a diagram of this connection can be seen in Fig. 4.9. The entrance and exit of the leads are directly next to each other in the bobbin. The end flange which connects to the bobbin has an outlet hole for the leads along with a pocket machined into it. This pocket is to house the splice area and will be impregnated later to contain the splice section. The pocket allows for an aluminum oxide (alumina) insert which has a sleeve for each individual wire splice to be place to insulate them from each other. The isolating pockets of alumina can be seen in Fig. 4.11. Alumina is chosen as an insulating material because it has a relatively high thermal conductivity for ceramic insulators, on average 30 W/mK. Thermal conduction to the splice area is important to adequately compensate for any Joule heating in the splice area from the soldered joint, and increasing the thermal conduction to the splice is also important for later implementation of conduction cooling scheme.

The splice takes the first wire from the lead out bundle and then connects it to wire 2 of the lead in bundle. They are connected via a standard 63% tin and 37% lead (36Sn63Pb) electrical solder. Additionally, when the wires are soldered together they are soldered to an additional strip of NbTi wire, which is 5 mm wide and 8 cm long, that serves as additional stabilizer to help draw away heat. An additional 24 AWG copper wire is also soldered in each splice to use as a voltage tap to monitor the voltage across each layer of the coil. The splice section is then covered with a polyethylene

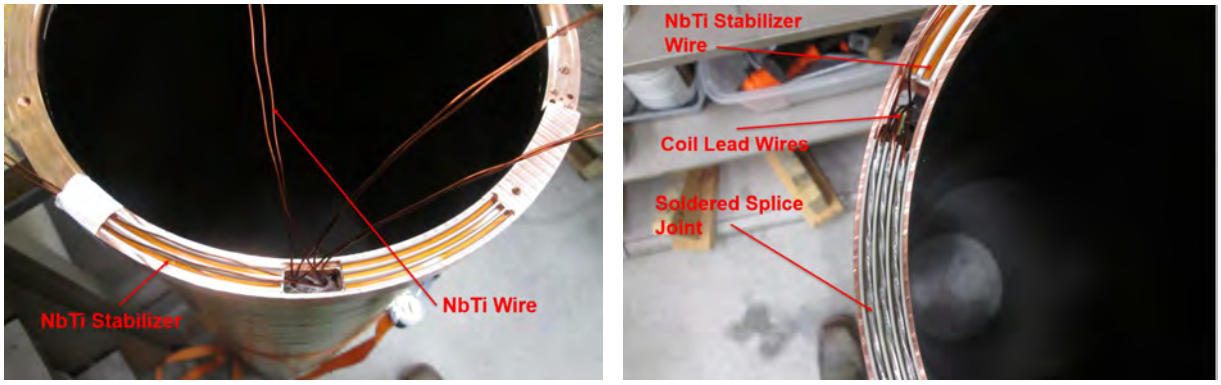

(a) (b)

Figure 4.11 a) NbTi stabilizer placed inside of the alumina pockets for sizing and preparation of lead splicing. b)Partially completed splicing of the leads placed into their insulating pockets.

heat shrink tubing for additional protection and isolation, and then placed in the alumina pocket. This process is done for each wire of the cable until you remain with one lead in wire and one lead out wire. Once the electrical splicing is complete, it is then checked for electrical isolation to the winding form. With the completion of the electrical splicing, the coil is then ready for vacuum impregnation preparations.

4.3 Vacuum Impregnation

Generally, coil impregnation is the process of filling the coil space with a binder, which then hardens and binds all of the conductor strands in place and fill the voids between conductors in order to minimize and ideally prevent any conductor movement during operation. Preventing conductor motion helps to prevent a quench during operation of superconducting magnets [21]. A variety of binders have been used for impregnation of superconducting coils. Typically most impregnations use some form of epoxy resin, but materials such as paraffin wax still have use in impregnation systems. For this quadrupole magnet, we decided that a Vacuum Pressure Impregnation (VPI) would be best for the design. The grooves would make a wet winding very difficult to fill the voids, especially the voids between conductors underneath the insulation. The drawback is that VPI provided challenges as this was our first attempt at impregnating this coil style. VPI is the practice of putting the coil filler form in a vacuum pressure space, approximately 500 mTorr or lower, and filling the coil space with a resin epoxy while both are under vacuum pressure. This

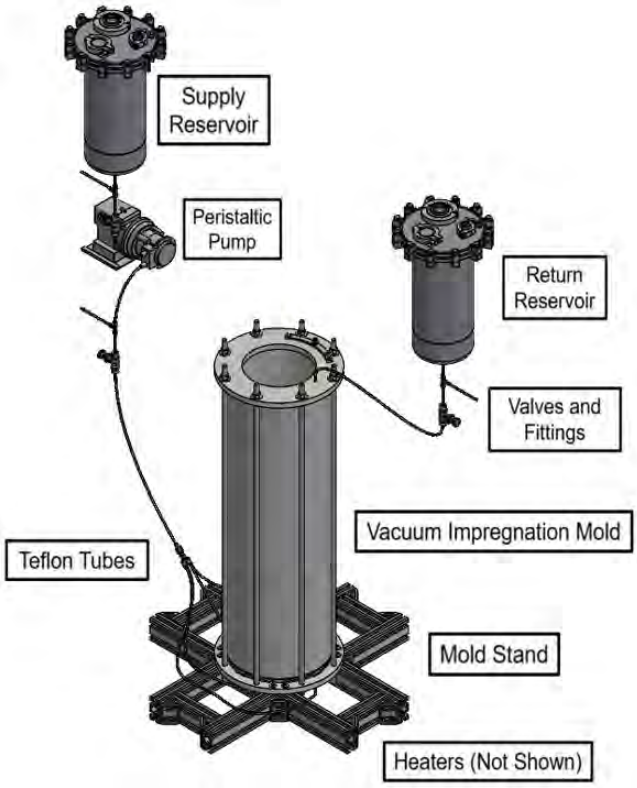

Figure 4.12 Design of conceptual model of vacuum pressure impregnation of setup for CDQ single layer coil winding prototype. Same technique can be applied to each individual super-layer [32].

process can allow for the coil assembly and epoxy mixture to degas separately before flow is started. Degassing both sufficiently before flow starts helps to ensure that no air bubbles or void form in the epoxy during the curing process, as voids can result in epoxy cracking once the coil sees magnetic force. This can lead to more training quenches due to loose areas of conductor [33]. The process for VPI that we chose to pursue was the use of a supply tank for mixed epoxy, a vacuum space for the coil, and a return tank to help ensure that epoxy filling was good, along with additional fiberglass insulating cloth wrapping the magnet which helps serve as both electrical insulation and flow medium for the epoxy resin [34]. The conceptual design of the vacuum impregnation system can be seen in Fig. 4.12.

4.3.1 Preparation

Typically, a vacuum furnace is employed for the VPI of magnetic coils, as we did not have access to a vacuum furnace, the VPI design deviated from a more "traditional" VPI system [35]. Traditionally, a coil is put into a filling form for the resin to fill the coil space. Then that form is

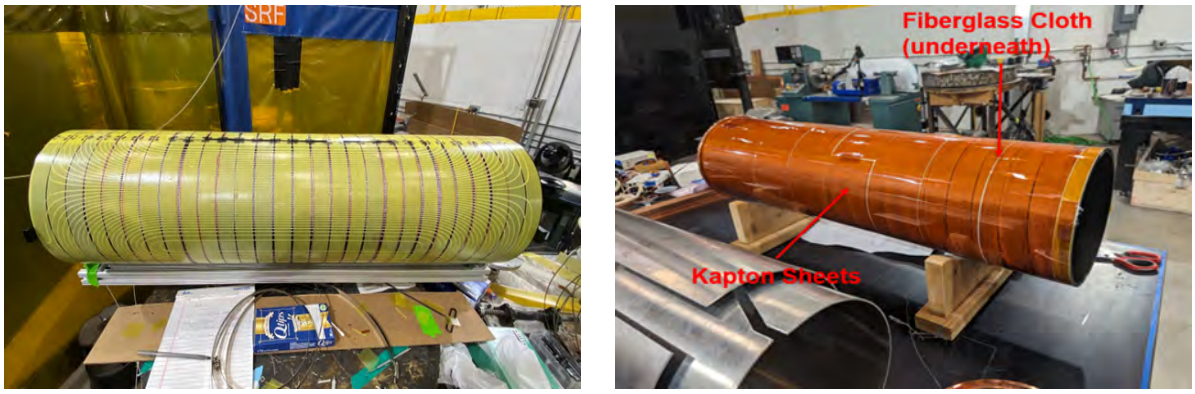

(a) (b)

Figure 4.13 a) Bobbin overbanded with G10 strips for wire containment. b) Fiberglass and kapton wrap of coil winding for insulation and protection.

put inside of a vacuum furnace. Instead of this, a shell was equipped around the coil and sealed to serve as both the filling form for the resin and also as the outer wall of the vacuum space for the coil. Further detail is provided in the proceedings subsections.

Preparation process for the coil is as follows. The overbanding is slowly removed as the coil is wrapped in fiberglass cloth, once wrapped in one layer of fiberglass cloth the coil is then wrapped over with bands of kapton. The overbanding and kapton wrap can be seen in Fig. 4.13a and Fig. 4.13b respectively. Then, 1/8 inch thick aluminum bands are prepared which will provide radial pre-load to the structure to contain the radial forces of the coil during energizing. Banding pre-load is achieved through having each band fitted to the bobbin and then clamped tightly, once clamped the seam of the band is then welded and the welding shrinkage provides the radial pre-load to the structure.

4.3.2 Force Constraints

The banding thickness is determined through a force analysis of the coil. The maximum force on the coil during it highest operating current is determined as an initial estimate of the necessary constraints for the magnetic forces of the coil, we found the total force to be on the coil body to be 22.2 kN at 450 A. A plot of the 450 A static stress in a symmetric slice of the constraining structure can be seen in Fig. 4.14. After an initial estimate and design for the mechanical constraints an analysis must be done for the force on the coil structure in the case of a quench. The constraining

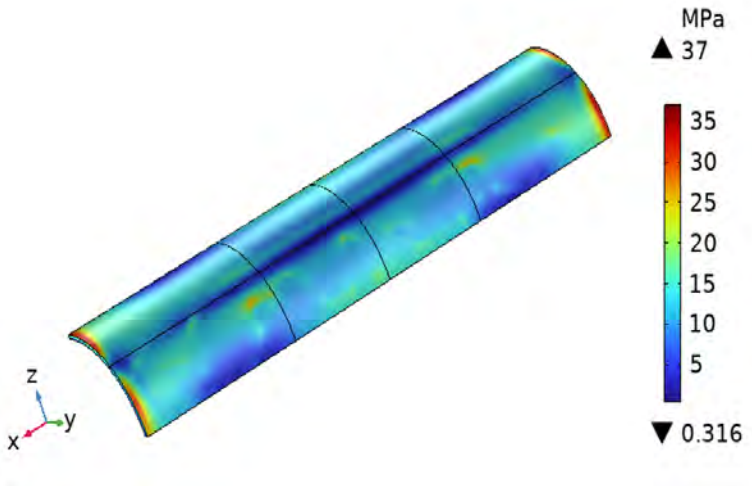

Figure 4.14 von Mises stress in symmetric quarter of 1/8 inch thick constraining shield at 450 A static case [36].

structure in most cases is made of metal, this means that when a quench occurs the change in magnetic flux through the constraining structure will produce eddy currents in the constraining structure proportional to the time derivative of the current [37]. The forces due to inductive response can be greater than that of the coil forces at max field, so making a constraining structure which can handle these forces is crucial for magnet operation stability.

The current decay curve from the quench analysis can be used with the inductance of the coil to simulate multiple points in time during the quench and analyze the forces. As the rate of change in current is highest right a the beginning of the quench we expect for this to be when the highest forces are seen. Based on highest force during quench we check that the von Mises stress does not exceed the tensile stress such that there is no permanent deformation of the restraining shell. A plot of the maximum stress during a quench along with the current density in the shield can be seen in Fig. 4.15. The maximum stress during quench reaches approximately 90 MPa, whereas the tensile stress is 240 MPa, therefore there will not be any deformation to the shield. Additionally, the axial strain was found to be sufficiently low as to not deform the conductor.

In order to have a higher safety margin in our constraining structure it was decided that the thickness of the constraining shield would be doubled to 1/4 inch. The structure was then divided into two layers each of 1/8 inch thickness. The inner layer which is constructed of multiple

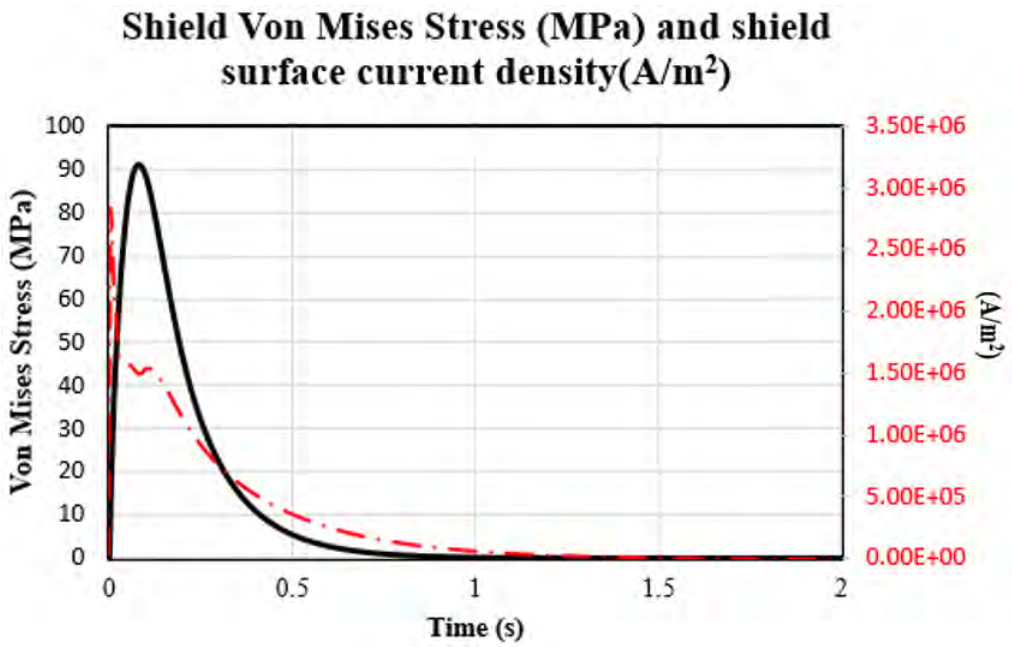

Figure 4.15 Plot of the maximum von Mises stress in the constraining shell and the surface current density in the aluminum shell versus the time of a quench [36].

aluminum bands, and an outer structure which is on continuous aluminum shell the entire length of the coil form. The inner layer is separated into bands which are insulated from their neighbors for the purpose of minimizing the inductive currents loop, which helps to minimize the forces from inductive response during quench. The outer layer is one shell piece, because the outer layer must also serve as the vessel which will seal the coil in a vacuum space for impregnation.

After the first layer of banding is fitted to the magnet and the weld seams are ground to be flush with the surface, the second layer is fitted on. The second layer consists of one aluminum shell which is the length of the entire coil bobbin. In the same manner as the first layer the shell is clamped tightly around the coil assembly and then the seam of the shell is welded to pull tightly around the coil and reduce the space between layers. This process can be seen in Fig. 4.16. After this is completed the sealing process for impregnation vacuum space begins.

(a) (b)

(c) (d)

Figure 4.16 a) Bobbin overbanded with G10 strips for wire containment. b) Fiberglass and kapton wrap of coil winding for insulation and protection. c) Test fitting of first layer banding. d) Full length coil picture with test fitted bands [29].

4.3.3 Impregnation

The ends of the Al shell are sealed through a silicon calk used on the interface between the Al shell and the end flanges of the coil. This calk seals the internal space of the coil such that it can be pumped down to vacuum pressure internally for VPI process later. The leads of the magnet are then placed in a polyline sleeve and sealed around the base of the lead via a silicon calk as well.

The coil is fitted onto the VPI stand once it is sealed. The coil is mounted to the stand via two plates that are mounted to the top and bottom of the coil. The plates are clamped to the ends of the coil assembly tightly via a threaded rod arrangement on the inner diameter of the coil, which can be seen in the assembly shown in both Fig. 4.17 and Fig. 4.18. These plates are equipped with the inlet and outlet ports for the polyline which will flow epoxy through the impregnation system.

Then wrapping heaters were equipped on the outside of the shell and then a reflective fiberglass blanket is wrapped around in order to maintain the temperature of the heaters seen in Fig. 4.19, to get the entire mass to the required temperatures for the various steps of curing. The curing process is determined by the type of epoxy used for impregnation. The epoxy chosen for impregnation was CTD-101k because it is intended for cryogenic use, it has a long pot life (60 hours at 40°C), low viscosity (less than 100 cP at 60°C), low toxicity, good adhesion to fiberglass, and has a good history of being used for a variety of magnet systems with vacuum impregnation of coils being one of it's intended uses [38]. The VPI process is as follows: 1) CTD 101k components are mixed according to the vendor instructions. 2) The mixture is then put into the inlet tank and degassed at 60°C until the mixture is observed to be static through view port of inlet tank. 3) The valves of the flow lines are put into the open position and 300 Torr of pressure is slowly let back into the inlet tank to facilitate epoxy flow through the system. 4) The first quarter of the solution is bled out any partially mixed epoxy that is concentrated near the bottom of the tank. 5) With the magnet in a vertical position the epoxy flows from the bottom through the coil space, through the splice area, and then up into the outlet tank. 6) Once 1/3 of the total mixture of epoxy is observed in the outlet tank flow valves are closed to stop epoxy flow because the coil space is sufficiently filled. 7) The form is then heated up from 60°C to 80°C and held for 24 hours. 7) The final process of curing is then that the temperature is brought up to 135°C and held for an hour, then allowed to cool back to room temperature to conclude the impregnation process.

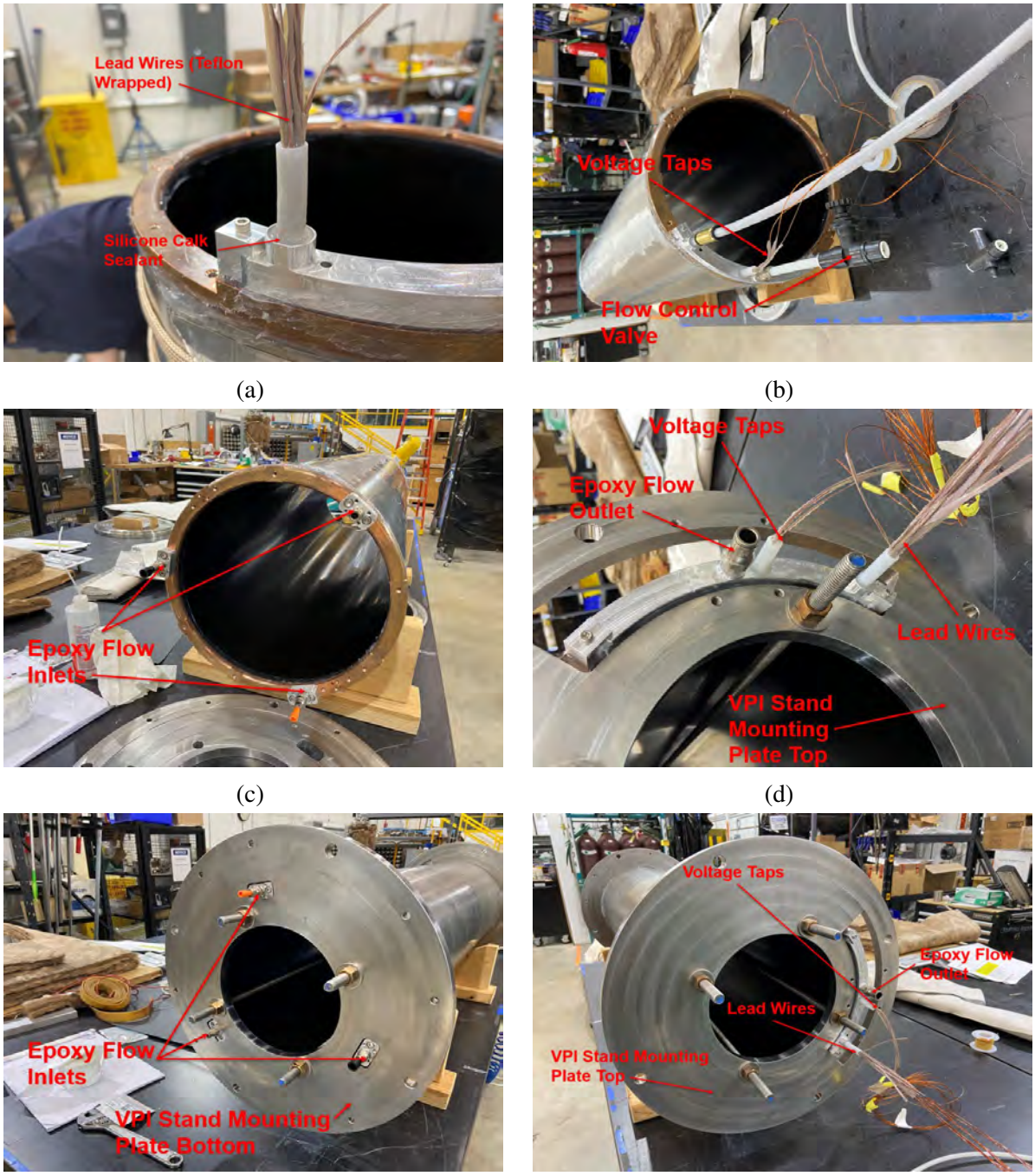

Figure 4.17 a) Aluminum piece used to cover the splice, seal the leads, and guide epoxy flow. b) View of bottom flow inlets. c) Coil mounting plate at the coil bottom. d) Splice after completed prep. e) Mounting plate connected to bottom of the coil. f) View of the entire top mounting plate [29].

Figure 4.18 Picture of CDQ single layer coil fully prepared for vacuum impregnation [29].

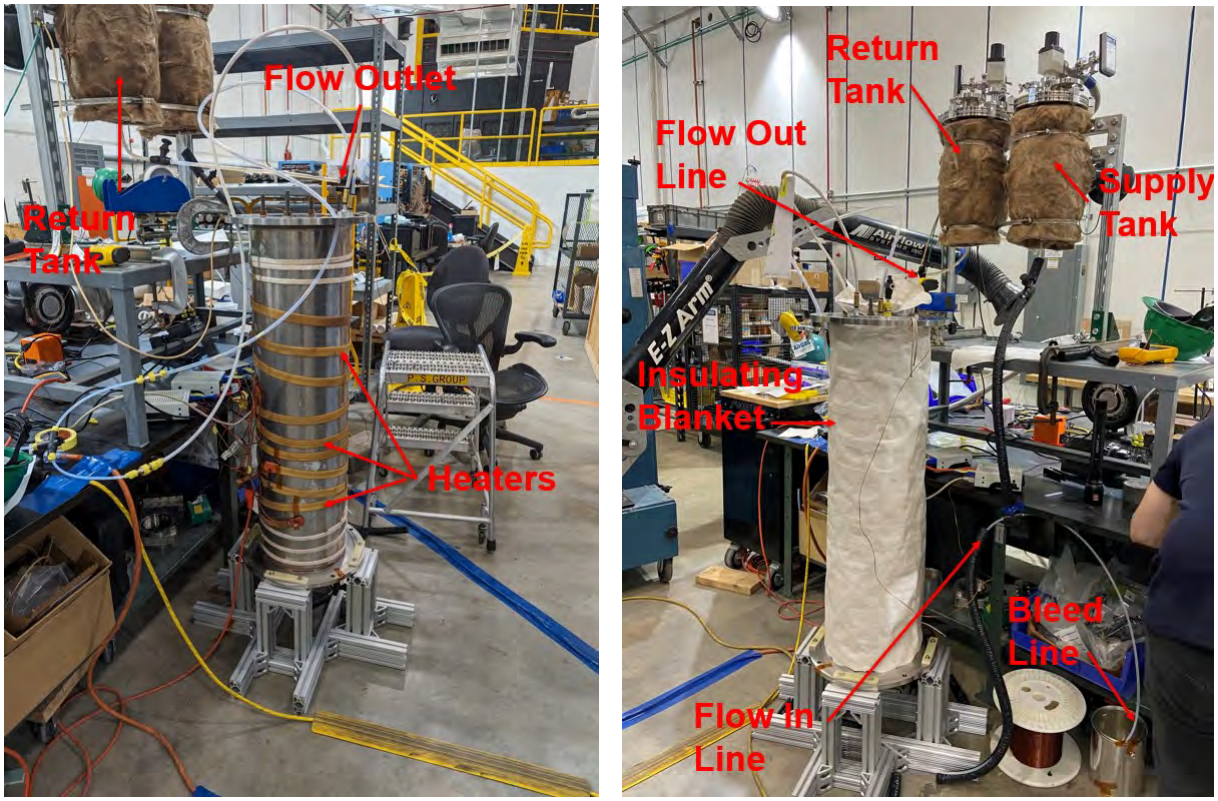

(a) (b)

Figure 4.19 a) Picture of fully connected impregnation system ready for initial heating and degassing. b) In progress vacuum impregnation of CDQ single layer coil [29].

4.4 Post Impregnation Inspection

After impregnation the coil is inspected to assure that the wire and the winding body are electrically insulated from each other. Due to the need to seal the leads during the impregnation process the electrical insulation could not be monitored during the impregnation. Once checked afterward it was found that there was an electrical short between the wires and the winding body. The coil lead splicing was then carefully dug out of the impregnation epoxy using a soldering iron and splicing was undone in order to diagnose which wire(s) are shorting to the body. It was found that only one of the 4 winding wires was shorting to the body. The diagnosing of the wires can be seen in Fig. 4.20.

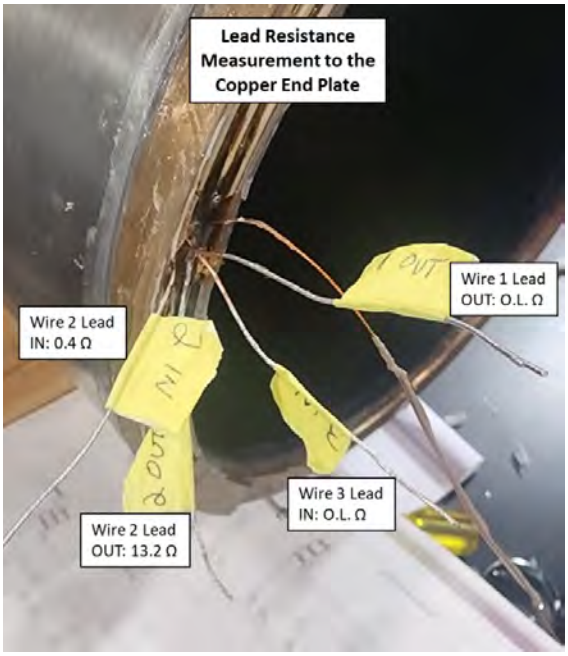

Figure 4.20 Inspection of lead wire electrical short of quadrupole coil.

After identification of the electrical short was complete, the shorting wires leads were isolated and kept separate from the other wire leads. The remaining 3 wires are then spliced back together in series in the same manor and the splice region needs to be impregnated again for operation stability. The splice region after being reworked is impregnated with Stycast epoxy manually. This means that the turn number of the coil is reduced by 1/4 uniformly throughout the coil. This still allows for cold testing and training, but field strength and forces will now be 3/4 of the predicted

maximum of the design. While unfortunate, the stability of the coil can still be tested at 3/4 of the maximum field strength and the field strength can be verified at compared to a simulated result at 3/4 of the maximum excitation. In addition, the measure of the uniformity and harmonics of the coil can still be measured as well. After the completion of this electrical work and confirmation that no electrical short exists the coil is then mounted into the testing structure for first training test in liquid helium.

CHAPTER 5

TEST SETUP AND RESULTS

5.1 Testing Assembly Overview

The CDQ cold test setup was designed with two operating options in mind. The first was to design such that a conduction cooling scheme could be implemented to the coil for future research and development. The second was to allow for the use of LHe for initial testing and as an alternate option in the case of low performance from conduction cooling. With conduction cooling in mind the test setup was designed to use a two stage cryocooler to achieve cool down of the cold mass to the superconducting state as well as using the first stage as a thermal intercept for current leads and a radiation shield. The additional criterion needed was a testing setup that would fit and work with the available testing Dewar, ability to use the cryocooler in liquid testing to help intercept heat, and the ability to map the magnetic field.

The coil would be tested in a vertical orientation, and a hanging assembly anchored to a central top flange would be used. Two circular copper plates would be used for the thermal intercepts of the cryocooler and the current leads. The testing setup was designed to accommodate a magnetic field measurement system for verifying the field quality of the coil. The simplest method would be to use a series of Hall probes designed for operation in a 4 K environment. They could then be mounted to a fixed position and measure the magnetic field a fixed locations on the coil. While this would be relatively simple, it is very useful to be able to measure the coil field along the beamline direction. This allows for the calculation of integrated quantities along the length such as the integrated harmonics, and effective length. For this reason the decision was to use a modular room temperature bore which could be mounted onto the central testing flange and allow for measurements of the field along the central axis of the coil using room temperature measurement tools.

The warm bore was designed to accommodate for a magnetic field mapper. The carriage of the rail is equipped with a circular holder to accommodate multiple hall probes such that the radial magnetic field can be measured as a function of angle. This allows for a more detailed mapping.

In addition diagnosing can be done without the need to take anything out of the helium which and also allows for in the moment swapping of spare probes if needed. The following sections will outline design and primary components of the testing assembly.

5.2 Central Hanging Flange

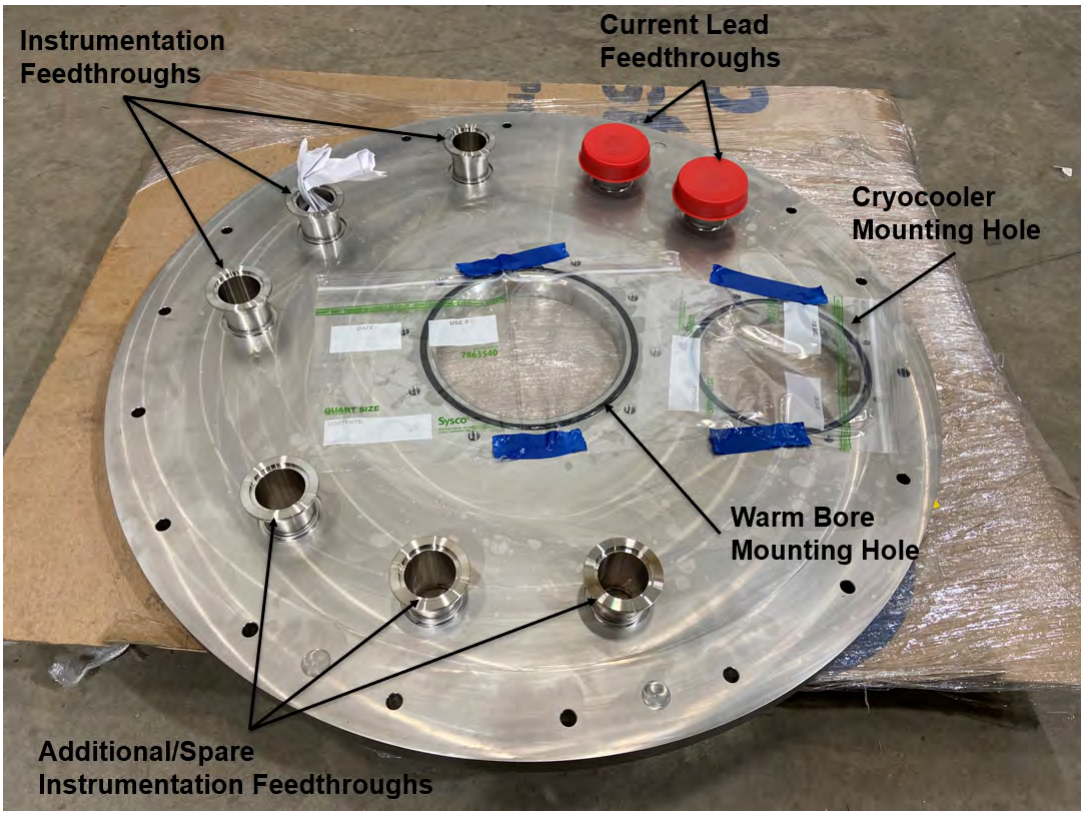

Figure 5.1 Picture of the primary flange which mates the coil hanging assembly to the testing Dewar.

The first primary component designed for this testing was the top flange. The testing setup consists of a central top flange which serves as the mating component to the test Dewar and will support all of the hanging assembly and connections for all necessary instrumentation. The top flange can be seen in Fig. 5.1. It was designed such that 6 primary KF ports can be used for instrumentation feedthroughs, 2 Conflat ports are used for connecting the current lead feedthroughs, a hole with a bolt pattern and o-ring for mounting the cryocooler, and a hole with a bolt pattern for mounting the warm bore. Once machined a test fitting was done to ensure that the flange mates to the testing Dewar and other external components correctly.

Figure 5.2 Test fitting of the top flange to the testing Dewar. Flange was mated to the Dewar and then pumped down to vacuum level and leak checked.

(a) (b)

Figure 5.3 a) Cryocooler test fitted to the testing top flagne while mounted in the Dewar. b) View of the cryocooler cold head positions while mated to the top flange.

The test fitting of the flange to the testing Dewar, two stage cryocooler, and modular warm bore can be seen in Fig. 5.2, Fig. 5.3, and Fig. 5.4 respectively. The cryocooler model used is a Crycomech PT425 two stage pulse tube cryocooler. The cooling capacity and performance of the cryocooler will be discussed in more detail in the following sections. Additionally, the warm bore was test fitted as well to the top flange as intended and was within specification for the magnetic

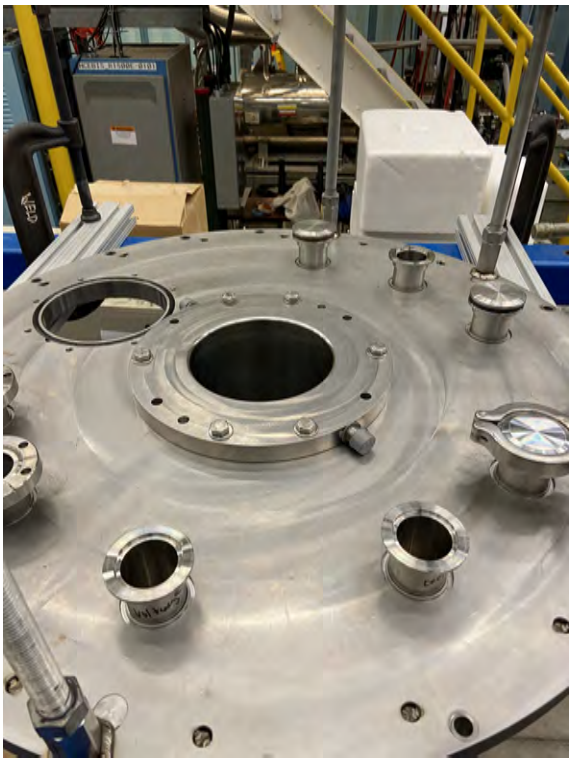

Figure 5.4 Picture of the test mating of the modular warm bore to the top flange of the testing assembly.

field mapping, further detail of the warm bore is discussed in the mapping section of this chapter.

The internal component of the testing assembly consists of several other components. The first stage thermal anchor, which is a circular copper plate thermally anchored to the first stage of the cryocooler. The plate is mechanically supported by a series of Garolite (G10) threaded rods connected to the top flange. The top flange has a circular array of 5 hex coupling nuts on it's bottom surface for the purpose of supporting the first thermal anchor plates weight by the G10 rods. G10 is chosen as the supporting material as we want to minimize the heat leak from the room temperature to the first thermal anchor. G10 has a very low thermal conductivity, approximately 0.3 W/mK, while still providing sufficient mechanical strength with a tensile strength max of 40,000 psi, to support the weight of the testing assembly. The second stage thermal anchor, in a similar fashion, is a circular copper plate supported by G10 thread rods connected from the first stage thermal anchor plate to the second stage thermal anchor plate, G10 is again used for the same reasons. From the second stage plate an array of 3 stainless steel thread rods are connected to a G10 plate which

supports the coil from the bottom and connected this G10 plate to the second stage thermal anchor. The threaded rods are used to secure the weight of the coil and fix its position. An array of 3 screws are used to connect the coil flange to the second stage plate and a set of spacers are used in order to fix the distance between the second stage plate and the top of the coil. The stainless steel threaded rods are tightened until the coil is fastened against the spacers securely. The following sections will outline the remaining components necessary for testing and how they are designed and integrated into the assembly.

5.3 Current Lead Design

As conduction cooling must rely on cooling channels, good thermal contacts, and cryocooler capacity it is important to minimize the heat leak into the system. As current leads can be a dominate contributor of heat, it is important to optimize their design based on the intended operating current and thermal intercept temperature to minimize the heating power they contribute into the system. As a conduction cooling system cannot rely on vapor cooling, the first stage of the cryocooler is used a thermal intercept for the current leads. As our application requires 450 A DC operation of a superconducting coil having a secondary set of current leads made of high temperature superconductor (HTS) which go from the first thermal intercept to the second thermal intercept and connect to the coil leads was considered an optimal setup, as copper leads connected to the 4 K connection would be difficult to implement without the assistance of vapor [39], [40].

5.3.1 Copper Leads

As normal conducting leads are required on the room temperature connection to the power supply, they must be designed such that they are capable of handling the current intended for the magnet, while also minimizing the heat load it delivers to the first thermal intercept. As the thermal intercept temperature is based on cryocooler capacity a lower heat load to first stage helps to improve operating temperature margin to the second stage. Minimizing the heat load of normal conducting leads based on operating current and thermal intercept temperature is a very well studied and understood topic [21], [41], [42].

When vapor heat transfer is not present, the heat transfer equation of a current lead takes the

form of the second order homogeneous differential equation, seen in Eq. (5.6), based on the Joule heating and thermal conduction through the lead. The solution to the differential equation can be used minimize the heat leak by finding the ideal ratio of the cross sectional area to the length. The minimum is a function of the operating current, cold and hot end temperatures, thermal conductivity, and electrical resistivity of the material.

$$Q_{out} = Q_{in} + Q_{gen} \tag{5.1}$$

$$Ak\frac{dT}{dz}\Big|_z = Ak\frac{dT}{dz}\Big|_{z+\Delta z} + \frac{\rho I^2}{A}\Delta z \tag{5.2}$$

$$0 = \left[Ak\frac{dT}{dz}\Big|_{z+\Delta z} - Ak\frac{dT}{dz}\Big|_z\right] + \frac{\rho I^2}{A}\Delta z \tag{5.3}$$

$$0 = \lim_{\Delta z \to 0}\frac{1}{\Delta z}\left[Ak\frac{dT}{dz}\Big|_{z+\Delta z} - Ak\frac{dT}{dz}\Big|_z\right] + \frac{\rho I^2}{A} \tag{5.4}$$

$$0 = \frac{d}{dz}Ak\frac{dT}{dz} + \frac{\rho I^2}{A} \tag{5.5}$$

$$0 = Ak\frac{d^2T}{dz^2} + \frac{\rho I^2}{A} \tag{5.6}$$

Where Q_{in} is the heat flux into the lead, Q_{out} is the heat flux out of the lead, Q_{gen} is the heat flux generated by the current flow in the lead, I is the current flowing through the lead, k is the thermal conductivity of the lead material, ρ is the electrical resistivity of the lead material, A is the cross sectional area normal to the current flow, z is the direction of current flow and heat transfer, and T is temperature. In actuality the thermal conductivity and electrical resistivity are dependent on the temperature of the materials, but for practical purposes it is appropriate to take an average of these values over the temperatures between the hot and cold end. The second order differential can then be expressed as Eq. 5.7, where $\tilde{k}$ and $\tilde{\rho}$ are the average values of thermal conductivity and electrical resistivity over the hot and cold temperature.

$$0 = A\tilde{k}\frac{d^2T}{dz^2} + \frac{\tilde{\rho} I^2}{A} \tag{5.7}$$

A change of variables can be made and then integration can be done over the heat flux and temperature to find the solution to the differential equation.

$$\int_{Q_c}^{Q_h} Q dQ = \int_{T_c}^{T_h} -I^2 \tilde{k} \tilde{\rho} dT \tag{5.8}$$

$$Q_c^2 = Q_H^2 + 2I^2 \int_{T_c}^{T_h} k \rho dT \tag{5.9}$$

It can be seen from Eq.5.9 that Q_c is minimizes when $Q_h = 0$. From this an expression for the minimum heat leak to the cold end can be expressed as Eq. 5.11 which can be used to estimate the minimum heat leak when the ideal geometry condition is met [41], [42].

$$Q_{min} = I\sqrt{2\int_{T_c}^{T_h} \tilde{k} \tilde{\rho} dT} \tag{5.10}$$

$$Q_{min} = I\sqrt{2\tilde{k}\tilde{\rho}(T_h - T_c)} \tag{5.11}$$

Where the boundary conditions of $T(z = 0) = T_c$ and $T(z = L) = T_h$ are applied for integration. Using these boundary conditions, Eq.5.7 can be integrated twice with respect to z in order to find an analytical expression for temperature as a function of z.

$$T(z) = -\frac{\tilde{\rho} I^2}{2A^2 \tilde{k}} z^2 + \left[\frac{(T_h - T_c)}{L} + \frac{\tilde{\rho} I^2 L}{2A^2 \tilde{k}}\right] z + T_c \tag{5.12}$$

Knowing that the heat to the cold side is minimized when $Q_h = 0$ and $Q_h = A\tilde{k}\frac{dT}{dz}\Big|_{z=0}$. Eq.5.12 can be differentiated with respect to z and evaluated at $z = 0$ to solve for an expression for $Q_h = 0$.

$$\frac{L}{A} = \frac{1}{I}\sqrt{\frac{2\tilde{k}(T_h - T_c)}{\tilde{\rho}}} \tag{5.13}$$

Solving $Q_h = 0$ then gives the optimum ratio of length to cross sectional are for a current lead seen in Eq.5.13. Based on the materials properties of our chosen copper we used this to optimize the geometry of the current leads and decided on a suitable design for the copper current leads which is summarized in Table 5.1.

Table 5.1 Copper Current Lead Design Parameters

Parameters	Unit	Chosen
Length	mm	250
Area	mm^2	25.8
Material	NA	Cu 101
Warm End Temp	K	300
Cold End Temp	K	60
Heat Leak @ 500 A	W	20

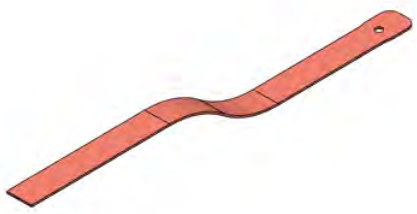

Figure 5.5 Model of copper current lead design. Copper lead is designed with a length of 250 mm and cross sectional area of 25.8 m^2.

5.3.2 HTS Leads

The HTS lead assembly consists of two copper terminals which are used for mounting the lead mechanically and making electrical connections to the copper leads and a G10 shell to provide mechanical strength and protect the conductor. The two copper terminals are electrically connected via high temperature superconducting tape. The HTS material used for our leads was a Yttrium based Rare Earth Barium Copper Oxide (ReBCO) tape, which was rated at a critical current of 215A. The details of the ReBCO tape can be seen in Table 5.2. By using 4 tapes in parallel we made an HTS lead intended for 500 A use with a 58% operating margin at 77 Kelvin. The tapes are soldered to the copper terminal via a standard 63% Lead 37% Tin (63Pb37Sn) electrical solder. The copper terminal is mounted then to the G10 shell which composes the mechanical structure of the lead. The copper terminals are connected to the bottom piece of the G10 shell by a dowel pin and then a top piece is placed onto the shell and the G10 shell is wrapped with fiberglass cloth and then painted with Stycast epoxy in order to seal the shell closed. As the HTS leads are in a low field space, less than 50 Gauss, the impact of external field on critical current capacity is very small, less than 5 ampere. We estimate the heat load of our HTS lead design to be 135 mW per lead delivered to the 4 K thermal intercept [43]–[47].

Table 5.2 ReBCO Parameters

Parameters	Unit	Chosen
Conductor Type	NA	ReBCO
Width	mm	6
Thickness	mm	0.1
Cu Stabilizer Thickness	μm	40
Silver Thickness	μm	3.6
Hastelloy Thickness	μm	50
Critical Current @ 0 T	A	215

Before fabrication of the leads it is necessary to verify the current carrying capacity of the ReBCO. To do this we cut a strip of ReBCO to the intended length of the design and solder it to a copper terminal which can be seen in Fig. 5.7. Voltage taps are then soldered onto the tape at a measured distance of 18.67 cm. As the quench voltage of ReBCO is 1 μV/cm, we expect to measure

(a) (b)

Figure 5.6 a) ReBCO tape soldered to copper terminals for power supply connection and mounted to G10 plate. b) ReBCO testing with power leads connected to terminals and voltage taps connected to ReBCO tape sample.

a quench voltage of about $18\mu V$ from a single tape [48]. The tape is then tested by connecting the power cables to the testing jig, seen in Fig. 5.6.

We submerge the testing jig in liquid nitrogen to bring the tape below it's critical temperature. Once nitrogen boil off is seen to settle the temperature of the copper terminals and tape is considered saturated and the power supply is turned on and prepared to deliver current. Current was increased in the tape until a quench was detected based on voltage reading. The quench voltage of $18\mu V$ was detected at a current of 250 A in our ReBCO sample. Nitrogen testing can be seen in Fig. 5.7a and the plot of the current versus the voltage during testing can be seen in Fig. 5.7b.

Once the critical current of the tape has been verified, the HTS current lead assembly process is begun. The copper terminals are placed in an assembly jig such that the ReBCO tapes can be cut to the proper length for the leads and slotted into the copper terminals. Once slotted into the copper terminals the tapes are soldered, and the temperature is monitored via a thermocouple to assure that the ReBCO is kept below 220C and for less than 30 minutes as a general procedure for current lead fabrication. This helps to assure that the ReBCO does not undergo thermal degradation which will lower the critical current of the tape. These soldered connections are made with a standard 63Pb37Sn electrical solder. The overlap length between the tape and the copper for the soldering joint is 25mm, as the joint length is 5 times the tape width as a standard sizing for HTS soldered

(a)

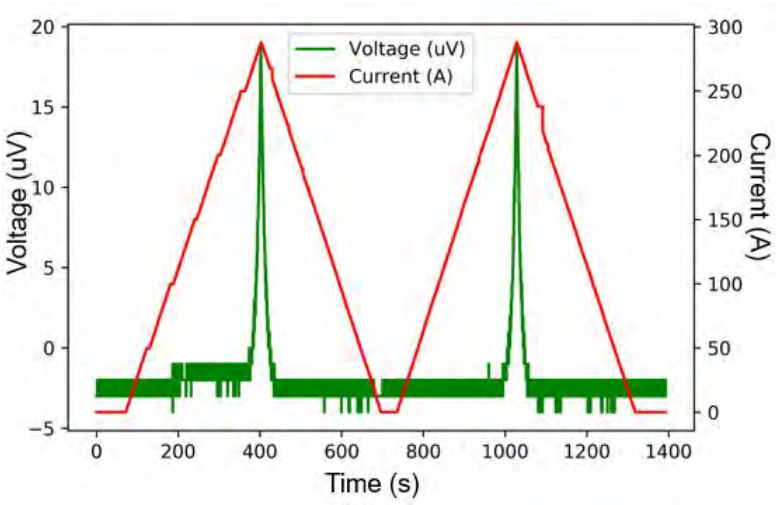

(b)

Figure 5.7 a) ReBCO testing jig submerged in nitrogen to test the critical current carrying capacity of the ReBCO tape. b) Voltage and current measurement of ReBCO tape in liquid nitrogen. The exponential growth of the voltage is seen at 250 A, where voltage is measured by a Keithley DMM6500 multimeter.

connections [49]

Once soldered to the copper terminals a G10 shell is fixed to the structure via two dowel pins, seen in Fig. 5.8. There is then a top piece which is pressed to the top of the shell and fastened via a wrapping of fiberglass cloth. The outer wrap of fiberglass cloth is then painted with epoxy to seal the structure together. Clearance is left for holes in the G10 shell so that any trapped air is allowed to escape in a vacuum environment and allows for the flow of liquid nitrogen to have direct contact with the tape for liquid testing. The assembly process for wrapping and potting can be seen in Fig. 5.9.

Once assembled the current leads are tested in liquid nitrogen to verify their current carrying capacity before use in the testing setup. Once current lead fabrication is completed, as seen in Fig. 5.10, the current leads are fastened to the same testing jig as ReBCO tape and tested in the same manor. Once fastened to the testing jig and submerged in liquid nitrogen the current is ramped up in stages up to the target max operating current of 450 A. They are sustained at max operating current for 10 minutes to test stability at max operating current.

The lead testing showed that the voltage increases linearly with current, seen in Fig. 5.11b.

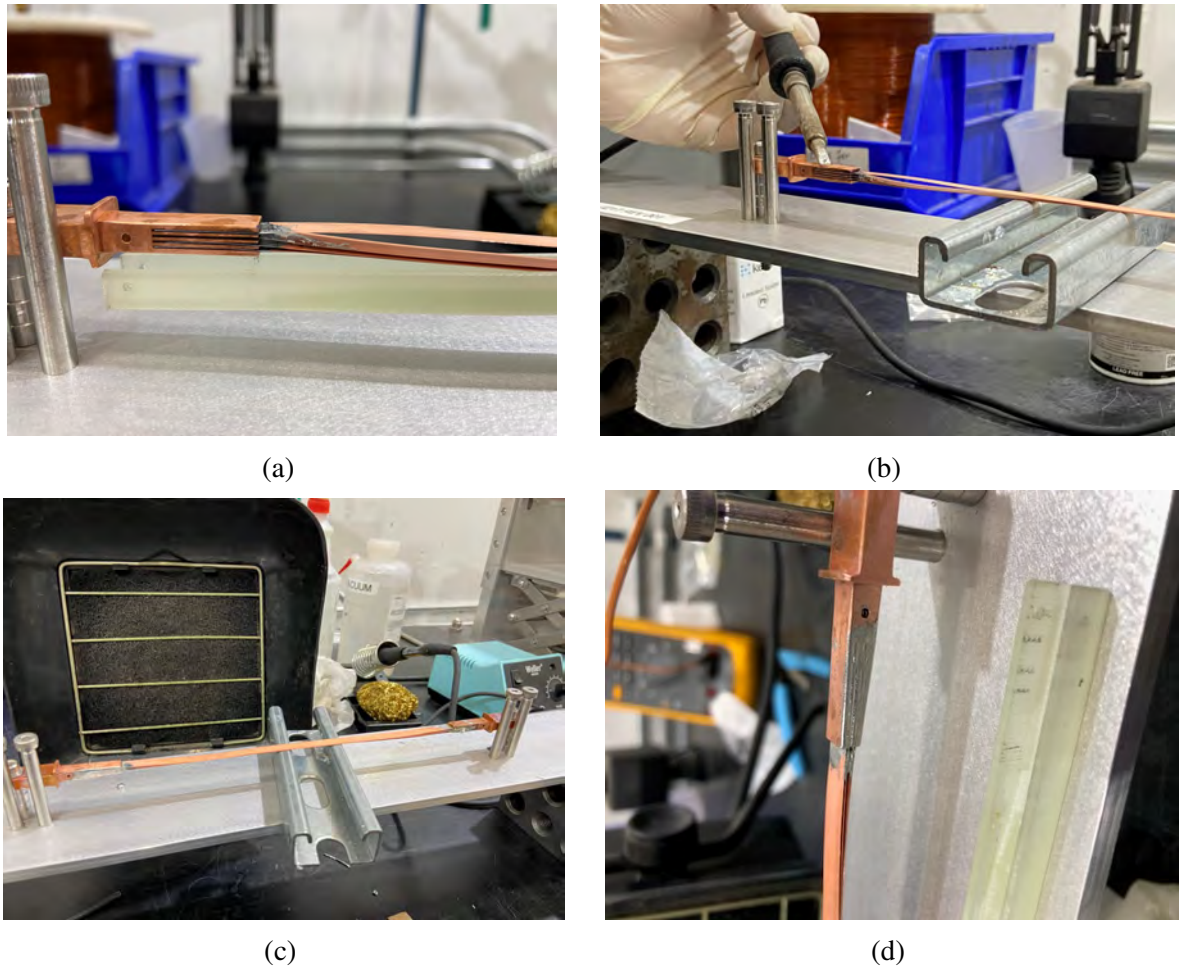

(a) (b)

(c) (d)

Figure 5.8 a) ReBCO tape slotted into copper terminal joint where it filled be soldered to copper. b) Active heating of the soldered joint for lead assembly. c) Picture of full length lead assembly after soldering of ReBCO to copper terminals. d) Close up of soldered joint of HTS lead.

This can be expected as the voltage taps are soldered to the copper terminals of the lead therefore a restive response is expected from the voltage reading, voltage tap locations can be seen in Fig. 5.11. During testing when held at constant current no increase in voltage beyond the $18\mu V$ ReBCO tape quench voltage was observed and stable operation at 450 A was achieved in liquid nitrogen testing. With the conclusion of 450 A HTS lead testing the leads are ready to be installed into the testing Dewar. Their performance is then observed in a conduction cooling scheme using the cryocooler in conjunction with the copper leads.

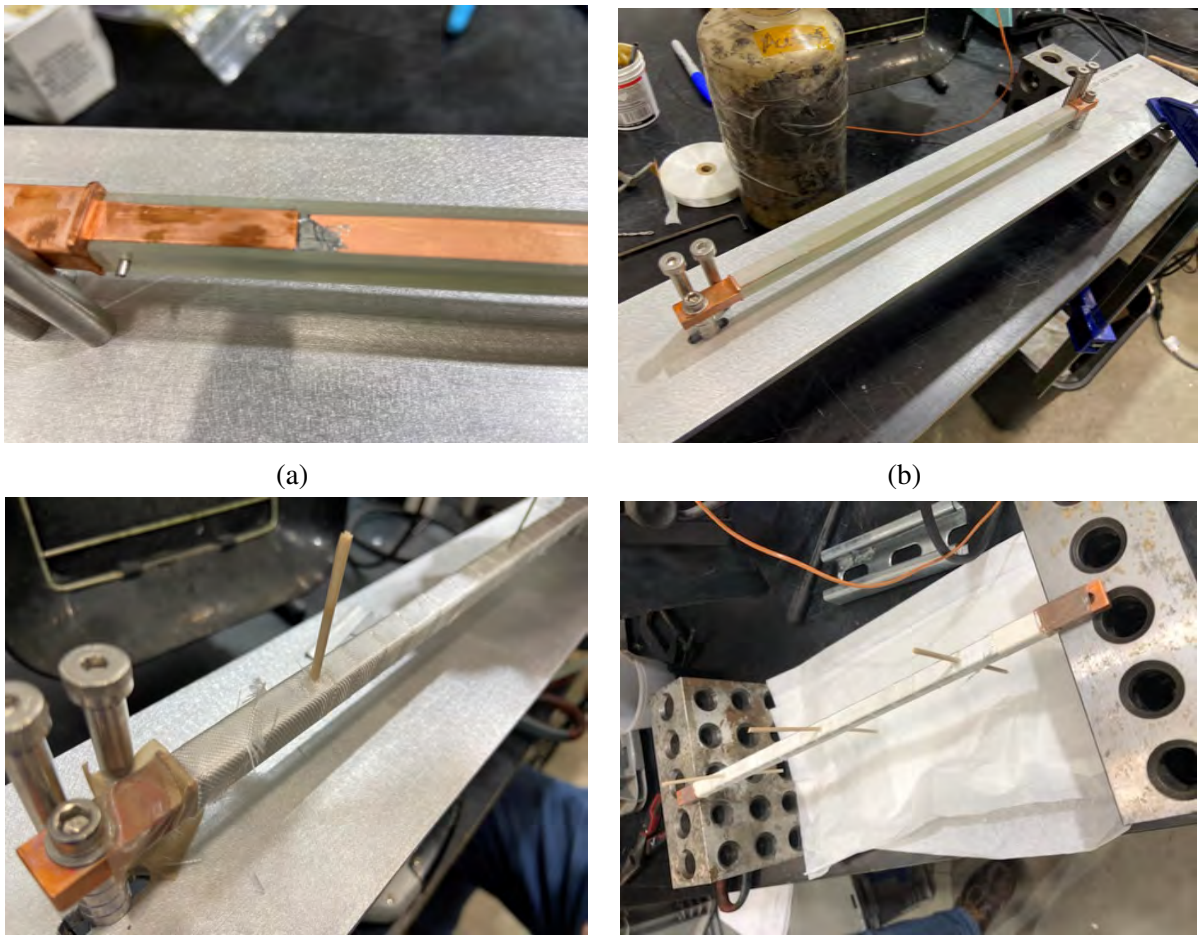

(a) (b)

(c) (d)

Figure 5.9 a) Picture of G10 shell being fixed to copper terminals via dowel pin. b) Picture of G10 full assembly for protection of ReBCO tape in the HTS lead. c) Close up of fiberglass wrapped lead where the wooden sticks for keeping hole clearance. d) Picture of fully fiberglass wrapped lead.

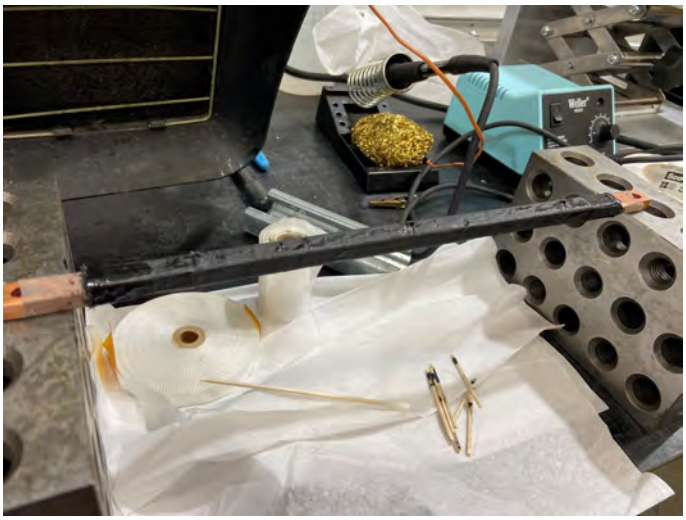

Figure 5.10 HTS lead which has had fiberglass cloth wrapping painted with epoxy in order to seal the lead, after epoxy curing the lead fabrication is complete.

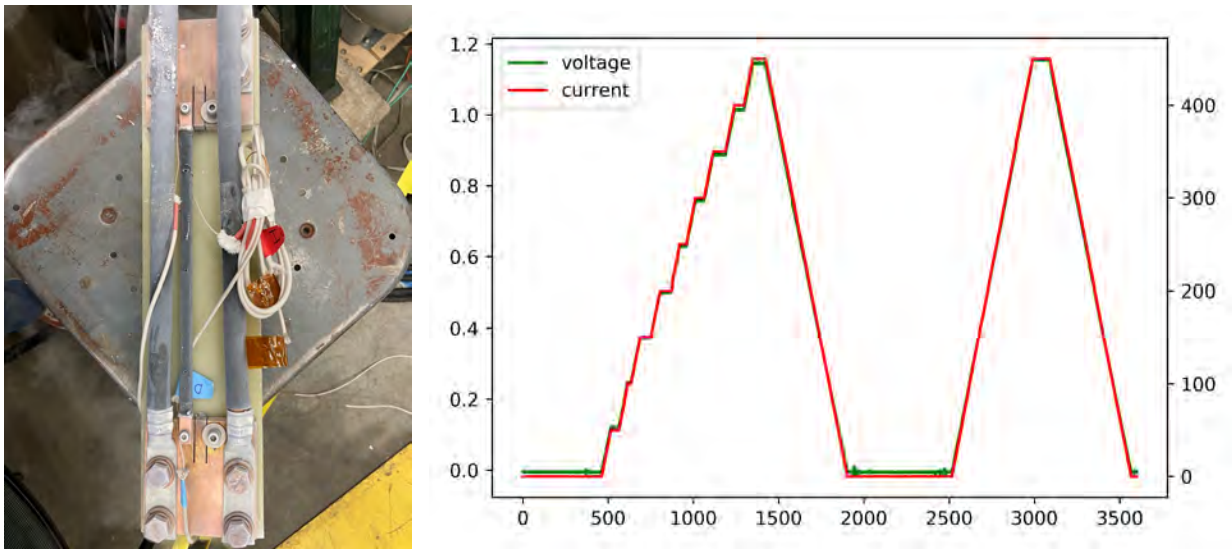

(a) (b)

Figure 5.11 a) Picture of HTS lead after being pulled out of nitrogen testing Dewar. b) Plot of the voltage and current of the HTS lead versus time.

5.3.3 Current Lead Conduction Cooling Test

As the current leads are designed to be operable in a conduction cooling scheme they are tested at 450 A in a conduction cooling setup to analyze their performance. The testing scheme consists of the two stage cryocooler, where the first stage is used to achieve the thermal intercept temperature for the HTS leads, approximately 60 K, and the second stage is used to achieve 4 K temperature at the bottom of the HTS leads where they will connect to the superconducting coil. For the purposes of testing, the HTS leads are connected at the bottom by a NbTi sample connected to copper stabilizer in order to form a closed current loop. This is done to monitor the NbTi sample and monitor if it quenches.

The copper leads are soldered to a vacuum current lead feedthrough which is rated up to 700 A. The bottom of the copper leads are then fastened together with the HTS leads to the first thermal intercept plate. In order to electrically insulate the copper plate to prevent electrical short in the case of HTS quench a sapphire washer is used between the current lead connection and copper plate thermal anchor along with an insulating sapphire bushing for the fastening screw. This allows for sufficient electrical insulation to prevent an electrical short, but has higher thermal conduction than other insulating materials such as kapton or G10. The copper plates which are the temperate anchors for the current leads are fastened directly to the cryocooler by fastening screws to the cold heads and using indium foil as a thermal contact medium between the two surfaces.

A series of temperature sensors are used to observe temperature gradient and cryocooler cold head temperatures. The temperature sensors used were Cernox™1010-CU type temperature sensors, 6 were placed at various points of interest around the testing setup. There were also voltage taps soldered to two spots on each lead such that the voltage across each lead could be measured during testing. While temperature sensors could not be placed directly onto the current leads due to risking electrical damage, they are placed right before the sapphire washer interface to observe temperature change during operation. The entire testing scheme can be seen in Fig. 5.12.

Once internal connections are completed a copper sheet is rolled around the mechanical assembly and thermally anchored to the first stage of the cryocooler to act as a thermal shield. Once

(a) (b)

Figure 5.12 a) Testing setup for conduction cool current lead scheme using two stage PT425 Cryomech cryocooler. b) View of interface of HTS lead to 4 K thermal intecept.

mounted it is then wrapped with 20 layers of MLI. These steps can be seen in Fig. 5.13. It is then transferred to a testing Dewar and instrumentation connections are checked and the internal pressure of the Dewar is pumped down to vacuum level below 50 mTorr. Power supply connections are made so that current can be provided to the leads as soon as temperature saturation has been reached from cryocooler cool down. The testing setup is then left for approximately 17 hours for cooldown, this was sufficient time to reach temperature equilibrium. The leads are then energized up to 450 A and held at that current to check stability. The equilibrium temperatures of the leads at zero current and max current can be seen in Table5.3.

Finding the optimal thermal contact for the leads in order to get enough heat transfer for 450 A operation at 4 K was challenging. It was found that a combination of single crystal sapphire washers with thermal grease connected to the copper leads and indium foil used at contact interface between the copper leads and HTS leads achieved an appropriate amount of thermal conductance for 450 A operation of conduction cooled leads. Based on these challenges geometry changes were

(a) (b)

Figure 5.13 a) Picture of thermal shield for current lead conduction cooling test. b) MLI layering wrapped around thermal shield as final preparation for testing.

Table 5.3 Lead Conduction Cooling Testing Temperatures

Location	Temperature: 0 A	Temperature: 450 A
1st Stage Cold Head	29.3 K	31.279 K
2nd Stage Cold Head	3.55 K	3.68 K
1st Stage Lead 1 Near Interface	30.58 K	33.56 K
1st Stage Lead 2 Near Interface	30.91 K	34.30 K
2nd Stage HTS 1 Near Interface	3.87 K	4.12 K
2nd Stage HTS 2 Near Interface	3.82 K	4.07 K

made to the HTS lead design and used for a second version of HTS, which were fabricated for coil testing. Primarily the copper joints contact area for interfacing with the thermal intercept was increased by a factor of 3 to 341 mm^2.

The new HTS lead design can be seen in Fig. 5.14. These leads are then liquid nitrogen tested in the same manner as the first version of the leads in order to verify that they can carry 450 A stably at 77 K. The lead voltage at 450 A are lower by approximately 20-50% than the voltages of the HTS leads tested previously, seen in in Table.5.4. We attribute this to a better scheme for

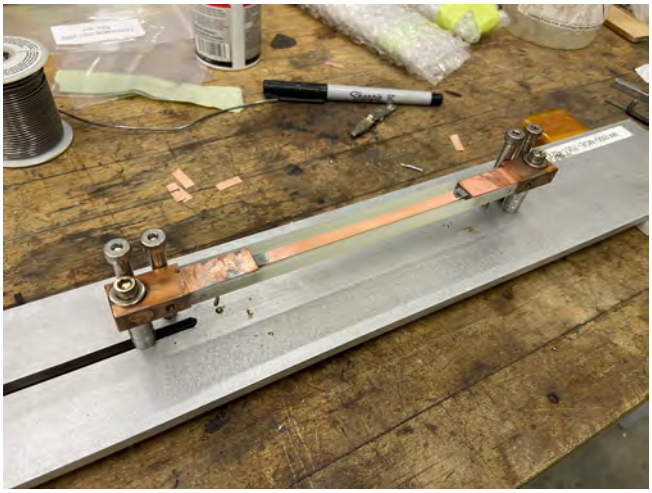

(a)

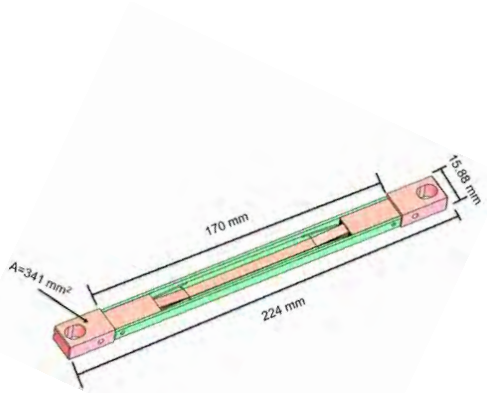

(b)

Figure 5.14 a) Picture of HTS lead assembly in progresses after soldering connections have been made. b) Picture of HTS lead model with dimensioned indicated.

Table 5.4 HTS Lead Version 2 Nitrogen Voltage Measurements

HTS Lead	Voltage	Current
Lead 1	0.57 mV	450 A
Lead 2	0.83 mV	450 A
Lead 3	0.86 mV	450 A

mechanical contact in the testing jig and better voltage tap contact with a more stable soldered connection. Similar to the first set of fabricated leads the voltage was constant at constant current and no voltage growth indicating tape quench was observed. Once 450 A performance was verified the new leads were then integrated into coil testing assembly. The assembly instrumentation and leads connections are discussed in the following sections.

5.4 Testing and Preparation

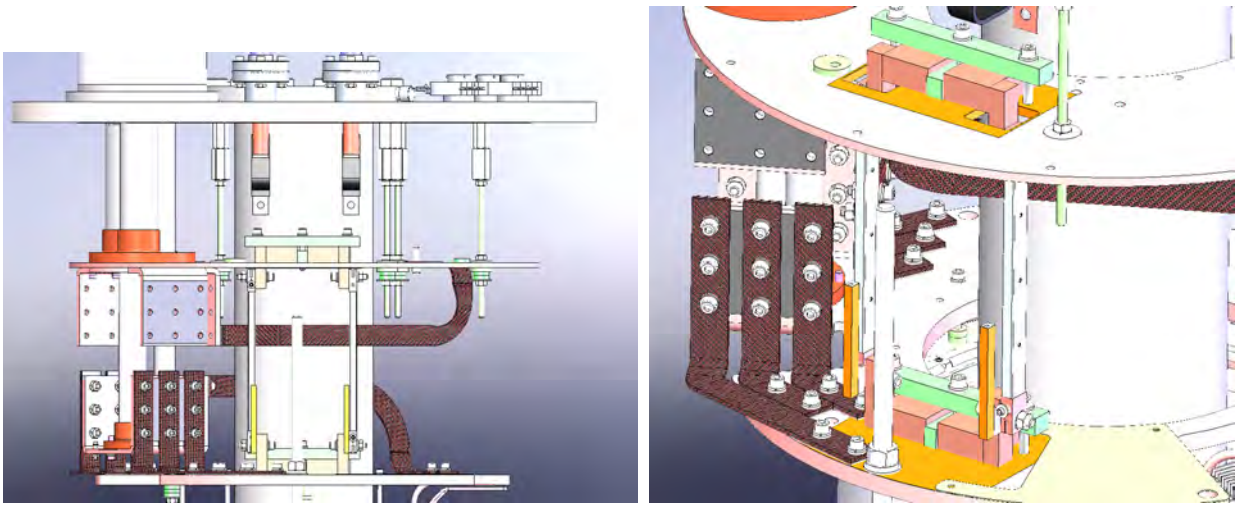

(a) (b)

Figure 5.15 a) Front view of final testing assembly model. b) Isometric view of the finalized HTS lead assembly for coil testing.

Due to difficulty in achieving a thermal contact interface for the leads that resulted in enough heat transfer to cool the HTS leads down to 4 K at the location that they would interface with the coil leads. A redesign was done in order to simplify and eliminate certain elements in order to simplify the assembly process and improve the cold temperature of the leads at the first and second stage thermal intercept. Instead of using 1/8 inch thick alumina washers along with insulating bushing and thermal straps, we chose to use an "L" style bracket piece which would allow the leads to mount directly to the "L" bracket copper piece. This copper piece would then be mounted directly to the copper plate for each thermal anchor and electrically via a 0.01 inch thick kapton sheet. The model of the new lead connection scheme used for testing can be seen in Fig. 5.15.

While kapton is a less than ideal thermal conductor , 0.8 W/mK, the kapton was thin enough used in conjunction with a large enough cooling area that the lead received a sufficient amount of cooling. The new scheme was assembled, seen in Fig. 5.16, and the temperature was saturated at 47 K at the leads on the first stage thermal anchor. While the leads saturated at 4 K on the second stage thermal anchor. This meant that the leads could be operated in a conduction cooling scheme after the design changes. As the first energization test was to be a liquid Helium test in order to

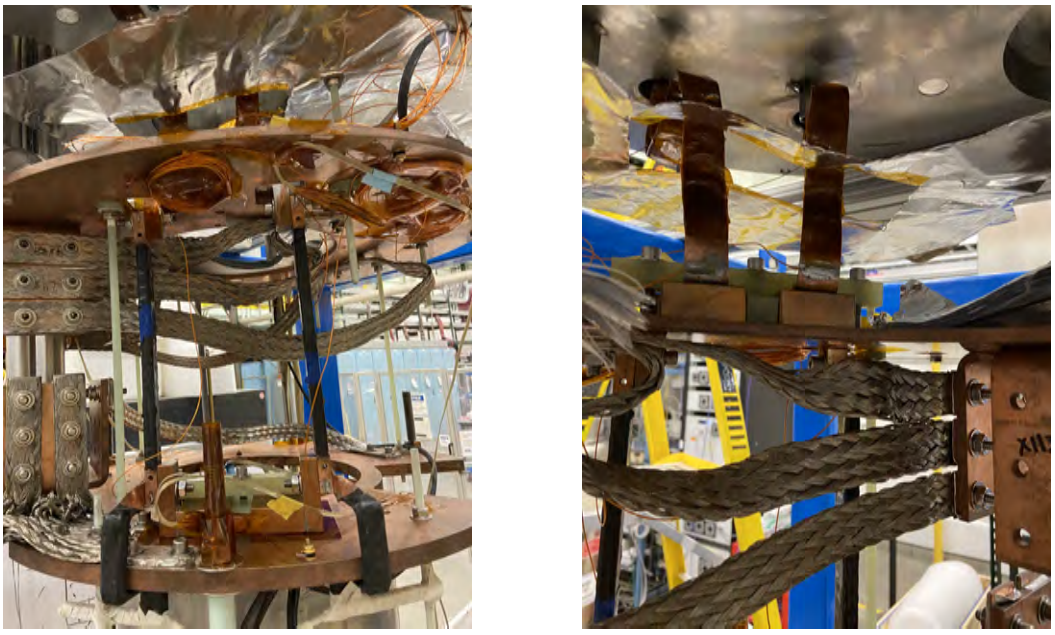

(a) (b)

Figure 5.16 a) Picture of the completed lead assembly including coil lead connections. b) View of the resistive lead connection to the copper mounting piece.

observe the coils training behavior with confidence in the cooling power, the most crucial part was providing enough cooling at the first stage such that the HTS leads could be operated below their critical temperature using cryocooler without relying on helium vapor cooling power.

The coil end which has the lead connection is mounted directly to the second stage copper plate via a set of 3 screws. A set of spacers is used to keep the coil 0.75 inches from the bottom surface of the copper plate. This is done to allow room to route the leads without damaging them. The leads themselves are soldered to a copper junction which has a pocket for soldering them into place and then a bolt hole to connect them directly to the HTS leads. The coils weights is primarily support by a G10 plate which holds it's weight. A G10 plate screws direct to the bottom of the coil using the end flange of the coil. Then 3 stainless steel threaded rods connect the G10 plate to the second stage copper plate and is fastened until the coil is tight against the top spacers. The mounted coil can be seen in Fig. 5.17. Instrumentation summary and non mechanical final preparation are described in the following section.

Figure 5.17 Picture of the full coil testing assembly ready for insertion into testing Dewar for liquid Helium testing.

5.5 Coil First Energization and Training

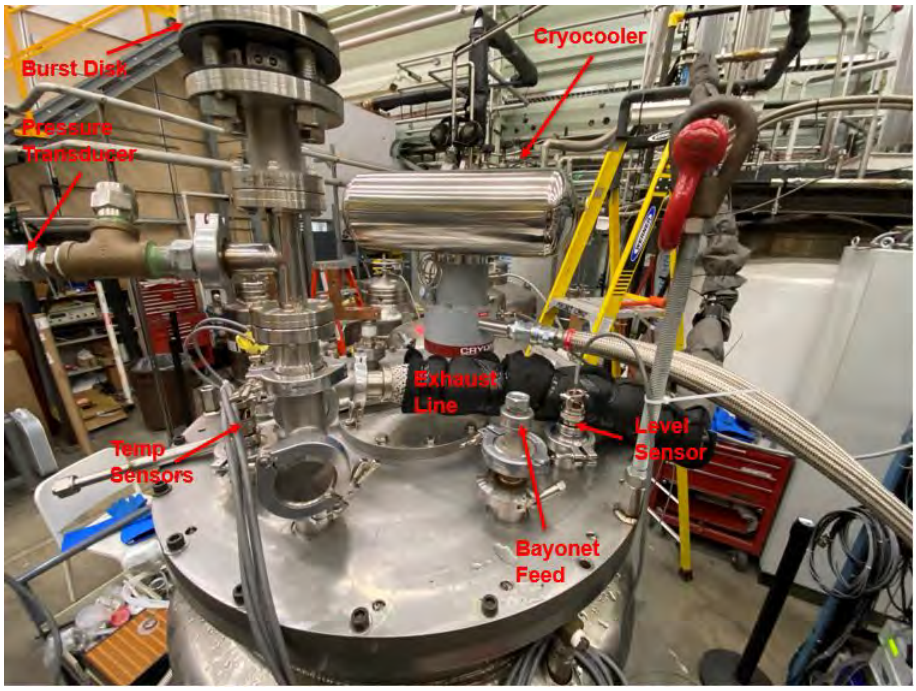

Figure 5.18 Layout of the instrumentation interfaces for the liquid helium testing of the CDQ coil.

This section will describe the first liquid helium testing preparation, procedure, and results. The first 4 K testing of the CDQ single layer prototype was conducted for the purpose of observing both the coil training and operational stability. This test was conducted with liquid helium in conjunction with a cryocooler. While the cryocoolers primary purpose was for future development of a conduction cooling scheme for the coil, the cryocooler can be used during helium testing in a hybrid scheme for multiple benefits. After a pre-cool of liquid nitrogen followed by helium purging of the system the cryocooler can be used to cool the leads and second stage copper plate before helium filling to reduce the amount of liquid used during the initial cool down of the coil. In addition the cryocooler, helps reduce the heat load to the bath and keeps the first stage temperature below 77 K during testing. For these reasons it is worth while to run the cryocooler during helium testing as a hybrid scheme as it offers virtually no draw backs.

The goal of the first liquid helium testing was to bring the coil to it's max current in both polarities and sustain maximum current for a minimum of 20 minutes. This testing would also provide the opportunity to verify the inductance of the coil based on the measured voltage during

current ramp in addition to observing the coil stability. A layout of the testing Dewar flange can be seen in Fig. 5.18, which labels the pertinent connections, feeds, and exhaust for helium handling.

5.5.1 Instrumentation & Assembly

The instrumentation for coil testing consisted of a series of Cernox™temperature sensors to monitor the temperature at various locations of the testing setup, voltage taps to monitor both current lead voltage and coil voltage, a helium level sensor to monitor the helium level and consumption, and a pressure transducer to monitor the helium gas pressure in the testing environment. The temperature sensors were placed at several location along the length of the coil, seen in Fig. 5.19, and additionally at several locations on each thermal intercept plate. The voltage taps allowed for the measurement of the voltage across each individual current lead as well as measuring the voltage across each layer of the coil and the total voltage drop over the coil as well. After wiring and sensor placement, all instrumentation wiring is connected to vacuum feedthroughs and then connections are checked and verified with resistance measurements to each connecting pin.

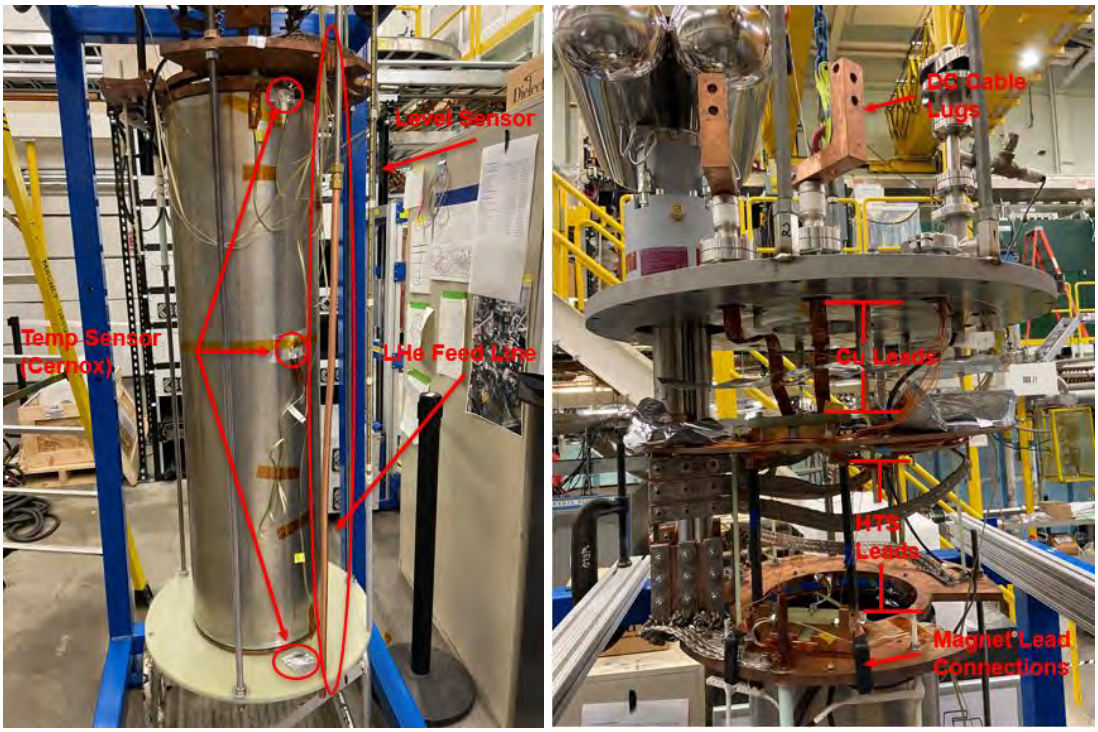

(a) (b)

Figure 5.19 a) Picture of mounted coil with instrumentation connections. b) Labeled connections of the lead assembly.

5.5.2 Nitrogen Pre-cooling

Pre-cooling the coil and testing surroundings is a necessary step in any liquid helium test as it reduces the amount of helium consumed to cool down the coil. The pre-cooling process is as follows: 1) A liquid nitrogen rolling Dewar is used to flush the system with cold nitrogen gas to initiate the pre-cool; 2) Once the temperature is saturated from the cold gas, liquid nitrogen is then filled into the vessel through the fill line; 3) After liquid nitrogen covers the coil package based on temperature sensor reading, the coil resistance is monitored until the resistance drop to 4Ω, which correlates to an internal temperature of 80 K, ; 4) Once the coil pack has been pre-cooled to 80 Kelvin the system is pressurized to push out the remaining liquid nitrogen; 5) The helium space is pumped down to a vacuum level of at least 80 mTorr; 6) The system is then filled with room temperature gas helium up to 1-2 psig in order to clean any residual nitrogen gas or liquid out of the system.

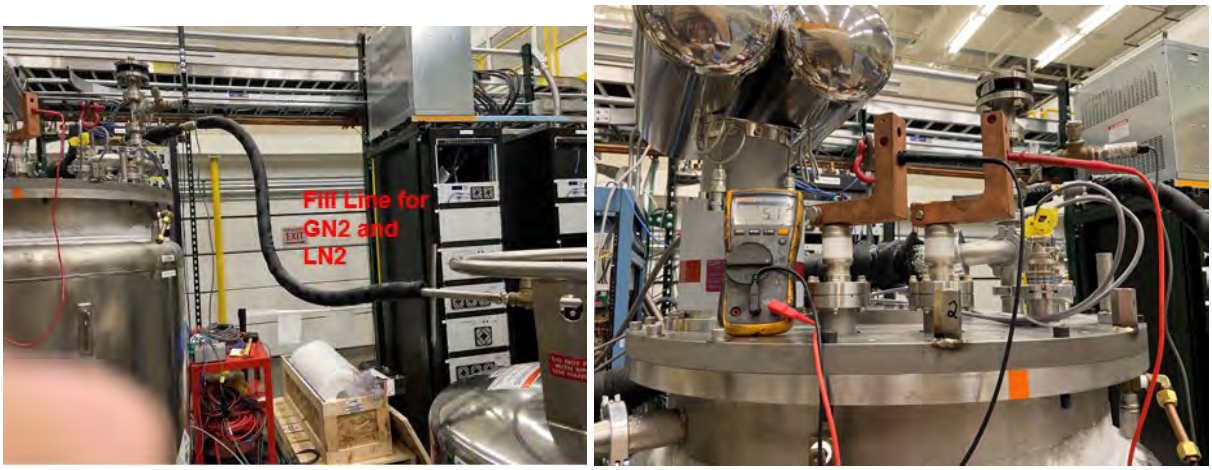

(a) (b)

Figure 5.20 a) Picture of liquid nitrogen filling process for pre-cooling of coil. b) Resistance monitoring of the coil for internal temperature verification.

While the purging process warms the system back above liquid nitrogen temperature, purging the system of nitrogen is a very important step in the preparation for filling with liquid helium. Remaining nitrogen in the system can rapidly solidify as the temperature at which nitrogen turns solid is 65 Kelvin at 1 atm. Solidified nitrogen can cause blockages in the flow of liquid helium and additionally residual nitrogen can also rapidly form a sheet of solid nitrogen on surfaces. This

is very inefficient for helium cooling as the specific heat capacity of solid nitrogen between 60 K-4 K averages 1.2 J/gK, which is almost several orders of magnitude higher than that of most conventional metals and alloys in the same temperature range, for example Aluminum averages about 0.07 J/gK in that same temperature range. Similarly the thermal conductivity of solid nitrogen in that temperate range is about 0.7 W/mK whereas most metals span 10-140 W/mK. This makes cool down and heat transfer to the liquid bath much less than efficient therefore nitrogen needs to be removed from the system before liquid helium is introduced [39].

5.5.3 Helium Cooldown

Before the liquid helium cooling process the amount of the liquid helium necessary for testing is always estimated first. It was calculated that for the initial cool down of the coil pack itself from approximately 100 K to 4 K would consume about 280 L, Filling the liquid level to the required level for testing would require 300 L, and the helium consumed from a quench would be about 14 L. Based on the total heat load of about 3.6 W to the helium bath this results in a boil off rate of about 4.5 L/h. With an estimated testing time of around 6-7 hours, the total helium required is about 630 L for testing requirements [50]. This estimate is used for comparison against the real consumption to see the relative accuracy of the heat load estimates.

The liquid helium filling process is as follows: 1) Liquid helium Dewar is placed exact distance of u-tube transfer line from testing fill line; 2) Pressure in the testing vessel is kept above 2 psig using helium gas; 3) U-tube is connected to liquid helium Dewar side and allowed to purge with gas from liquid Dewar in order to keep line clean; 4) U-tube is then connected into the testing Dewar and connections are sealed and liquid helium flow begins; 5) Liquid flow continues until level sensor reads the intended fill level for testing (86% / 300 L). The filling process can be seen in Fig. 5.21. After filling we monitor the resistance of the coil using a Fluke™multimeter until the resistance reading reaches the meters minimum readable resistance.

From then the helium level is monitored from the level sensor. About 400 L of helium were consumed cooling from the beginning of the filling process to the liquid level reaching the intended location on the level sensor. As 580 L total for cooldown and reaching fill level was a conservative

estimate the 400 L consumption was within expectation for this testing. No abnormalities or leaks appeared during the filling process.

Figure 5.21 Picture of 1000 liter liquid helium Dewar connected to the coil testing Dewar via liquid helium U-tube transfer line.

5.5.4 Energization

Once we confirm that the coils temperature is sufficiently low based on resistance measurement the power cables are then connected to the power lead lugs, seen in Fig. 5.22. After connection the coil is ramped up to 2 A and and monitored for 2 minutes. Once an inductive voltage is seen during ramp and the voltage returns to the 0 A state at constant current the ramping process continues, as this confirms the coil is receiving current properly. The coil is then ramped to 5, 10, 20, 80, 150, 200 A and held for 2 minutes at each current. Then ramped up to 250, 300, 350, 400 A and held for 5 minutes at each stage. The coil is then ramped up to 450 A and held for 20 minutes to monitor the stability. Based on the inductive voltage and ramp rate of 0.5 A/s that's used during testing, using Eq. 5.14 is used to confirm the inductance of the coil. Based on the inductive voltage we calculate

a 51 mH inductance. This is consistent with both the simulated coil inductance and the inductance measurement taken before impregnation. The inductive voltage can be seen to be constant during periods of constant ramp rate, seen in Fig. 5.23.

$$V = L\frac{dI}{dt} \tag{5.14}$$

Figure 5.22 500 A power supply DC cable connection to the leads connection lugs of the coil testing assembly.

We were able to successfully ramp up to the maximum intended operating current of 450 A and sustain operation for 45 minutes with no quench. The current was then increased to 500 A to see if the coil can be operated above it's maximum stably, as operating up to 500 A would allow more beam tuning benefits. The HTS leads are capable of handling 500 A at a 58% operating margin at 77 K, implying that the leads should not be a restricting factor for 500 A operation. HTS leads held a voltage of 0.45 mV at 0 A. We saw a voltage increase of 0.5 mV for each lead at 450 A operation. This is consistent with the testings voltages seen. As the voltage growth from 0 A to 450 A is consistent with the HTS lead testing and the voltage growth was also linear as expected, the HTS leads exhibited no operational issues. The temperatures of the HTS lead warm side was seen to be 68 K at it's hottest and 60 K at it's coldest. This was good as we saw that even when

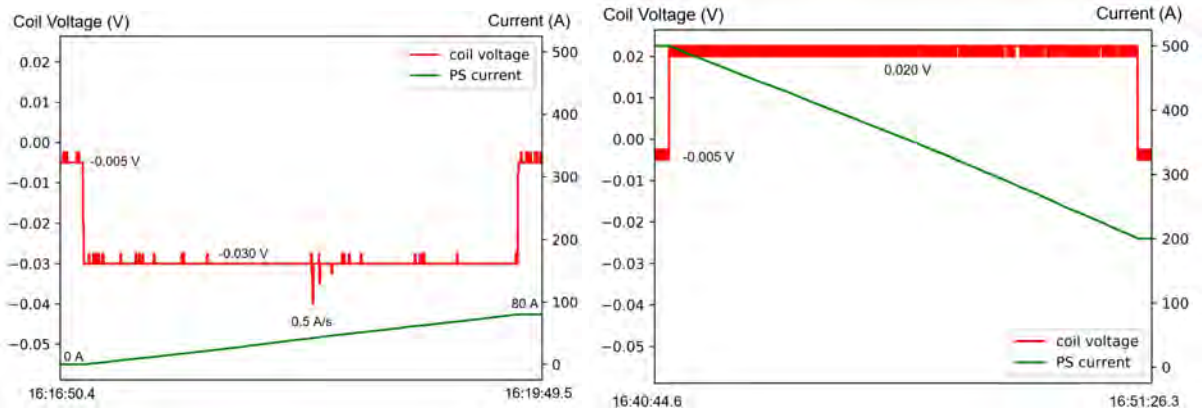

(a) (b)

Figure 5.23 a) Inductive voltage and power supply current versus time plot, while ramping from 0 A to 80 A at 0.5 A/s ramp rate. b) Inductive voltage and power supply current versus time plot while ramping from 500 A to 200 A at 0.5 A/s ramp rate.

the liquid level started to run low and the leads cold end heated up to 5.4 K that the HTS leads still had a temperature margin of 10 K for their operation and confirmed stable operation at 500 A. The sub-scaled prototype was able to operate at 500 A stably for 20 minutes. Once 500 A operation was confirmed to be stable the coil was ramped down to 0 A and then the polarity was switched. The coil was switched to -450 A operation and the inductive voltage was confirmed to be the same as during positive ramp up. The magnitude of the change in voltage during periods of current ramping can be seen to be the same during both positive and negative ramping in Fig. 5.23, about 0.025 V which corresponds to the calculated 51 mH.

To verify the field linearity as a function of excitation current the field at the surface of the testing Dewar was measured using a portable gaussmeter. We expect a linear relationship to field and excitation current as the design is iron free and no magnetic materials are present in testing. The field was measured at a fixed spot and was measured at every 100 A up to 500 A. We found that the field did change linearly with respect to excitation current based on a linear regression fit of the data. The results of these measurements and a plot of the field versus the current can be seen in Fig. 5.24.

In summary, stable operation at the design maximum of 450 A and above maximum at 500 A was observed with no quench occurring during any part of the coil testing. While the total

forces on the single layer quadrupole are lower than the intended full package, this was a promising indication of little or no training being needed for coils wound and impregnated in this way. After the verification of stable operation at max current, field linearity, and coil inductance liquid helium testing was concluded. The following sections discuss the magnetic field mapper design and the magnetic field mapping results from a second liquid helium test.

(a)

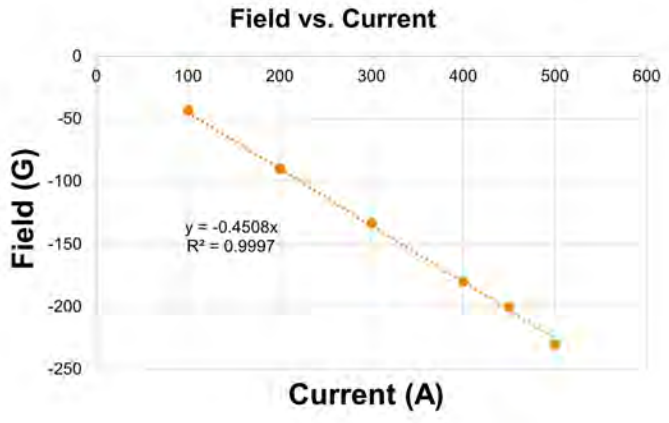

(b)

Figure 5.24 a) Field measurement taken at every 100 A. b) Plot of current versus measured field.

5.6 Mapper & Mapping Setup

As discussed in the previous sections, the magnetic field within the area of the planned warm bore would be measured in order to verify the field gradient and uniformity of the single layer. We constructed a mapping system and mechanical assembly which would allow for a room temperature mapper to be used to scan the field. This was done via a double walled warm bore for operation in a liquid helium testing scheme. A diagram of the warm bore can be seen in Fig. 5.25.

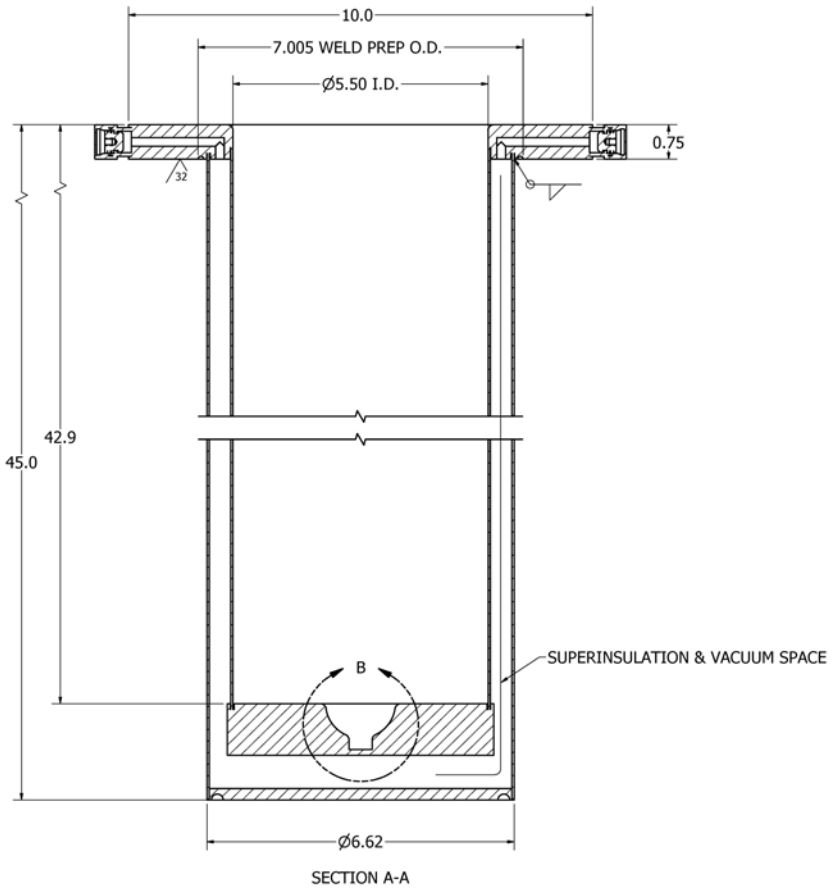

Figure 5.25 Profile of view of the warm bore drawing used for mapping.

The mapper consist of a lead screw driven rail system. On the carriage of the rail is a circular flange which holds a series of Hall sensors. The hall sensors are mounted at a radius of 63.5 mm and an array of 6 sensors is used. The 6 sensors can each be moved such that measurements can be made at every 15 degrees along 63.5 mm radius circle. The angular adjustment of 15 degrees is

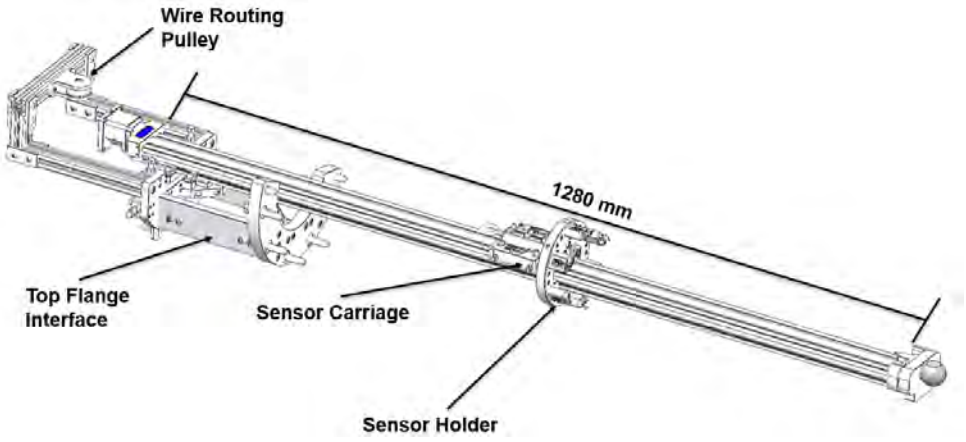

Figure 5.26 Mechanical model of the magnetic field mapping system used to scan the magnetic field of the CDQ coil.

chosen so that we have the minimum required angular resolution in order to measure up to the $n = 6$ harmonic component of the field. The hall probes are oriented so that they will measure the radial magnetic field component of the quadrupole as a function of angle. This measurement can also be taken at steps along the central axis of the coil up to the middle of the coil in order to compute the effective length and integrated strength of the coil. Due to the size constrictions of the testing Dewar we execute a mapping of half of the coil and take the coil to be symmetric about it's mid plane. The motor controls for the movement of the rail carriage and the data acquisition for the hall probes is controlled via LabView and a National Instrument cDAQ. On the sensor flange 5 HE244 Hall probes are used along with 1 SENIS probe. The HE244 probes are operated at a nominal current of 2 mA and their output voltage scales linearly with the applied field, they are advertised to keep linearity to ±0.2% when kept at steady temperature, constant current, and in the range of 0 T to 2 T applied field [51]. A portable current supply was used to provide the 2 mA current to each Hall probe. The other probe used is a SENIS type C 3 axis magnetic field probe used with a SENIS 3MH6-E Digital Teslameter which comes calibrated and allows for high accuracy magnetic field measurements, 100 ppm in ±2 T range [52], [53].

The model of the mapping system can be seen in Fig. 5.26. Which depicts the rail system and mechanical assembly required for mounting to the testing Dewar and warm bore. The circular flange and the sensor holder models can be seen in more detail in Fig. 5.27. We mount a hall sensor

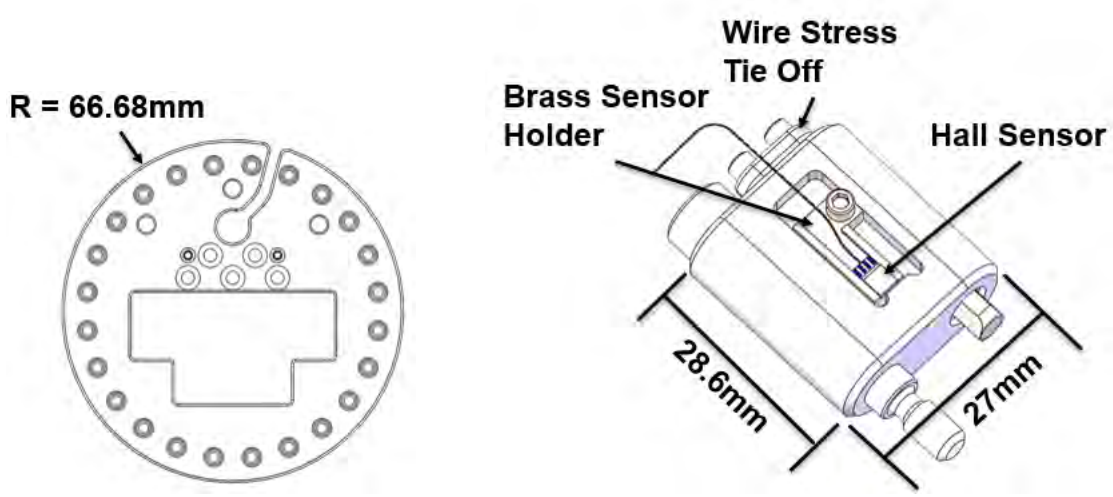

(a) (b)

Figure 5.27 a) Circular flange which allow for mounting of the sensor holders to form the full sensor array for mapping. b) Model of the sensor holder which mates to the sensor ring.

onto a brass sensors holder, this is done via manually gluing the sensor to the brass holder. The brass holder itself is then connected to a secondary sensor holder made of aluminum which can be mounted onto the mapping ring and be manually moved to different positions along the flange. This is done out of convenience for sensor handling and mounting. The mapping sensor holders require some manual movement in order to take the measurement of the radial magnetic field in 15 degree intervals. A 6 sensor array combined with some manual placement was chosen as good compromise for simplification of the motor controls and the DAQ (data acquisition). Therefore sensors need to be moved 4 times for full angular measurement set.

The DAQ for the mapping setup can be seen in Fig. 5.28. The DAQ is a National Instrument cDAQ 9174 controlled with LabView. The DAQ serves several functions in the mapping process. It measures the hall probes voltages, measures the limit switch voltages, sends pulse trains to the stepper motor for movement, and reads the motor encoder to record position. The Hall probes voltages are measured, recorded, and translated into magnetic field strength during the mapping process. A set of optical limit switches are used to serves as both emergency stops of the motion in the case of a motion logic failure and are also used to zero the position of the mapper on setup. The motor comes with an angular encoder which measures the total angular movement of the motor

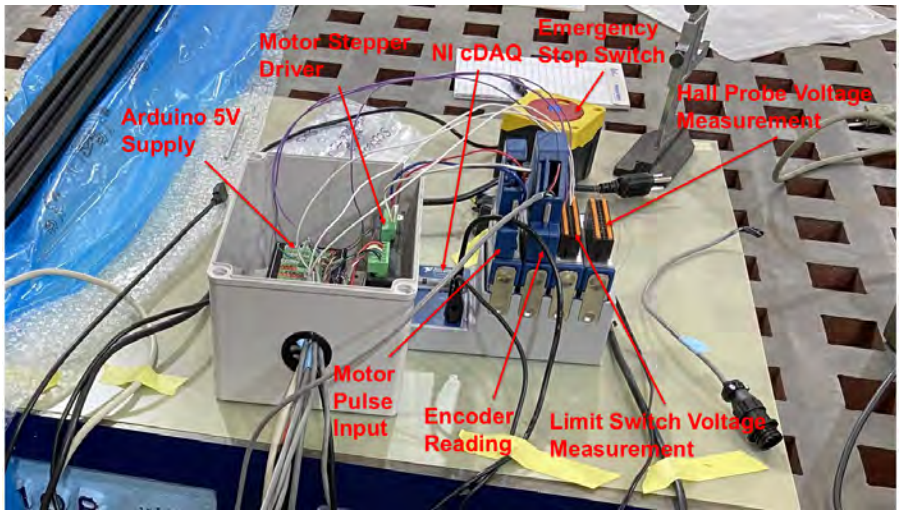

Figure 5.28 Motion control and data acquisition system for magnetic field mapping of CDQ coil.

shaft, this is translated into linear position based upon the lead screw size and also recorded for each measurement. A laser alignment tracker was used to verify the encoder reading and we found that the encoder could be used to verify the linear position to ±0.02 mm. Lastly, the motor stepper driver itself is connected to the NI DAQ so that the pulse train and motion can be controlled in LabView. The stepper driver can be used to change the motors motion resolution and has a series of different Pulse per revolution settings. The system was designed to take measurements in 5 mm steps along the beam line direction of the coil. The mapping system is mounted to the warm bore using the bores bolt hole pattern and two locating dowel pins to have it in an orientation that does not interfere with the cryocooler, this can be seen in Fig. 5.29.

The mapper has a series of alignment features in order to have the ability to make position adjustments at the top of the rail location. The bottom of the mapper has a fixed location where the ball joint at the end of the rail system fit's into the ball socket at the bottom of the warm bore. As there is no efficient way to design a closed bottom warm bore with and adjustable socket position the coil is mounted into the testing setup measured using a laser tracker to align it's position within less than 2 mm to the mechanical center of the top flange, and the straightness of the coil is adjusted such that the central axis of the coil is less than 1 degrees deflected form the top flange central axis. The alignment process was challenging due to limitations in the adjustments features and shifting of the mass during cooldown. Once the coil position is adjusted we adjust the mapper position to

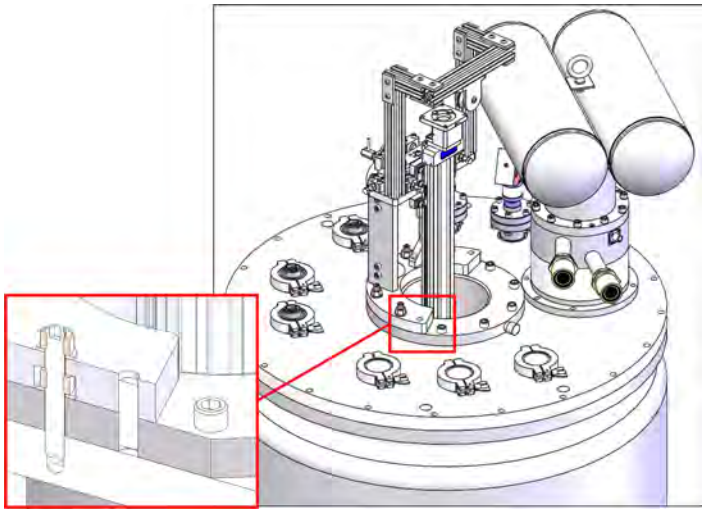

Figure 5.29 Model of magnetic field mapping system mounted onto testing setup. Close up of fasteners and dowel locating pins can be seen in red box [54].

the mechanical center of the top flange to less than 1 mm. This is done using a series of 3 laser tracker fiducial on the sensor ring to track the position relative to the flange center while the rail position is adjusted to mechanical center. Before installation the sensor carriage position is also adjusted with recept to the mapper rails such that the sensor ring is center to the rail to less than 1 mm. The fiducial placement position and adjustment features can be seen in Fig. 5.30.

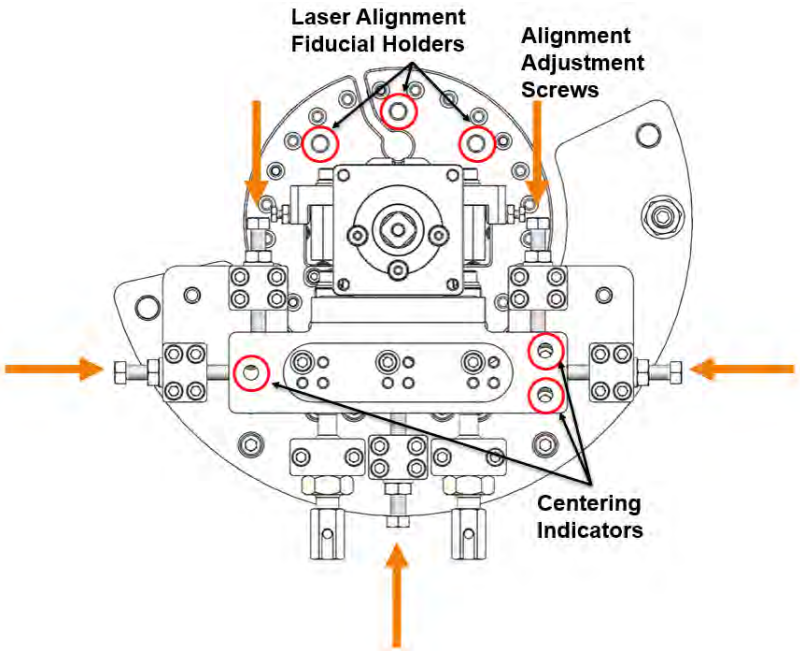

Figure 5.30 Model of magnetic mapper position adjustment features for mechanical alignment of magnetic field mapper.

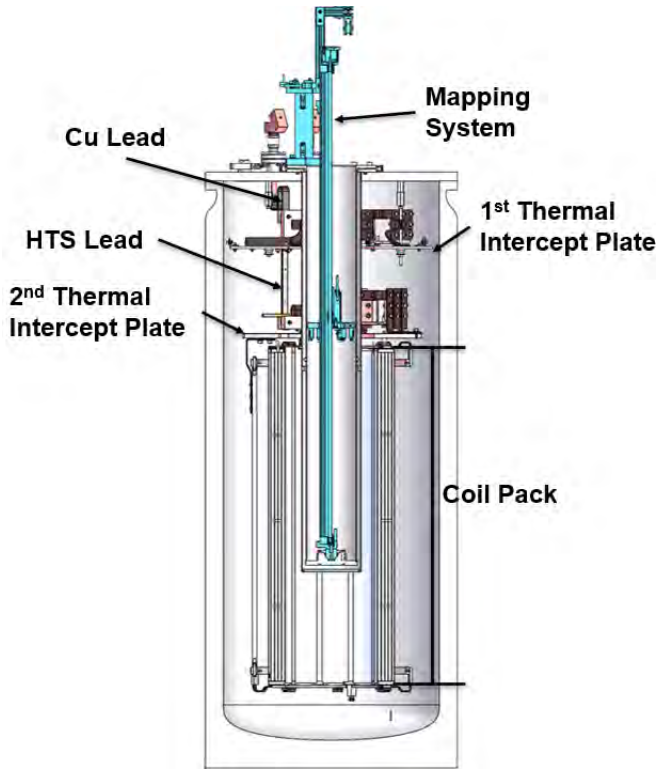

Figure 5.31 Model of the full testing assembly for magnetic field mapping of the CDQ coil.

The entire assembly is installed and aligned. Then it is motion tested to assure that the motion controls work as intended. A small current of 0.5 A is used to check that the sensor readings are working correctly. The sensors are checked again using a 5 A current when the coil is submerged in liquid nitrogen as well. Once all mapping features are tested and verified after installation into the testing setup, we are then ready for the mapping of the magnetic field at the coils maximum current. A diagram of the full testing assembly for mapping can be seen in Fig. 5.31. The following section will describe the mapping process and results.

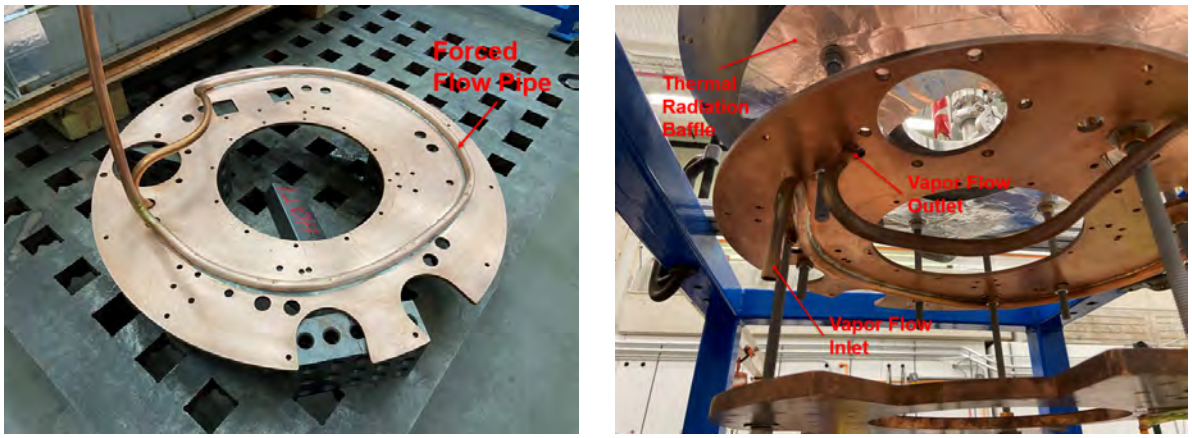

(a) (b)

Figure 5.32 a) Helium vapor forced flow pipe for first stage thermal intercept plate. b) Assembly of first stage thermal intercept plate onto testing setup.

5.7 Magnetic Field Mapping

The magnetic field mapping process is as follows: 1) The coil is energized to the desired current; 2) Set the mapper carriage to the starting position, 1.1 m from the coil center; 3) The mapping code is run and magnetic field measurements will be taken at every 5 mm along the z direction; 4) After completion of mapping procedure return the mapper carriage to the zero position; 4) Manually unscrew and move each sensor over one position clockwise; 5) Repeat the process until each sensor has taken data in a total of 4 positions, which comprises a total angular data set of every 15 degrees.

The mapping test differed from the training test in that the cryocooler was no longer in an operational state due to damage that occurred offline. This meant that the thermal intercept temperature of the first stage, which corresponds to the HTS warm end, was reliant on the cooling power provided by the vapor flow from the helium boil off. In order to make the cooling power more efficient a half inch diameter copper pipe was soldered to the first stage cooling plate and used for forced flow of helium vapor, seen in Fig. 5.32. The flow through the pipe can be controlled by opening and closing a main exhaust valve and a flow meter is connected to the forced flow outlet.

The pre-cool and helium fill process followed the same procedure as described in the previous sections. When the vessel was filled to the target fill level, approximately half way up the HTS leads, the U-tube transfer line vale is closed and the magnet is energized. At 300 A the temperature of the first thermal intercept plate increased to 72 K and continued rising. As their was concern of

the HTS lead quenching, the current was ramped down to 0 A and an adjustment was made. As the boil off rate, approximately 5 L/h, provided too little vapor flow for sufficient cooling power to the first thermal intercept plate we cracked open the valve of the U-tube transfer line in order increase vapor pressure due to liquid transfer. In practice how much the U-tube valve was opened needed to be determined manually by monitoring the temperature and vapor pressure in the system. We adjusted the valve manually until we saw a steady state of 3 psig vapor pressure in the system and the helium fill level was maintaining a constant value. This scheme provided enough cooling to keep the HTS lead warm end around 25 K, but allowed for enough time to complete magnetic field mapping at both 450 A and 300 A.

5.7.1 Mapping Results

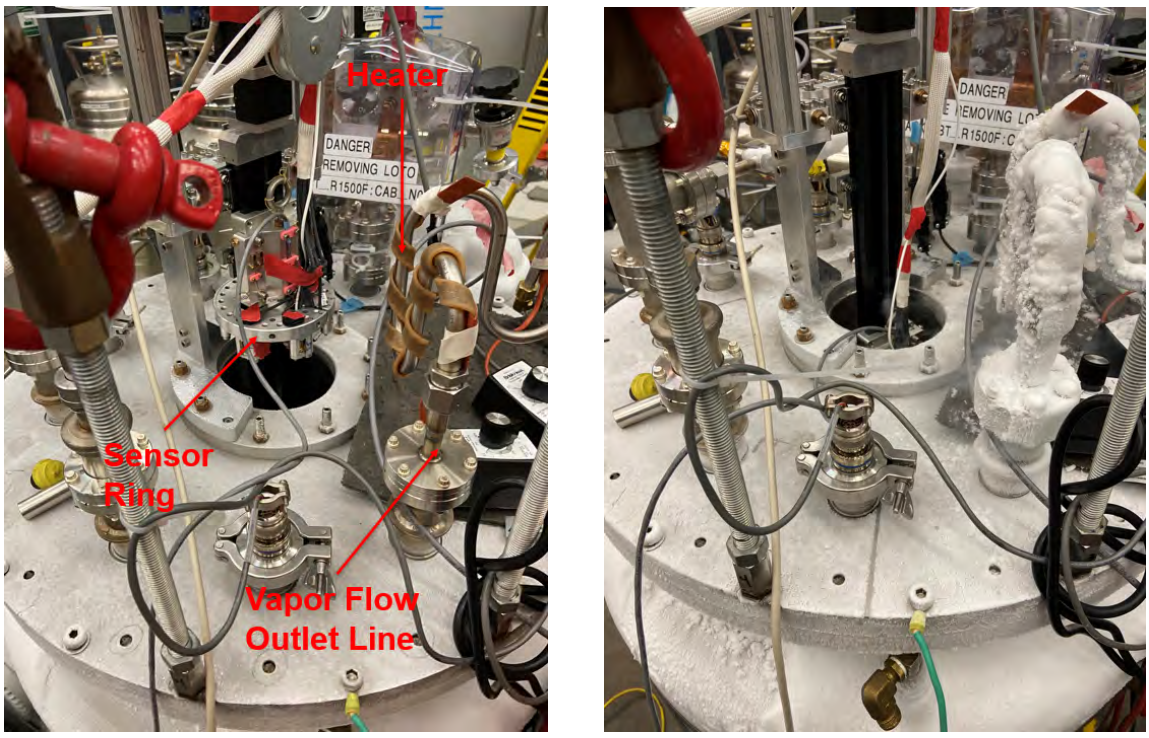

(a) (b)

Figure 5.33 a) View of the mapping assembly in the starting position. b) Magnetic field mapping in progress after coil was cooled to 4 K.

During the mapping process care needs to be taken in order to manually move the sensors without damaging them as the wires are delicate. A dry run is done to make sure that sufficient

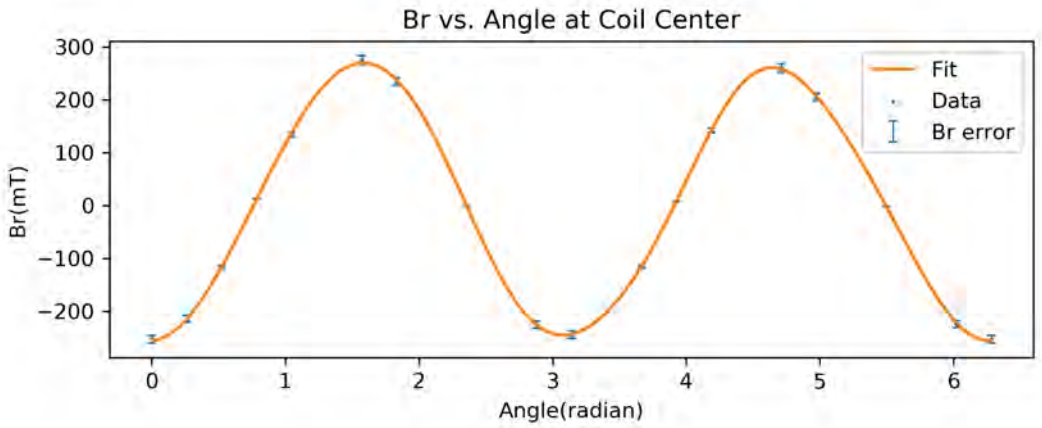

Figure 5.34 Plot of the measured field data versus angle at the center of the coil. A sine series fit of the data is seen plotted as well.

length on the sensor wires is available for sensor movement. Despite having successful movement of the sensors without damage in the functionality testing, we had multiple sensors sustain damage when moved. As this had been planned for, spare sensors were available for replacement in the case of sensor damage. Unfortunately, sensor wire damage become a consist issue during our testing procedure and we found that only 18 of the intended 24 angular data points were viable for analysis and confirmed damage to multiple sensor both from resistance check and visible damage to the sensor wires. The analysis consisted of fitting the data to a sine series, seen in Fig. 5.34. The fit compared to the data correlates to a $\chi^2_{red} = 0.54$, which is a reasonable fit considering the loss of sensors and remaining available data. The fit was used to do a harmonic decomposition analysis to analyze the field results. The technique used to calculate field harmonics is described in Chapter 2.

The rotational position of the coil is arbitrary as the coil is not in a permanent cryomodule which will be used for beam optics. A harmonics analysis of the field is done in it's arbitrary rotational position and then an angular offset is applied to place the field in either a skew or normal orientation. For the sake of consistency with the simulated results an offset is applied to put the coil field in a normal position. The angular offset of the coil to the normal position is refereed to as the roll, ϕ_{norm}, and is calculated using Eq. 5.15.

$$\phi_{norm} = -\frac{1}{2}\tan^{-1}\left(\frac{A_2}{B_2}\right) \tag{5.15}$$

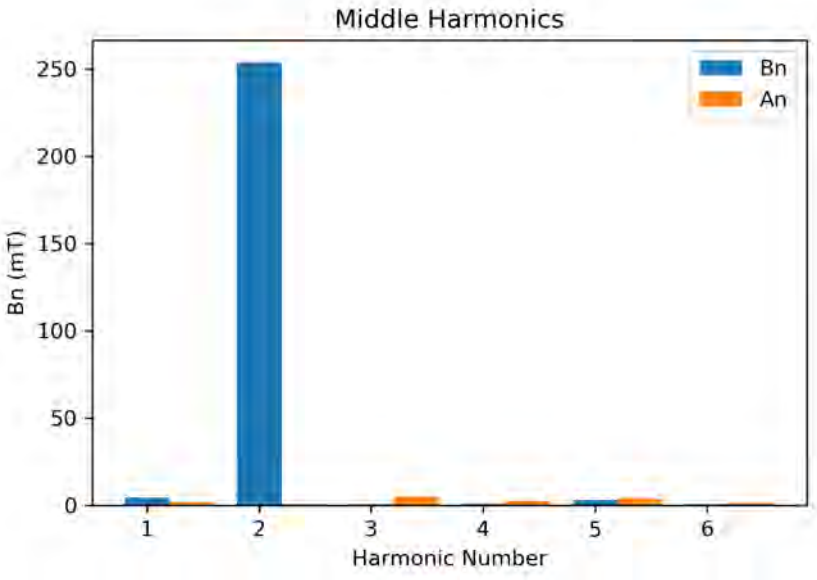

Figure 5.35 Calculated harmonics at the center of the CDQ coil at 450 A.

Where A_2 and B_2 are the normal and skew quadrupole harmonics. The roll is then calculated and applied as an offset to place the field in normal orientation. Once put in normal orientation a harmonic analysis is then done on the field in normal orientation. These results can be seen in Fig. 5.35. The quadrupole gradient plotted against the beam line direction to the coil center can also be seen in, Fig. 5.36. While the field has been aligned rotationally into a normal orientation, a transverse offset still exists therefore the misalignment distance in the x and y can be calculated to show how the center of the coil has shifted during cooldown.

The misalignment is directly proportional to the dipole harmonic terms $B1$ and $A1$. The dipole and quadrupole terms can be used to directly calculate the misalignment using Eq. 5.16 & 5.17.

$$x_m = -r\frac{B_2B_1 + A_2A_1}{B_2^2 + A_2^2} \tag{5.16}$$

$$y_m = -r\frac{B_2A_1 - A_2B_1}{B_2^2 + A_2^2} \tag{5.17}$$

The x and y misalignment calculated is 1.13 mm and 0.2 mm respectively. As the x alignment is larger than the measured alignment while the coil is warm, shifting of the cold mass is suspected during the cooldown process. Movement during cooldown is a difficult problem to combat, in the

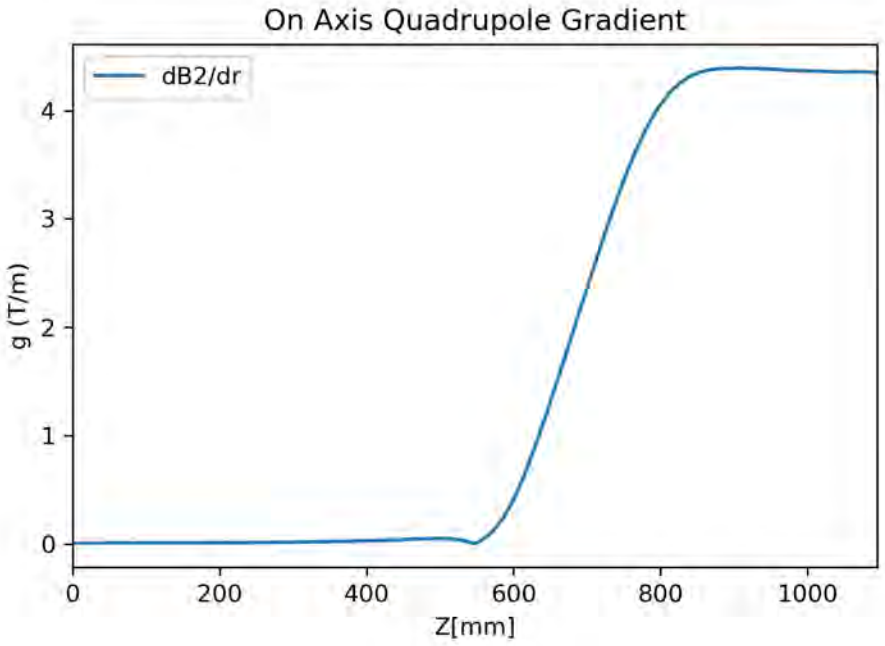

Figure 5.36 Plot of quadrupole gradient in the beam line direction.

absence of alignment features that can be used after cooldown. There is very little that can be done when the mapping system does not have full transverse motion at both ends. Based on the calculated misalignment a correction term can be added which is proportional to the x and y misalignment to reflect what better alignment would look like from the coil. This results in minimized $B1$ and $A1$ terms.

Radial magnetic field, B_r, can be expressed in terms of a summation of normal and skew harmonic as outlined in Chapter 2. A correction term can be applied to the radial field distribution to show a "virtual" alignment. Meaning a dipole field proportional to the misalignment can be added to the radial field distribution to reflect better aligned field.

$$B_{correction} = B_1 \cos\phi + A_1 \sin\phi \tag{5.18}$$

The quadrupole skew term is low enough that Eq. 5.16 & 5.17 simplifies to Eq. 5.19 & 5.20, which produces the same results.

$$B_1 \approx x_m g \tag{5.19}$$

$$A_1 \approx y_m g \tag{5.20}$$

This simplification can then be used in the correction term, so that it can be expressed in terms of misalignment and quadrupole gradient.

$$B_{correction} = x_m g \cos\phi + y_m g \sin\phi \tag{5.21}$$

A "virtually" aligned field can then be expressed as Eq. 5.22

$$B_{aligned} = B_r(r_0, \phi) + B_{correcion}(r_0, \phi) \tag{5.22}$$

Where $B_r(r_0, \phi)$ is the radial magnetic field at reference radius from the measured data, $B_{correction}$ is the radial magnetic field correction term, x_m and y_m are the misalignment distances in x and y, ϕ is the azimuth angle, and g is the quadrupole field gradient, and $B_{aligned}$ is the radial magnetic field as a function of azimuth angle at the reference radius if the field was aligned to the mappers sensor ring center.

The results of virtual alignment can be seen in Fig. 5.37. The reduction of the dipole harmonic can be seen when compared to Fig. 5.35, and correlates to a misalignment of 12 μm in x and 2 μm in y. The alignment correction has a negligible impact on the quadrupole component and improves the overall non-uniformity of the field from 3.2% to 1.5%. The measured field and simulation results have good agreement for the quadrupole gradient, integrated strength, and effective length. The results can be seen in Table 5.5.

The alignment correction has a negligible impact on the quadrupole component and improves the overall non-uniformity of the field from 3.2% to 1.5%. The measured field and simulation results have good agreement for the quadrupole gradient, integrated strength, and effective length. The results can be seen in Table 5.5.

The analysis shows higher non-uniformity than the simulation and in particular the $n = 5$ harmonic is higher than one would expect from the simulation, seen in Chapter 2. Unfortunately, a non-uniformity below 1% is part of the design requirement for this project. As alignment was

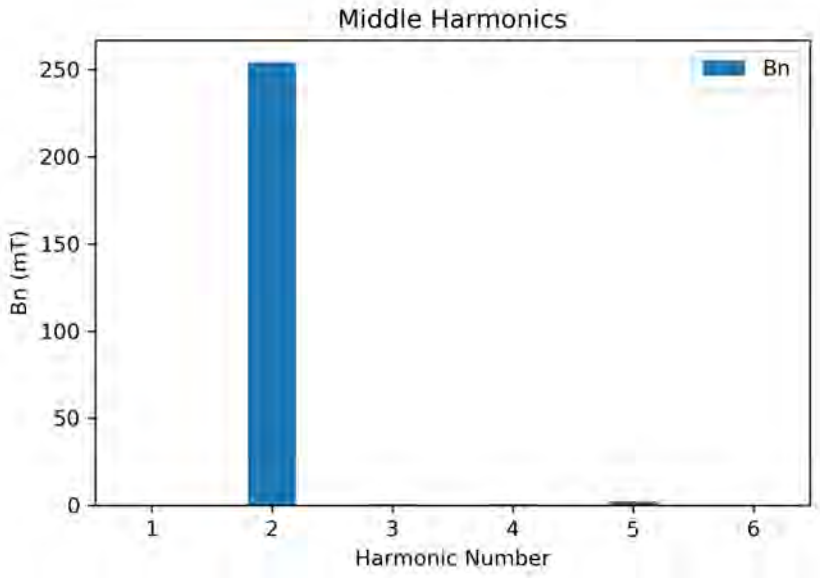

(a)

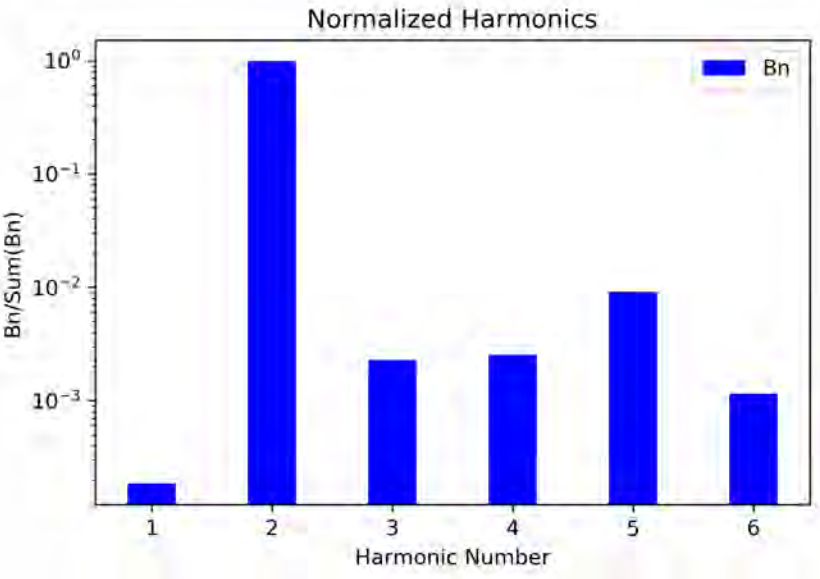

(b)

Figure 5.37 a) Harmonics of the CDQ coil at center at 450 A when virtual alignment correction was applied. b) Normalized log plot of harmonics of CDQ coil at 450 A after alignment correction.

challenging for this magnetic field mapping and a series of sensors received damage part of the future work is to improve the measurement system for a full length magnetic field verification of a full CDQ package. It is worthy of mention that during the magnetic field mapping there was no quench observed during any part of testing and that the design shows promise in terms of strength

Table 5.5 Mapping Results

Results	Measured	Simulation
Gradient (T/m)	3.99	3.96
Half Effective Length (mm)	404	401
Integrated Strength (T)	3.22	3.17
Non-Uniformity	1.53%	0.1%

and stability, but uniformity requires further verification. Further aspects of the future work are discussed in the conclusion.

CHAPTER 6

CONCLUSIONS AND FUTURE WORK

This chapter reports on the conclusions of the findings of this thesis and the future work for further progress on this project.

6.1 Conclusions

6.1.1 Coil Design and Fabrication Feasibility

It was discussed in Chapter 2 that a magnet model which could fulfill the design requirements was established. After an investigation of conductor options, a selection was made and a quench analysis was done to see if the selection was feasible in term of both stability and winding. The findings were that our selected conductor worked well in terms of stability and windings for the designed winding geometry.

6.1.2 Beam Impact

In Chapter 3, a study was done to quantize the dipole component induced by the sextupole package nested in the iron-dominated quadrupoles. on the optical impact of replacing some of the iron-dominated triplets of FRIB's fragment separator with CDQ magnets triplets. It was found that the impact of the dipole component induced would require active correction and that replacement of the FSQC and FSQB magnets with CDQ quads would eliminate this issue. The additional benefits of the CDQ design discussed in this thesis also demonstrate their promise as a replacement.

6.1.3 Coil Winding and Fabrication

In Chapter 4 the fabrication process of the single layer prototype quad was discussed. While a successful winding and impregnation was completed, there were issues which plagued the process. The style of insulating coating we used was found to be difficult to work with with our style of winding, and resulted in several failed winding attempts due to electrical shorts to the winding bobbin. A similar issue arose after the impregnation process, where one of the 4 wires was shorting to the winding bobbin and needed to be isolated and the coil wires required re-splicing.

6.1.4 Cold Testing and Magnetic Field Mapping

In Chapter 5 the details of the cold testing for the coil and magnetic field mapping were discussed. The single layer CDQ prototype was able to reach the 500 A and operate stably with the use of HTS leads which were also be to operate stably at 500 A. The coil never quenched at any point of testing, which shows promising preliminary results for the operational stability of these coils. The alignment of the magnet to the mapping warm bore was a challenging process, and we did not have success aligning the coil to less than 1 mm in the xy-plane. The sensor array also provided some challenges, as the manual movement of sensors resulted in damage to multiple sensors.

6.2 Future Work

The implementation of a conduction cooling scheme was discussed in Chapter 5. The implementation of this was beyond the scope of this thesis work, but a conduction cooling scheme was the motivation for the design of HTS leads and the integration of a cryocooler. The design and implementation of a conduction cooling scheme for the CDQ coils will be part of future work, and a working design would be very advantageous for saving liquid helium, as liquid helium is a growing expense in applied superconductivity.

Additionally, due to the challenges of coil alignment to the mapper bore in the testing setup, a series of improvements will be made to the mechanical design such that the coil can be kept centered to the warm bore for magnetic field mapping to guarantee alignment of less than 1 mm in xy-plane. The mapper sensor array will also be improved upon further, to help minimize sensor damage risk. Sensors will be stationary and require no movement. Lastly, a full CDQ package, as outlined in Chapter 2, is in fabrication and will be liquid helium tested. Lastly, the full length of the coil will be mapped using the upgraded mapping system.

BIBLIOGRAPHY

[1] S. Y. Lee, *Accelerator physics*, Fourth edition. World Scientific Publishing Co. Pte. Ltd., 2019, ISBN: 978-981-327-467-9.

[2] M. Venturini and A. J. Dragt, "Accurate computation of transfer maps from magnetic field data," *Nuclear Instruments and Methods in Physics Research Section A: Accelerators, Spectrometers, Detectors and Associated Equipment*, vol. 427, no. 1, pp. 387–392, 1999, ISSN: 0168-9002. DOI: https://doi.org/10.1016/S0168-9002(98)01518-6. [Online]. Available: https://www.sciencedirect.com/science/article/pii/S0168900298015186.

[3] M. Venturini, "Lie methods, exact map computation, and the problem of dispersion in space charge dominated beams," English, Ph.D. dissertation, University of Maryland, 1998, p. 268, ISBN: 978-0-599-07185-8. [Online]. Available: https://ezproxy.msu.edu/login?url=https://www.proquest.com/dissertations-theses/lie-methods-exact-map-computation-problem/docview/304428612/se-2.

[4] J. T. Tanabe, *Iron dominated electromagnets: design, fabrication, assembly and measurements*. World Scientific, 2005.

[5] S. Russenshuck, *Field Computation for Accelerator Magnets*, 1st ed. John Wiley & Sons, Ltd, 2010, _eprint: https://onlinelibrary.wiley.com/doi/pdf/10.1002/9783527635467. DOI: 10.1002/9783527635467. [Online]. Available: https://onlinelibrary.wiley.com/doi/10.1002/9783527635467 (visited on 04/05/2023).

[6] F. Savary, B. Bordini, L. Fiscarelli, *et al.*, "Design and Construction of the Full-Length Prototype of the 11-T Dipole Magnet for the High Luminosity LHC Project at CERN," *IEEE Transactions on Applied Superconductivity*, vol. 28, no. 3, pp. 1–6, 2018. DOI: 10.1109/TASC.2018.2800713.

[7] W. Wei, L. Yu, Z. Lun-Cai, *et al.*, "Multipole magnets for the HIAF fragment separator using the Canted-Cosine-Theta (CCT) geometry.," *Journal of Physics: Conference Series*, vol. 1401, no. 1, p. 1, 2020, ISSN: 17426588. [Online]. Available: http://ezproxy.msu.edu/login?url=https://search.ebscohost.com/login.aspx?direct=true&AuthType=ip,uid,cookie&db=edb&AN=141540302&site=eds-live.

[8] J. Nolen, S. L. Manikonda, M. Authier, *et al.*, "Design and Status of the Super Separator Spectrometer for the GANIL SPIRAL2 Project," en,

[9] P. Ostroumov, M. Hausmann, K. Fukushima, *et al.*, "Heavy ion beam physics at Facility for Rare Isotope Beams," en, *Journal of Instrumentation*, vol. 15, no. 12, P12034–P12034, Dec. 2020, ISSN: 1748-0221. DOI: 10.1088/1748-0221/15/12/P12034. [Online]. Available: https://iopscience.iop.org/article/10.1088/1748-0221/15/12/P12034 (visited on 04/04/2023).

[10] M. Hausmann, A. M. Aaron, A. M. Amthor, *et al.*, "Design of the advanced rare isotope

separator ARIS at FRIB," *Nuclear Instruments and Methods in Physics Research Section B: Beam Interactions with Materials and Atoms*, vol. 317, pp. 349–353, 2013.

[11] M. Portillo, B. Sherrill, Y. Choi, *et al.*, "Commissioning of the Advanced Rare Isotope Separator ARIS at FRIB," *Nuclear Instruments and Methods in Physics Research Section B: Beam Interactions with Materials and Atoms*, vol. 540, pp. 151–157, 2023, ISSN: 0168-583X. DOI: https://doi.org/10.1016/j.nimb.2023.04.025. [Online]. Available: https://www.sciencedirect.com/science/article/pii/S0168583X23001556.

[12] A. F. Zeller, J. C. DeKamp, D. Johnson, *et al.*, "Magnetic elements for the A1900 fragment separator at the NSCL," in *Advances in cryogenic engineering*, Springer, 1998, pp. 245–252.

[13] P. L. Walstrom, "Some New Design Codes for High-Field Magnetic Lens Systems," Los Alamos National Laboratory, Internal Report, Jan. 1997.

[14] P. L. Walstrom, "Design of End Turns in Current-Dominated Dipole and Quadrupole Magnets for Fields with Low Higher-Harmonic Content," en, Jan. 2002. [Online]. Available: %5Curl%7Bhttps://www.osti.gov/biblio/976187%7D.

[15] P. Walstrom, "Dipole-sheet multipole magnets for accelerators," *IEEE Transactions on Magnetics*, vol. 30, no. 4, pp. 2471–2474, 1994. DOI: 10.1109/20.305778.

[16] P. L. Walstrom, "Magnetic Fields and Inductances of Cylindrical Current Sheet Magnets," Los Alamos National Laboratory, Internal Report LA-UR-90-4090, Dec. 1990.

[17] P. L. Walstrom, "Magnetic Fields from Distributions of Dipoles on Cylindrical Surfaces," Los Alamos National Laboratory, Internal Report LA-UR-91-3496, Nov. 1991.

[18] P. Walstrom, "Soft-edged magnet models for higher-order beam-optics map codes," *Nuclear Instruments and Methods in Physics Research Section A: Accelerators, Spectrometers, Detectors and Associated Equipment*, vol. 519, no. 1, pp. 216–221, 2004, Proceedings of the Sixth International Conference on Charged Part icle Optics, ISSN: 0168-9002. DOI: https://doi.org/10.1016/j.nima.2003.11.158. [Online]. Available: https://www.sciencedirect.com/science/article/pii/S0168900203030237.

[19] P. L. Walstrom, "Design of End Turns in Current-Dominated Dipole and Quadrupole Magnets for Fields with Low Higher-Harmonic Content," Los Alamos National Laboratory, Internal Report LA-UR-01-6661, Nov. 2001.

[20] D. Greene, Y. Choi, J. DeKamp, *et al.*, "Design of coil-dominated quadrupole triplet for high rigidity isotope beams," *IEEE Transactions on Applied Superconductivity*, vol. 33, no. 5, pp. 1–5, 2023. DOI: 10.1109/TASC.2023.3255825.

[21] M. N. Wilson, *Superconducting Magnets* (Monographs on Cryogenics). Oxford, New York: Oxford University Press, Mar. 1987, ISBN: 978-0-19-854810-2.

[22] L. Dresner, *Stability of Superconductors*. New York, NY, UNITED STATES: Springer, 1995, ISBN: 978-0-306-47064-6. [Online]. Available: http://ebookcentral.proquest.com/lib/michstate-ebooks/detail.action?docID=3035541 (visited on 04/05/2023).

[23] X. Du, private communication, Nov. 2024.

[24] Q. Zhao, A. Facco, F. Marti, *et al.*, "FRIB accelerator beam dynamics design and challenges," *Growth*, vol. 400, p. 4, 2021.

[25] A. Gade, B. M. Sherrill, *et al.*, "The Scientific Case for the 400 MeV/u Energy Upgrade of FRIB," Facility for Rare Isotope Beams, Tech. Rep., 2019.

[26] M. Berz and K. Makino, "Cosy infinity version 8.1. user's guide and reference manual," *Department of Physics and Astronomy MSUHEP-20704, Michigan State University*, 2002.

[27] S. S. Chouhan, T. Borden, J. DeKamp, *et al.*, "Superferric cold iron quadrupole magnets for FRIB fragment separator," *IEEE transactions on applied superconductivity*, vol. 24, no. 3, pp. 1–5, 2013.

[28] R. F. Muraca and J. S. Whittick, "Materials data handbook: Aluminum alloy 6061," (Western Applied Research and Development, Inc., Tech. Rep., 1972.

[29] D. Greene *et al.*, "Status of coil-dominated discrete-cosine-theta quadrupole prototype for high rigidity isotope beams," English, in *Proc. 15th International Particle Accelerator Conference*, (Nashville, TN), ser. IPAC'24 - 15th International Particle Accelerator Conference, JACoW Publishing, Geneva, Switzerland, May 2024, pp. 2854–2857, ISBN: 978-3-95450-247-9. DOI: 10.18429/JACoW-IPAC2024-WEPS67. [Online]. Available: https://indico.jacow.org/event/63/contributions/4177.

[30] Z. Ahmad, *Principles of corrosion engineering and corrosion control*. Elsevier, 2006.

[31] P. G. Sheasby, R. Pinner, and S. Wernick, *The surface treatment and finishing of aluminium and its alloys*. ASM international Materials Park, OH, 2001, vol. 1.

[32] Y. Al-Mahmoud, private communication, Oct. 2023.

[33] S. Krave, "Coil impregnation processes and experiences at FNAL," in *Workshop on Nb3Sn Technology for Accelerator Magnets, https://indico.cern.ch/event/743626/contributions/3154003*, 2018.

[34] R. Reed, F. Roundy, N. Martovetsky, J. Miller, and T. Mann, "Resin permeation through compressed glass insulation for iter central solenoid," in *AIP Conference Proceedings*, American Institute of Physics, vol. 1219, 2010, pp. 111–118.

[35] J. Axensalva, F. Lackner, and R. Gauthier, "Vacuum Pressure Impregnation Setup at CERN

for Nb3Sn Coils," *IEEE Transactions on Applied Superconductivity*, vol. 30, no. 4, pp. 1–4, 2020. DOI: 10.1109/TASC.2020.2977028.

[36] D. Zhang, private communication, Nov. 2023.

[37] J. D. Jackson, *Classical electrodynamics*. John Wiley & Sons, 2021.

[38] Composite Technology Dvelopment, Inc., "CTD-101K Epoxy Resin System Datasheet," Composite Technology Dvelopment, Inc., Tech. Rep., 2014.

[39] J. Ekin, *Experimental Techniques for Low-Temperature Measurements: Cryostat Design, Material Properties and Superconductor Critical-Current Testing*. Oxford, UNITED KINGDOM: Oxford University Press, Incorporated, 2006, ISBN: 978-0-19-152469-1. [Online]. Available: http://ebookcentral.proquest.com/lib/michstate-ebooks/detail.action?docID=430810 (visited on 04/05/2023).

[40] A. Ballarino, "Large-capacity current leads," *Physica C: Superconductivity*, vol. 468, no. 15, pp. 2143–2148, 2008, Proceedings of the 20th International Symposium on Superconductivity (ISS 2007), ISSN: 0921-4534. DOI: https://doi.org/10.1016/j.physc.2008.05.217. [Online]. Available: https://www.sciencedirect.com/science/article/pii/S0921453408004553.

[41] Y. Iwasa, *Case studies in superconducting magnets: design and operational issues*. Springer science & business media, 2009.

[42] H. G. Lee, H. M. Kim, B. W. Lee, *et al.*, "Conduction-cooled brass current leads for a resistive superconducting fault current limiter (SFCL) system," *IEEE transactions on applied superconductivity*, vol. 17, no. 2, pp. 2248–2251, 2007.

[43] C. Hoffmann, N. Strickland, D. Pooke, J. Gannon, B. Carter, and A. Otto, "Thermal conductivity of 2G HTS wires for current lead applications," *Journal of Physics: Conference Series*, vol. 234, no. 2, p. 022 015, Jun. 2010. DOI: 10.1088/1742-6596/234/2/022015. [Online]. Available: https://dx.doi.org/10.1088/1742-6596/234/2/022015.

[44] L. Ren, Y. Tang, J. Li, *et al.*, "Conduction-Cooled YBCO HTS Current Lead for SMES Application," *IEEE Transactions on Applied Superconductivity*, vol. 20, no. 3, pp. 1737–1740, 2010. DOI: 10.1109/TASC.2010.2044776.

[45] K. Ohsemochi, M. Ono, S. Nomura, *et al.*, "Development of 3kA conduction cooled HTS current lead system," *Cryogenics*, vol. 43, no. 10, pp. 643–648, 2003, Korea-Japan Joint Workshop 2002 on Applied Superconductivity and Cryogenics, ISSN: 0011-2275. DOI: https://doi.org/10.1016/S0011-2275(03)00176-0. [Online]. Available: https://www.sciencedirect.com/science/article/pii/S0011227503001760.

[46] Y. Yamada, Y. Ishii, S. Sakai, *et al.*, "HTS Current Leads Prepared by the TFA-MOD Processed YBCO Tapes," *IEEE Transactions on Applied Superconductivity*, vol. 21, no. 3,

pp. 1054–1057, 2011. DOI: 10.1109/TASC.2011.2106751.

[47] P. Bauer, Y. Bi, A. Cheng, *et al.*, "R&D Towards HTS Current Leads for ITER," *IEEE Transactions on Applied Superconductivity*, vol. 19, no. 3, pp. 1500–1503, 2009. DOI: 10.1109/TASC.2009.2017838.

[48] W. D. Markiewicz, T. Painter, I. Dixon, and M. Bird, "Quench transient current and quench propagation limit in pancake wound REBCO coils as a function of contact resistance, critical current, and coil size," *Superconductor Science and Technology*, vol. 32, no. 10, p. 105 010, 2019.

[49] N. Bagrets, G. Celentano, A. Augieri, R. Nast, and K.-P. Weiss, "Investigation of soldered REBCO tape–copper joints for superconducting applications," *IEEE Transactions on Applied Superconductivity*, vol. 26, no. 4, pp. 1–4, 2016.

[50] S. W. Van Sciver, *Helium Cryogenics*, en. New York, NY: Springer, 2012, ISBN: 978-1-4419-9979-5. DOI: 10.1007/978-1-4419-9979-5. [Online]. Available: http://link.springer.com/10.1007/978-1-4419-9979-5 (visited on 04/05/2023).

[51] A. Sensor, *HE244X Datasheet*, 2024. [Online]. Available: https://asensor.eu/onewebmedia/Datasheet-HE244X.pdf.

[52] S. AG, *Hall Probe Type C for 3MH6/3MH4 Digital Teslameters and I3D Low Noise Magnetic Field Transducers, Rev. 1.1*, 2023. [Online]. Available: https://www.senis.swiss/wp-content/uploads/2023/04/Hall-probe-type-C-for-3MH6-3MH4-digital-teslameters-and-I3D-low-noise-magnetic-field-transducers_rev.1.1.pdf.

[53] S. AG, *High Performance 3-Channel Digital Teslameter 3MH6-E, Rev. 3.1*, 2023. [Online]. Available: https://www.senis.swiss/wp-content/uploads/2023/04/High-Performances-3-Channe-Digital-Teslameter-3MH6-E_rev.3.1.pdf.

[54] Y. Al-Mahmoud, private communication, Oct. 2024.